MEASUREMENTS OF ROTOR STALLING IN A MATCHED AND A MISMATCHED MULTISTAGE COMPRESSOR

by

Peter D. Silkowski

GTL Report #221 April 1995

GAS TURBINE LABORATORY
MASSACHUSETTS INSTITUTE OF TECHNOLOGY
CAMBRIDGE, MASSACHUSETTS

MEASUREMENTS OF ROTOR STALLING IN A MATCHED AND A MISMATCHED MULTISTAGE COMPRESSOR

by

Peter D. Silkowski

GTL Report #221 April 1995

This research was supported by the Air Force Office of Scientific Research, Major Daniel Fant, Technical Monitor; General Electric Aircraft Engine Co.; and the Air Force Research in Aero Propulsion Technology (AFRAPT) Program.

Measurements of Rotor Stalling in a Matched and a Mismatched Multistage Compressor

by

Peter Daniel Silkowski

Abstract

This paper presents the results from a set of experiments on stall inception in multistage axial flow compressors. The experiments were tailored to investigate phenomena having a wide range of time and length scales. This range of scales was motivated by two previously observed paths to stall. Parametric changes such as tip clearance, inlet distortion and mismatch were carried out to demonstrate the importance of component coupling in the stall inception process. Evidence is presented for the importance of the local compressor characteristic in determining where and when the initiation of the stall inception process will occur. Although the stall inception process may begin as a localized event, its growth into rotating stall is governed by the environment established by the coupling of the various compression system components. Finally, the tip flow field, specifically the rotor tip leakage jet, is shown to be a key feature in the stall inception process.

Acknowledgments

The work presented in this document is only a small fraction of a much larger research program, involving several teams of people without whom, none of this would have been possible. The author wishes to acknowledge the following people and organizations for their efforts in this project:

Prof. E.M. Greitzer and Dr. C.S. Tan for allowing me this opportunity and for their guidance in matters both technical and nontechnical.

Prof. N.A. Cumpsty for his patience and insight in sifting through the data with me. I would also like to thank Prof. Cumpsty for his continued help and support in creating this document.

Dr. I.J. Day for his help and suggestions in setting up and running the experiments.

Dr. J.P. Longley for his involvement in planning the experiment and teaching me about data analysis.

Prof. J.E. McCune for his interest and support.

General Electric and specifically the people of the Aerodynamics Research Laboratory. The people and the facilities at G.E. are all top notch. My experience there was both fruitful and enjoyable. I want to thank everyone there for their help and friendship.

Mr. Bill Groll for helping me with the G.E. computing facilities and everythingelse.

Mr. Don Menner for coming in very early and staying late so that I could have a full day of running. Don's efforts to make changes to the rig and to keep it running so that we could stay on schedule were legendary.

Dr. Brent Beacher for answering all of my questions.

Mr. Randy Bauer, Mr. David Halstead, Mr. Gary Osterbrock, and Mr. Thomas Herdman for their help and friendship.

Dr. Steve Manwaring for accommodating my experiments while he was trying to conduct work of his own.

Dr. H.W. Shin for his patience in teaching me how to operate the instrumentation, data collection and storage equipment, and all the required software. Dr. Shin was a very key part in the running of these experiments. I am very thankful to him for the many hours he worked with me, especially late night and on the weekends, and for his willingness to help me with whatever I needed. Dr. Shin's experience and calm nature were very helpful under sometimes hectic and stressful situations of running an experimental program of this size and caliber.

Dr. D.C. Wisler director of the Aerodynamics Research Laboratory, without whose support, none of this work would have been possible. Dr. Wisler's enthusiasm towards the project was also a helpful motivator through some of the long days and nights of set up and running. I also want to thank Dr. Wisler for all of the personal help, support, encouragement and advice that he has given me throughout this process.

Finally, I want to thank all of my family and friends for their support, my parents and sister, and some friends from MIT: Dan Gysling, Aaron Gleixner, Dave Tew, Norm Sun, Mark Campbell, Yew Poh Mak, S. J. Song, Taras Palczynski, and Jon Simon.

This work was supported by the Air Force Office of Scientific Research, Monitor Maj. Daniel Fant, USAF Grant# AFOSR-90-0035, General Electric Aircraft Engine Co., and the Air Force Research in Aero Propulsion Technology (AFRAPT) Program, Grant# AFOSR-91-0052.

Table of Contents

Introduction

Recent studies of rotating stall inception have led to the definition of two different paths from the essentially axisymmetric flow in the pre-stall state to fully developed rotating stall. The first path involves the growth of a small amplitude long circumferential length scale (O~1 circumference) traveling wave into a mature rotating stall cell. The initial propagation speed of this traveling wave is equal to or slightly less then the mature stall cell speed. Furthermore, this small amplitude traveling wave can exist for a long time (tens of rotor revs.) before becoming a stall cell. This scenario agrees well with several models which predict the growth of traveling waves at the peak of the total to static characteristic. These long length scale traveling waves are referred to as modes [1].

A different scenario has been observed which involves the growth and deceleration of a short circumferential (few blade pitches) fast moving disturbance into a mature stall cell in only a few rotor revolutions. These short length scale phenomena are referred to here as pips. An important factor in the design of this experiment was the desire to focus on these different time and length scales associated with the pips and modes. This influence is seen in the circumferential distribution of the testing probes, first over the entire circumference and then more closely spaced over three blade pitches. Furthermore, the axial locations of probes well upstream of the rotor were intended to filter out any short length scale disturbances (pips) and make longer length scale disturbances (modes) clearer. Finally, several rig modifications were used as tools to focus on specific time and length scales. These included mismatch, (restaggering the rear three stages of the four stage compressor to a lower design ϕ), asymmetric tip clearance, and a distortion screen.

Six main questions to be addressed are:

1) What are the mechanisms of rotating stall inception?

2) Is there a repeatable prestall event, and if so, is it a long wavelength disturbance (mode), short wavelength disturbance (pip), or some combination of the two, coupling?

3) At the blade passage length scale how do the various fluid dynamic structures (tip vortex/leakage jet, blade wakes, and endwall boundary layers) behave with

changing operating point and what role do these structures play in the stall inception process?

4) How do inlet distortion and changes in tip clearance affect the stall inception process?

5) What is the overall machine and local flow field behavior in the first stage operated below its normal stall flow when stabilized by mismatching the rear three stages?

6) What role does component coupling play in stall inception?

Experimental Facilities

This project was a collaborative effort between academia and industry. The three groups involved were MIT, GE Cincinnati, and The Whittle Lab, Cambridge England. The experiments were carried out at the General Electric Aerodynamics Research Laboratory, with the cooperation of Dr. D.C. Wisler's group. This facility has a low speed research compressor that duplicates high speed compressor flow fields in a large low speed machine (60" diameter). This large size minimizes probe blockage and allows for easier access and instrumentation whilst giving correct Reynolds number at low operating speed. Furthermore, this rig is very flexible and changing tip clearance, blade stagger, or adding unsteady distortion can all be achieved with relative ease. The compressor has four repeating stages and the NASA/GE E^3 blading was used to represent a current high performance multistage machine (see fig. 1). For further information on this facility or the blading see reference [2].

In addition to the standard instrumentation for steady state pressure rise and flow rate, high response pressure transducers and hot wires were used. A radially traversable slant wire, to give three components of velocity, and a total pressure probe were also used at several operating points at rotor inlet and rotor exit of various builds. The slant wire and the total pressure probe signals were phase locked to the rotor. Several steady state experiments were conducted at each radial location, and the results ensemble averaged to create a picture of rotor locked phenomena (blade wakes, tip vortex, etc.).

The bulk of the experiments were carried out with fixed arrays of 40 probes, consisting of 20 hot wires and 20 pressure transducers. At IGV exit there were 10 reference hot wires at midspan and 10 corresponding pressure transducers in the casing. These 10 reference locations were circumferentially distributed in the following manner: 0°,45°,90°,135°,180°,225°,270°,315°. These eight equally spaced locations would allow spatial Fourier analysis. In addition to these locations, the remaining two pressure transducers were placed at 200°, 210° and the two remaining hot wires were at 15°, 25°. The purpose of these extra offset probes was to allow crosscorrelations over various distances, to combat spatial aliasing (see fig. 2). With all the dynamic instrumentation appropriate logging and filtering rates were used to insure temporal resolution and to prevent temporal aliasing. Specifically, most of the unsteady data was sampled at 10 kHz and low pass filtered at 3 kHz, with a few cases sampled at 1 kHz and low pass filtered at 300 Hz.

Complementing the reference probes there were 10 testing hot wires and 10 testing pressure transducers. The circumferential distribution of these testing probes is identical to the reference probes referred to above. However, whereas the reference probes are fixed at their locations for all runs as a control, allowing comparisons between various runs, the test probes were moved to various axial-radial positions. The testing probes were used at four axial locations: one half of a radius and one quarter of a radius upstream of rotor inlet, also at rotor inlet, and rotor exit, which were at locations roughly 0.2 chord upstream and downstream of the rotor respectively. In all cases the testing pressure transducers were in the casing. When at R/2 or R/4 upstream the testing hot wires were at midspan. At rotor inlet and rotor exit the testing hot wires were usually at 20% and then at 80% immersion (tip and hub) (see fig. 3), but other immersions were investigated. To focus on small length scale events, experiments were also performed with testing probes at the rotor inlet and rotor exit locations, but with eight testing probes equally spaced over three blade pitches.

One of the key features of this facility is the relative ease with which major modifications to the rig can be made. This ability was used to investigate three variations from the baseline build. The baseline build's overall speedline and stall hysteresis loop are displayed in Figure 4. Figure 5 is the performance of the first stage only and several points are labeled for future reference. Point A is design and point E is just before stall. Figure 6 displays the individual static pressure rise characteristics for all four stages.

The first variant from the baseline build was the mismatch. The purpose of the mismatch was to extend the stable operating region of the first stage and to provide a clearer view of any pips by suppressing any long length scale disturbances, thus preventing modal stall. This mismatch was achieved by closing the rear three rotors by 10°. Figure 7 shows the result of the mismatch on the overall characteristic. The stalling flow coefficient was changed from 0.345 to 0.308. Note the abrupt change in slope of the overall mismatched characteristic at the stalling ϕ of the baseline build. Figure 8 is the characteristic complete with hysteresis loop for the mismatched compressor. Figures 9 and 10 display the first stage characteristics for the baseline and mismatch builds. Figure 10 has specific operating points labeled for future reference. Note that the extended operating region of the first stage characteristic is positively sloped. Figure 11 shows the four individual stages in and out of stall for the mismatch build. Finally, figure 12 shows the first stage of the mismatch build broken down by direction of throttle motion. The standard stability analysis predicts that positive slope is unstable, negative slope is stable. However, the rear three stages are negatively sloped and the overall compressor is negatively sloped and stable. This shows the importance of both the local characteristic and the overall steady state characteristic.

The second variation from the baseline build was to open the first stage rotor clearance from gap/span=1.3% to 3.1% on the matched compressor. This was done in both a symmetric and an asymmetric fashion, the latter by only opening the clearance over a 120° section of the annulus. The clearance was opened to examine its effect on the stall inception process. The asymmetric clearance was used in an attempt to fix the circumferential location of the beginning of stall inception.

The final variation from the baseline that was investigated consisted of the matched build and a 120° circumferential distortion screen 1.5 radii upstream of rotor inlet [3]. Experiments were conducted both with the distortion screen fixed and with it rotating. As with the variable tip clearance, these experiments were carried out to investigate the effect of inlet distortion on the stall inception process, to try to force a time and length scale into the machine, and to try to circumferentially fix the starting point of stall inception. Figure 13 displays the various changes in the first stage characteristic associated with these rig changes.

Results

Steady State Data

The following set of data was taken with a slant wire. The sampling rate was 50 kHz. For the baseline build data were taken at 16 immersions from 2% to 95% and for the larger clearance data were taken at 19 immersions from 2% to 50%. The data were phase locked to the rotor. At each location and wire orientation 300 data sets were taken and then ensemble averaged resulting in the steady state results displayed here. The data are presented in two basic formats. The first format is a radial profile created by mass averaging the given quantity at the given radius over one circumferential pitch. The second format is to display the data in contour or vector format over roughly 1.5 pitch.

Discrepancies in the tip flow field for runs at different operating points can clearly be seen by examining radial velocity profiles. Figure 14 shows radial profiles of radial velocity for various fixed operating points. (The radial velocity should be nearly equal to zero everywhere.) The flow field in the tip region at rotor inlet for the extended operating region of the mismatch build was out of the calibration range for the slant wire and, as a consequence of this, the measured velocities in that region are incorrect. However, useful information can still be obtained from this data. The plot shows that the tip flow field does not deviate far enough from the expected direction (ie. radial velocity small) to be out of range until operating at point J of the mismatch build, which is the baseline stalling flow coefficient. As the flow coefficient decreases further, an increasingly large portion of the tip flow field is out of range for the slant wire and physically impossible radial velocities are shown. It should be noted that at rotor exit the flow field was not out of range of the slant wire.

The effect of changing operating point on specific flow structures, such as the tip vortex, blade wakes, and endwall boundary layers can be seen by viewing the data in a direction aligned with the relative flow. To display all three components of velocity, the results will be presented, first in vector format, and then in contour format. Three operating points will be examined. Figure 15 is a display of the slant wire data at rotor exit. The data has been converted to the relative frame and is viewed at a yaw of 55° from axial. This viewing angle is aligned with the bulk through flow and figure 15 thus represents the secondary flow. The scale vector at the top shows the direction of rotor rotation and the magnitude of tip speed. The blade wakes and tip vortex/jet flows are clearly visible. This figure is representative of the baseline operating points away from stall. Figure 16 is a similar plot at the last stable operating point before stall in the baseline build. Note the difference in the tip jet/vortex flow from the previous plot, with the tip leakage jet now extending to a lower radial immersion. Figure 17 shows the flow in the extended operating region of the mismatch build, at a lower flow coefficient than the baseline stall, but well above the mismatch stall point. Figure 17 is representative of other operating points in this flow regime; it is also very similar to figure 15. Thus the steady state, rotor locked, secondary flow field at rotor exit is relatively unchanged with operating point, except immediately before stall (as in figure 16).

The through flow velocity corresponding to the secondary fields of figures 15, 16, and 17 is displayed in figures 18, 19, and 20 in contour format. The low velocity region inside the constant contour of $v/U_{tip} <.45$ has been shaded in the three figures and the pronounced change in the tip region between points D and K is revealed.

Similarly, the effect of changing operating point on the axial velocity field is examined by first looking at circumferential and then radial profiles of axial velocity. Figures 21 and 22 show the axial velocity distribution at 50% immersion (mid-span) at rotor exit for roughly 1.5 pitch. It is seen that the rotor wakes do not grow very much circumferentially in θ as ϕ decreases. The radial profiles of axial velocity also reveal the changes in the tip flow field due to the change in stage 1 tip clearance. Figures 23 and 24 display the axial velocity profiles for three operating points at rotor inlet and rotor exit for the baseline and larger first stage tip clearance cases. There is an increase of axial flow deficit in the 20% of span nearest the tip with the larger clearance.

To summarize the steady state data, as ϕ decreases the tip vortex/jet structure and rotor wakes do not change appreciably. However, just before stall the rotor leakage jet does become larger. Furthermore, for the mismatched case, starting at the baseline stall flow coefficient, a region of tip flow that deviates from design, grows radially in a monotonic fashion with decreasing flow coefficient at first rotor inlet. Finally, the larger tip clearance build had a larger axial velocity deficit in the tip region, than the baseline build.

Unsteady Data

Baseline Build

This data was taken with the array of hot wires and pressure transducers discussed earlier and displayed in figures 2 and 3. Unless specifically noted, the hot wires are aligned perpendicular to the axial direction. The hot wires were always perpendicular to the radial direction.

This first section will examine the stalling process in the baseline build. To document this process as completely as possible, a represenative experiment at both the rotor inlet and rotor exit are presented. Figure 25 shows time traces for the eight equally spaced casing pressure transducers at rotor inlet, while figure 25b is at rotor exit. The probe numbers increase in the direction of increasing θ in the rotor rotation direction. The probe numbers of the ordinate locate the zero level for each probe. The time is in units of rotor revolutions. The data has been normalized, i.e. the mean removed and rms standardized to 1. All pressure transducer measurements are guage, relative to ambient. Figure 26 is the time histories of the testing hot wires at rotor inlet and 20% immersion corresponding to figure 25. Figures 25 and 26 are for the same stall event. (Figures 25b and 26b, both at rotor exit, are for the same stall event, which is similar to that of Figures 25 and 26.) The compressor was set at a stable operating point close to stall. The throttle was then slowly closed until the machine went into stall. The pip is first visible at t~76.5 on pressure transducer number 5 in Figure 25. The growth of this pip in amplitude and θ is clearly seen over the next few rotor revolutions, resulting in a mature stall cell by t~82. In these two figures (25 and 26) there are no apparent propagating disturbances prior to time~76.5.

Additional analysis of the pressure transducer data at rotor inlet shown in figure 25 is presented in figures 27 through 30. Figure 27 again displays the time traces of figure 25, but without the data being normalized. The negative mean values are explained by the fact that the probes are measuring gauge pressure and the flow has already accelerated through the IGV row. The coarser nature of figure 27 is due to the fact that only every twelfth data point was plotted. This technique of plotting every nth point was used for most figures to speed up the process of obtaining hard copies. In all cases there is no major difference between plots with every single point and those with only an integer fraction of points. Guidelines have been drawn in figure 27 and the slope of these lines represents the speed of propagation of the disturbance around the annulus. The change in slope of these lines displays the change in the speed of propagation of the disturbance as it decelerates from 70% of rotor speed at inception to 45% as a mature stall cell. The direction of propagation is in rotor direction. As stated earlier, prior to time~76.5 there is no sign of any disturbance, propagating or fixed. Various tools for data analysis such as FFTs, cross correlations, and filtering techniques, both with software and physically, (by looking at signals "far" upstream from rotor inlet), could not find evidence of any waves traveling at other than 70% speed prior to stall. More specifically, no modal disturbances above the perturbation levels of $v'/U=0.5\%$ $p'/\rho U^2=1\%$ could be found. Furthermore, these techniques confirmed the pip's 70% initial speed and subsequent deceleration to 45% as it grew in magnitude and circumferential extent.

An example of the spatial Fourier technique is shown in figures 28 and 29. At each time in figure 27 the data from the eight equally spaced probes was Fourier transformed and the resulting magnitudes and phases for the various harmonics are displayed. The size of the symbols in figure 29 are scaled by the magnitudes of figure 28. The phase in figure 29 is calculated using θ=arctan(Im(Cn)/Re(Cn))/n and thus the range for each harmonic decreases. This also gives a positive slope for motion in the direction of rotor rotation. In figures 28 and 29 the zeros for the various harmonics are offset for clarity. These figures confirm that there is nothing visible prior to time=77, at which point the disturbance grows and matures within roughly five rotor revolutions. Furthermore, the continuous change in slope of the first harmonic phase indicates the deceleration of the pip. The regular pattern seen for time<77 in harmonic one is attributed to a rotor asymmetry.

The data from figures 25 and 27 were also examined using correlations. Figure 30 is an autocorrelation of the first probe from figure 25 taken over the time period 65<t<75. This correlation clearly shows the strong once-per-revolution signal seen in the first harmonic of figure 29 and the 54 overtones of the rotor blade passing. However, there is no sign of any other traveling disturbance.

Some experiments were conducted with the eight equally spaced test wires alternating between hub and tip, 80% and 20% immersion. Figure 31 displays the results from one of these tests conducted at rotor inlet. This plot allows the three dimensional nature of the pip to be seen. Between t~77 and t~78 the pip is seen as an axial deficit traveling in the tip region, with no disturbance visible in the hub wires. Only when the tip deficit disturbance has grown to an appreciable extent is any disturbance visible at the hub, t~78.5. This hub disturbance is first seen as a flow increase, to compensate for the tip blockage, but as the pip grows into a stall there is eventually a full span deficit.

To obtain information about the flow direction within the pip an experiment was conducted with seven testing wires distributed over a three-pitch circumferential region at the rotor inlet tip, 20% immersion. (The eighth wire malfunctioned.) These seven wires were oriented at various angles between 0° and 180° in the x-θ plane, as displayed in a schematic in figure 32. Wire 1 is aligned to measure axial flow, while wire 4 is aligned to measure circumferential flow. Again, the zero level for each trace corresponds to the probe number on the ordinate. The following observations are consistent with the turning of the flow in the counter rotor direction due to a flow perturbation in the -x,-θ direction. First, the increase in the signal of wire 4 and the decrease in the signal of wire 1 indicate a flow turning, or an axial deficit and circumferential increase. The stronger deficit on wires 5-7 than 2 and 3 implies that the flow is turned so as to be more parallel with wires 5-7. An increased tip leakage jet would be a perturbation having components in both the negative axial and circumferential directions.

The unsteady measurements with the baseline build show that this machine stalled via radial and circumferential growth of an initially small length scale disturbance. The growth occurred in less than five rotor revolutions and no modal signals or any other type of precursors could be found. The disturbance's initial speed of 70% decelerates to 45% as it grows into a mature stall cell. This disturbance begins as a tip deficit and as it grows has a corresponding hub increase in local flow, before becoming a full span deficit at stall. At 20% immersion at rotor inlet the disturbance appears as a turning of the flow in the anti-rotor direction.

Unsteady Data

Mismatched Build

Starting at the baseline stall flow coefficient, a set of experiments conducted in the mismatched build at fixed operating points of decreasing flow coefficient are now presented. As the throttle was closed for the mismatched build, the following sequence of events occurred. When the flow coefficient had decreased to the level of the baseline stall, pips would appear and disappear sporadically. Figure 33 displays the normalized traces from eight equally spaced hot wires at 20% immersion at rotor inlet obtained for the fixed throttle setting, J, baseline stall. Note that for most of the time the wires are relatively clear. However at time~37, wires 6 and 7 display a pip. Figure 34 is another experiment under these same conditions and the presence of a disturbance is seen between time =20 and time=25. Figure 35 is an expanded view of probe #2 from figure 34 showing the pip over about 2-3 blade pitches. For comparison, figure 35b is a similar plot for fixed operating point M. There are now more pip disturbances, the mean velocity has decreased, and the pip width is now 3-4 pitches.

As the flow coefficient continues to decrease from J, the pip disturbances become more regular and do not decay after a short appearance, but persist. Time traces, FFTs, and correlations all show that the disturbance signal becomes regular, and travels at roughly 70%. For example, figure 36 again represents the time traces from the eight equally spaced testing hot wires at rotor inlet at 20% immersion. The steady state operating point is L. Note that there are 5 pips, not equally spaced about the circumference, traveling around the annulus at 70% speed. As the flow coefficient is reduced further more and more pips appear around the annulus, all traveling at roughly 70% speed. Eventually, at operating point N there are 12 pips traveling about the annulus at 70% as shown in figure 37. Any further decrease in ϕ and one of these 12 pips grows into rotating stall in the same fashion as the baseline case. These disturbances in the extended first stage region may be part span stall cells rather than precursor pips.

The signal at roughly nine times rotor speed established by the twelve disturbances travelling at approximately 75% speed is clearly displayed by the twelve signals between t=22 and t=23.4 and the nine signals between t=22 and t=23 in figure 37. Figure 37b is an autocorrelation of probe#1 in figure 37, showing a correlation at roughly 70% speed. Furthermore, the 12 coherent disturbances that are travelling about the annulus are seen as the 12 peaks between 0 and the 70% speed marker. The 9 peaks between 0 and delay time=1, lead to a perceived 9 times rotor speed signal. Figure 37c is a temporal FFT of probe #1 from Figure 37, which also shows the resultant nine times rotor speed signal. A comparison of Figure 2-9 from [4] with temporal FFTs such as Figrue 37c and others at fixed operating points between J and N, suggest that perhaps a similar situation of several disturbances travelling about the annulus also existed in [4].

To obtain some radial information, experiments were conducted with the testing hot wires at rotor exit, in the hub/tip (80% and 20% immersion) configuration. Figures 38 and 39 show different time periods from the same experiment of the mismatched compressor. Crosscorrelations show that the pip speed was roughly 73% and appropriate guidelines have been sketched. The compressor was set close to stall, and the throttle slowly closed until the machine stalled at about time~74. From these figures it is seen that as in the baseline case, the pip disturbance gives a deficit in tip axial velocity and hub increase in axial velocity until the disturbance becomes full span at rotating stall onset. Furthermore, the time traces from the hub wires clearly show the blade passing signal even during pips. Using these blade wakes as a reference, and remembering that the disturbance is traveling at 30% speed relative to the rotor, it can be seen that the pip disturbance's circumferential size at the hub is on the order of one or two pitches.

More information about the travelling disturbances is presented in the flollowing three experiments that were carried out at operating point K of the mismatch build. Figure 40 is the time trace from a testing wire at rotor exit at the hub for fixed operating point K. This again shows that the pip disturbance takes the form of a flow increase at the hub, and that it is only one or two blade pitches wide. Finally figures 41 and 42 show hot wire traces from rotor inlet at 5% and 30% immersion respectively for the fixed operating point K. For these two runs the hot wires were packed over a 3 pitch region, and they alternated between their standard orientation, perpendicular to axial, and parallel to axial. The hot wire orientations are displayed in the right margin of the figures . Looking, for example, at the traces from probes 1 and 2 it is observed that the pip disturbance appears as an axial flow deficit and a circumferential flow increase. Figure 42 shows that the disturbances are less visible at 30% immersion.

The mismatch does extend the stable operating region of the first stage. At the matched baseline stall flow coefficient sporadic pips intermittently appear. As ϕ is continuously decreased from this point, the pips stay and travel at roughly 70% speed. These disturbances are a few blade pitches wide, and are not necessarily equally spaced about the annulus. More disturbances appear around the annulus until prior to stall there are 12 around the circumference. Eventually one of these grows into stall in a similar fashion to the baseline case.

These disturbances in the stabilized first stage of the mismatch build have four similar features with the transient pips that grow to stall in less than five rotor revolutions for the same rotor in the baseline build. Both disturbances appear first at point J and travel at a speed of roughly 70%. Both disturbances have a radial profile of a tip deficit and a hub increment in flow. Finally, the circumferential size (few pitches) of the stabilized disturbances of the mismatch build is comparable to the size of the pip disturbance of the matched baseline build, early in its growth towards stall. That is, the stabilized disturbance of the mismatch build resembles the baseline transient pip at some time during its five rotor revolution growth period. Based on these similarities, the stabilized disturbances of the mismatch build and the transient disturbance of the baseline build appear to be the same phenomena, although this has not been proven conclusively.

In the artificially stabilized region, the local first stage characteristic is positively sloped, and the flow in the first stage becomes unstable at about the condition where pips first appear. The pips left to their own accord, would quickly grow into rotating stall. The pips are a local flow phenomena of small scale and for them it is this local characteristic which is important. However, the pips only grow a certain amount (few pitches) until they are at an appropriate length scale to feel the influence of the downstream stages (negatively sloped characteristic), and their size is effectively held in check. Hence above a certain size, the overall global characteristic becomes important. For this machine, this threshold length scale was a few pitches.

Unsteady Data

Variable First Rotor Clearance

The first rotor tip clearance was opened around the whole circumference from 1.3% to 3.1% to asses the effect of tip clearance on the stall inception process, and as an attempt to change the stall inception process to a modal type. This has been done in the past by Day [1]. Opening the first rotor clearance shifted the stalling ϕ from .345 to .352. This is seen in Figure 43 of the first stage characteristics. The stall inception process was the same as the baseline except that the initial pip speed was 62% based on correlations. As before, there is no evidence of any long length scale or slower traveling disturbances prior to stall.

To fix the starting point of stall inception and to examine local behavior around the annulus, the tip clearance over a 120° sector of the first stage was opened to 3.1% while keeping the remaining 240° at the baseline 1.3%. Figures 44 and 45 show that around the end of the large clearance region is where the steady pressure and local ϕ are minima. Figure 46 shows that this region is where the signal is the noisiest. The data was taken with the 10 testing probes and was averaged over 10 rotor revolutions. (The instantaneous results are similar) Viewing the two circumferential sections as two parallel compressors, operating on the respective speed lines of figure 43, it is clear that as ϕ is decreased the larger clearance section of the annulus (the notch) will reach its stability limit first. Therefore, it is expected that disturbances which are small in circumferential extent will begin and grow first in the larger clearance area and that this region should be the noisiest. As a result of this, even though the disturbances may be "born" in the high clearance region, they may not grow to an observable size until after passing through the low ϕ region at the end of the notch. This is indeed what is observed for example in figures 47 and 48. The disturbance labled X in figure 47, is first seen after being "born" in the 3.1% clearance region and growing through the high rms low ϕ region at the end of the notch. The disturbance is then damped in the baseline clearance region as this flow is operating at a relatively more stable point on its respective characteristic. A subsequent disturbance, Z, persists longer and travels at roughly 70% rotor speed.

Figure 49 displays the speed of propagation of the pip at various points about the annulus. The figure was created by crosscorrelating adjacent probes and plotting the result at a circumferential location half way between the two probes. The fact that the speed of propagation in the large clearance region is about 60% ,which is roughly equal to the speed for the symmetric large clearance, and that the speed in the tight clearance is roughly 70%, which is about the speed for the symmetric small clearance, confirms that, since the pip's length scale is small compared to the circumferential extent of each of the clearance regions, in each of these respective regions the pip behaves as if it was in a uniform clearance machine.

Unsteady Data

Distortion Screen

The distortion screen was used as a tool to force a length scale, to fix the starting location of stall inception, (similar to the notch tip clearance experiment), and to force a time scale (when the screen was rotated). The distortion screen covered a 120° sector and was 1.5 radii upstream of the rotor inlet [3]. At rotor inlet the shape of the velocity profile, Figure 50, is consistent with [4] and [5]. The lowest local ϕ occurs at the end of the screen and this corresponds with the highest velocity rms, Figure 51. Similar to the non-uniform tip clearance build, the pips are believed to be "born" and to grow in the low ϕ region at the edge of the screen. Then they are attenuated through the clean flow region as the local ϕ increases (Figures 52 and 53). (This agrees with [5] which states that the end of screen has the highest growth rate for propagating 2-D disturbances.)

The stall inception process is again the same as the other builds, and is displayed in figure 54. A short length scale disturbance traveling at roughly 70% speed grows and decelerates into a mature stall cell. There are no signs of long length scale, slower traveling modes. Note that the mature stall cell attenuates in the higher local ϕ of the clean region.

A final attempt to force modal stall was made by rotating the inlet distortion screen. Figure 55 displays stalling ϕ vs. screen speed. Counter rotation gives an increase in stall margin, ie. stall at a lower flow coefficient. There are two resonant speeds, at 20% and 70%, which decrease the stall margin. The 70% speed is the strongest resonant speed and corresponds to the pip speed. The 20% speed is similar to the predicted modal speed based on 2-D semi-actuator disc analysis.

The experiments seem to suggest the existence of two resonant speeds in a machine. The first speed, 20% corresponding to long length scale modes, and the second resonant speed, 70% corresponding to short length scale pips. The final mature stall cell speed is 45%. In light of the importance of these three speeds, 20%, 45%, and 70%, experiments were repeated with the full array of dynamic instrumentation and the screen moving at these key speeds. An example is shown in figure 56 where the screen is rotating at 20% speed in an attempt to force the long length scale modal path to stall. The screen's propagation is clearly visible. A pip begins at the screen border. The pip's speed is not 20%, but 70% (displayed by the difference in the slopes of the guide lines) which then decelerate to the 45% speed mature stall cell as it grows, following the baseline scenario. Similar results were obtained with the screen at 45% and 70% speed. That is, no modal stalls were observed, the pip would start at the screen border, the pip propagation speed was not effected by the screen speed, and the pip would grow into a mature stall cell in the same fashion as the baseline case.

Summary

This work has shown repeatedly that short length scale "pip" disturbances can play a key role in stall inception, independent of the longer length scale, slower traveling modes. For the pip-type of stall inception, the initial pip size is on the order of a few pitches and grows to full rotating stall within five rotor revolutions. The tip flow field has been shown to experience changes that grow monotonically in the radial direction as stall is approached. The pip flow structure in the tip region at rotor inlet manifests itself as a turning of the flow away from axial in the counter rotor direction. The rotor wakes and other secondary flow structures do not show any significant changes with operating point, except prior to stall.

At the small length scale of the initial pip, potential fields from various components of the machine are weakly coupled and as a result the stall inception and pip are influenced mainly by the local environment. However, once the pip grows past a threshold length scale, (few pitch), component coupling becomes more important and the overall environment thus ultimately determines whether the pip grows or decays. Coupling can thus be used as a tool to display the importance of the local environment and to filter out disturbances of different wavelength. These points were demonstrated with the mismatch, asymmetric tip clearance, and fixed distortion screen builds.

Finally, the pips were shown to be essentially 3-D, consisting of a region of circumferential size (at inception) on the order of a blade pitch, with a tip flow deficit. A hub increment in flow had to occur to satisfy continuity. A 2-D semi-actuator disc analysis for this geometry predicts modal propagation at roughly 20% of rotor speed. However, the pips are strongly 3-D, being of small radial and circumferential extent, and rotate at 70% of rotor speed. There is some empirical evidence to support the idea that axial flow compressors may have two natural frequencies, one near 20% speed, corresponding to the modes predicted by 2-D models, and a second at 70% speed, corresponding to the 3-D pips, and the particular type of stall inception is determined by which natural frequency dominates.

Future Work

Some evidence has been presented for the tip leakage jet as having a key role in the stall inception process. Real time directional data of the tip jet at rotor inlet is needed for a clearer and time accurate presentation of this tip jet flow. Instantaneous three component of velocity could be measured with a multi-sensor probe or with several single sensor probes arranged at various orientations and with restrictor shields to help clarify the direction of the flow.

A second experimental avenue to pursue is to measure the instantaneous local characteristic with hot wires and pressure transducers simultaneously at rotor inlet and exit at corresponding θ locations. With this technique, employed for example simultaneously in the notch and clean flow regions of the notched tip clearance build, a true instantaneous view of Figure 43 may be measured experimentally. Also, the instrumentation could be continued through the rig to determine the axial extent of the disturbances.

A third area that requires more investigation is the apparent presence of two natural frequencies in machines, their connection to the two paths to stall, (pips and modes), and determining which of these is dominant. A matrix of relevant parameters such as tip clearance, aspect ratio, spanwise loading, etc. should be assembled for various modal and pip machines. Any trends observed in this parameter space (such as going from baseline clearance to a larger clearance on all stages) should then be employed to convert a machine from pip to modal, or vice versa. Once this is achieved, the resonance experiment with the moving distortion screen should be repeated to determine if indeed the dominant frequency changes between the two natural frequencies as the rig and corresponding stall inception changes are carried out.

Finally, taking note of the three dimensionality of the flow as displayed in figure 31, future modeling of the stall inception process should incorporate the presence of radial harmonics, radial distributions.

References

[1] Day, I.J., "Stall Inception In Axial Flow Compressors", ASME paper 91-GT-86, 1991.

[2] Wisler, D.C., "Core Compressor Exit Stage Study," Volume IV, Data and Performance Report for the Best Stage Configuration, NASA CR 165357, April 1981

[3] Plumley, R.E., 1990, "Unsteady Compressor Distortion Response and Compressor Instability," M.S. Thesis, Department of Aeronautics and Astronautics, MIT.

[4] Longley, J.P., "Inlet Distortion and Compressor Stability," Ph.D. Dissertation, Cambridge University Engineering Department, 1988.

[5] Hynes, T.P., and Greitzer, E.M., "A Method for Assessing Effects of Circumferential Flow Distortion on Compressor Stability," ASME Journal Of Turbomachinery, Vol. 109, July 1987, pp. 371-379.

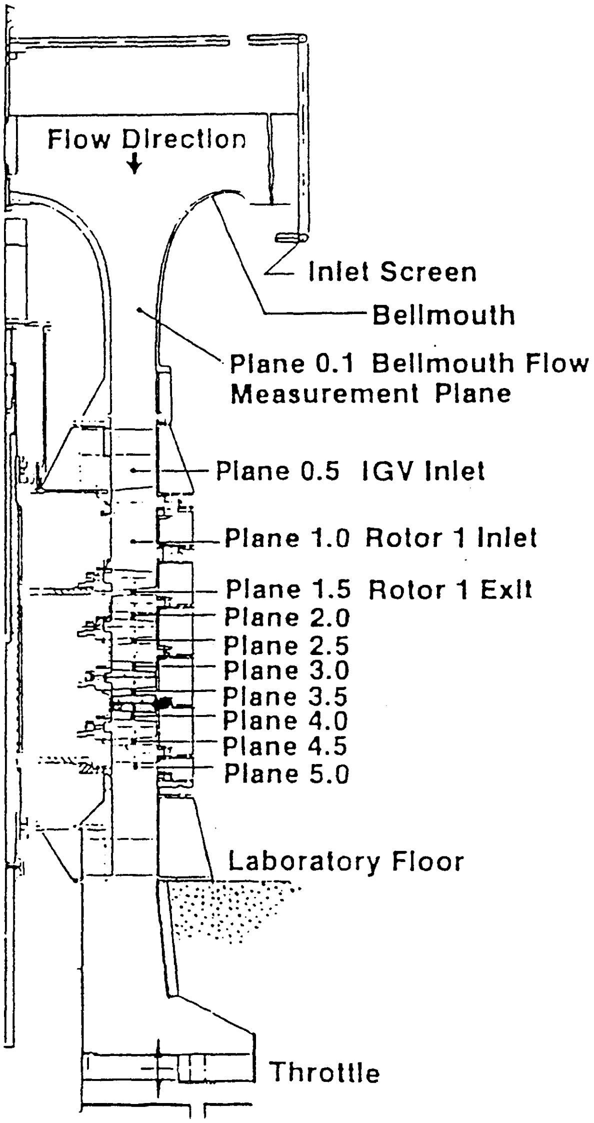

Figure 1: Cross-Section of Low Speed GE Research Compressor.

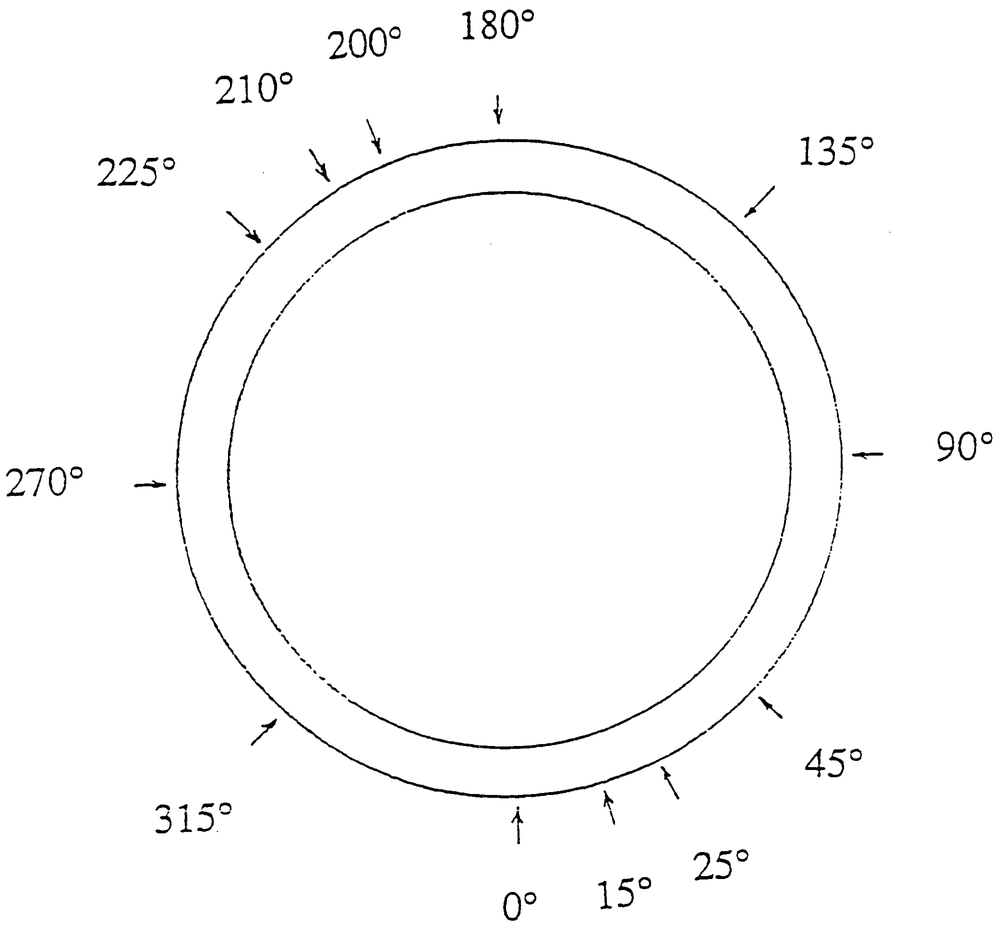

Figure 2: Axial view of instrumentation. Circumferential map of hot wire and pressure transducer locations.

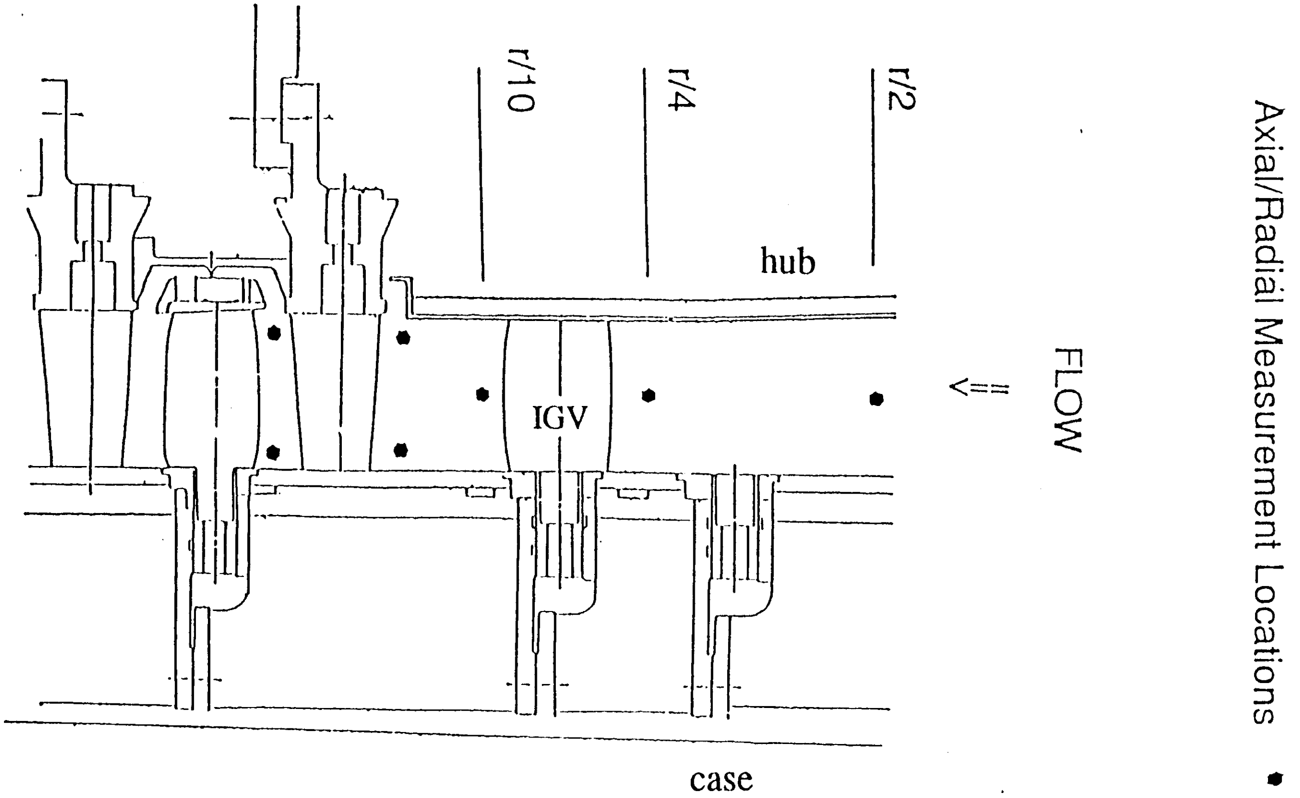

Figure 3: Detailed view of flow path including IGVs and first stage.

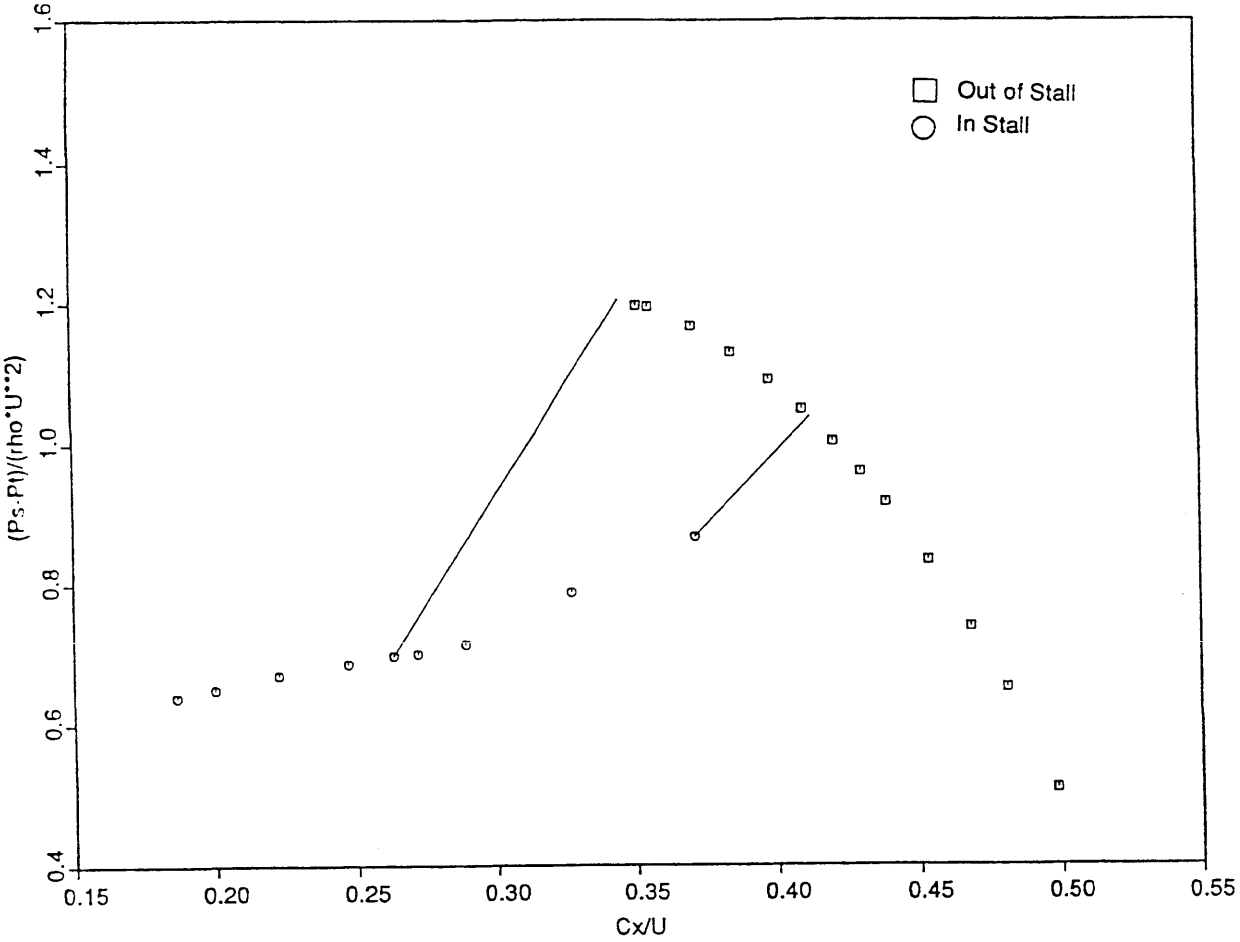

Figure 4: Baseline build overall characteristic showing hysteresis loop, including in stall and out of stall operating points.

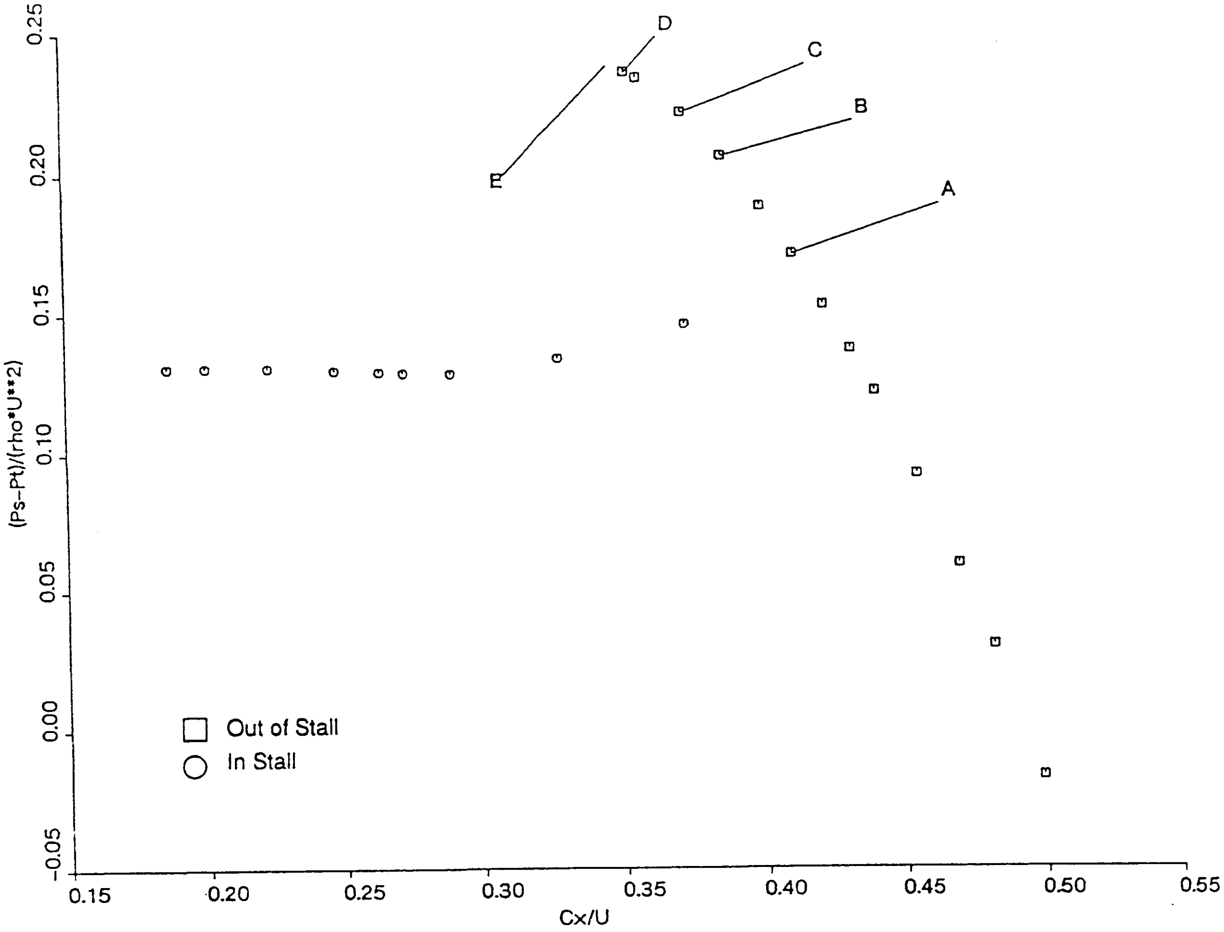

Figure 5: Stage 1 characteristic of baseline build. Several points are labeled for future reference. Point A is design and point E is just before stall.

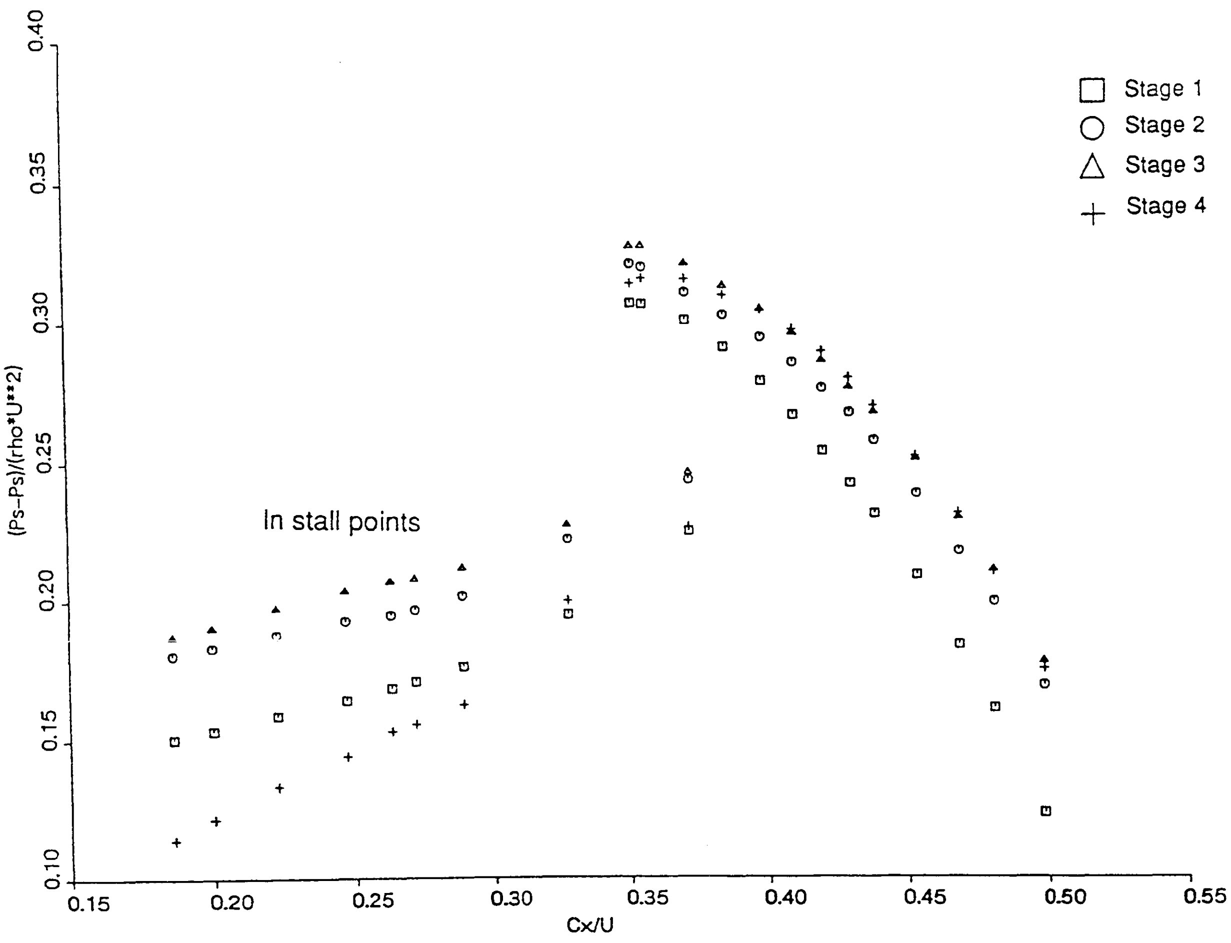

Figure 6: Individual static pressure rise characteristics for all four stages of the baseline build.

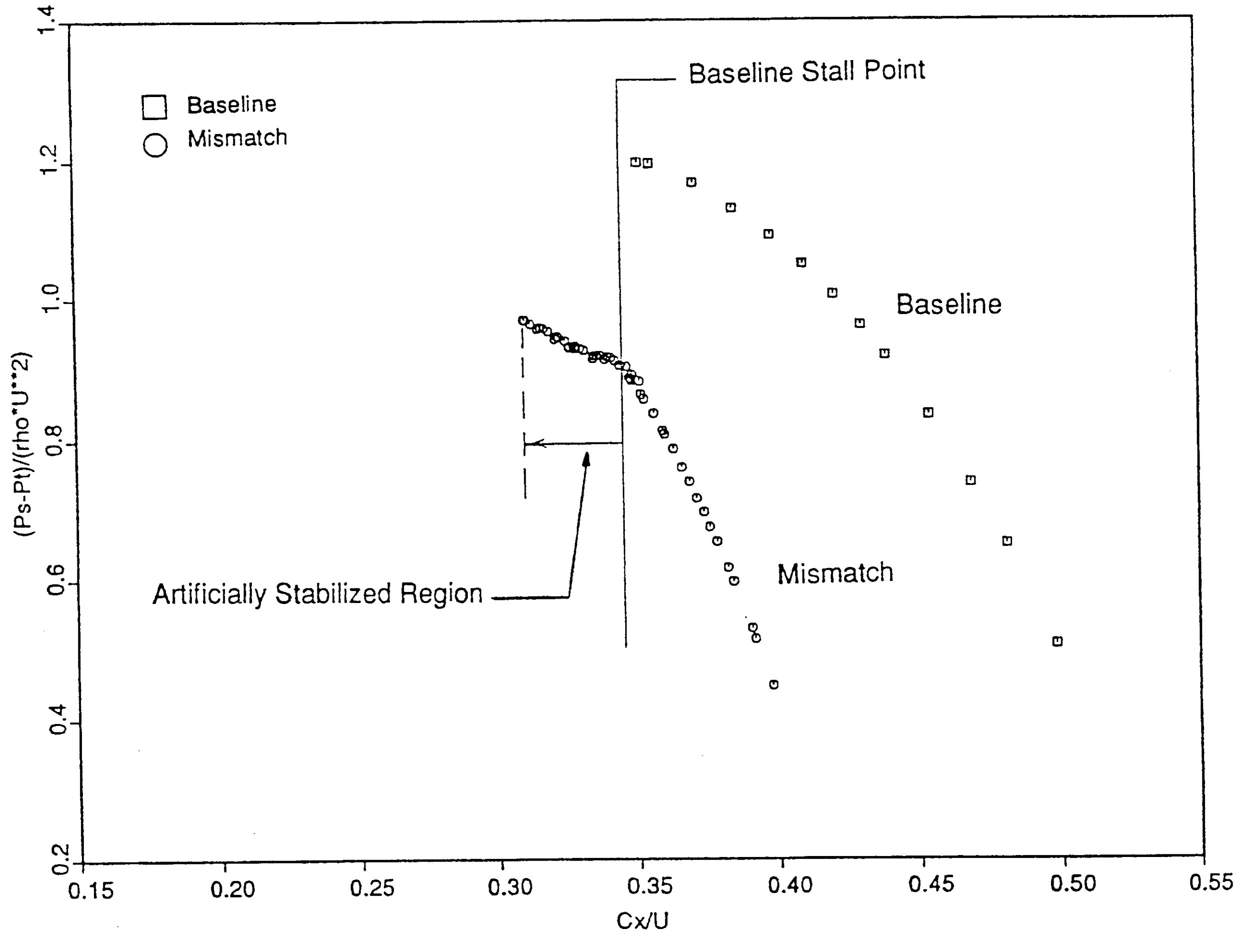

Figure 7: Overall characteristics for baseline and mismatch builds. Mismatch was created by closing the rear three rotors by 10 °
Note the extended stable operating region of the mismatch build, and the abrupt change in its characteristic's slope at the baseline build's stalling flow coefficient.

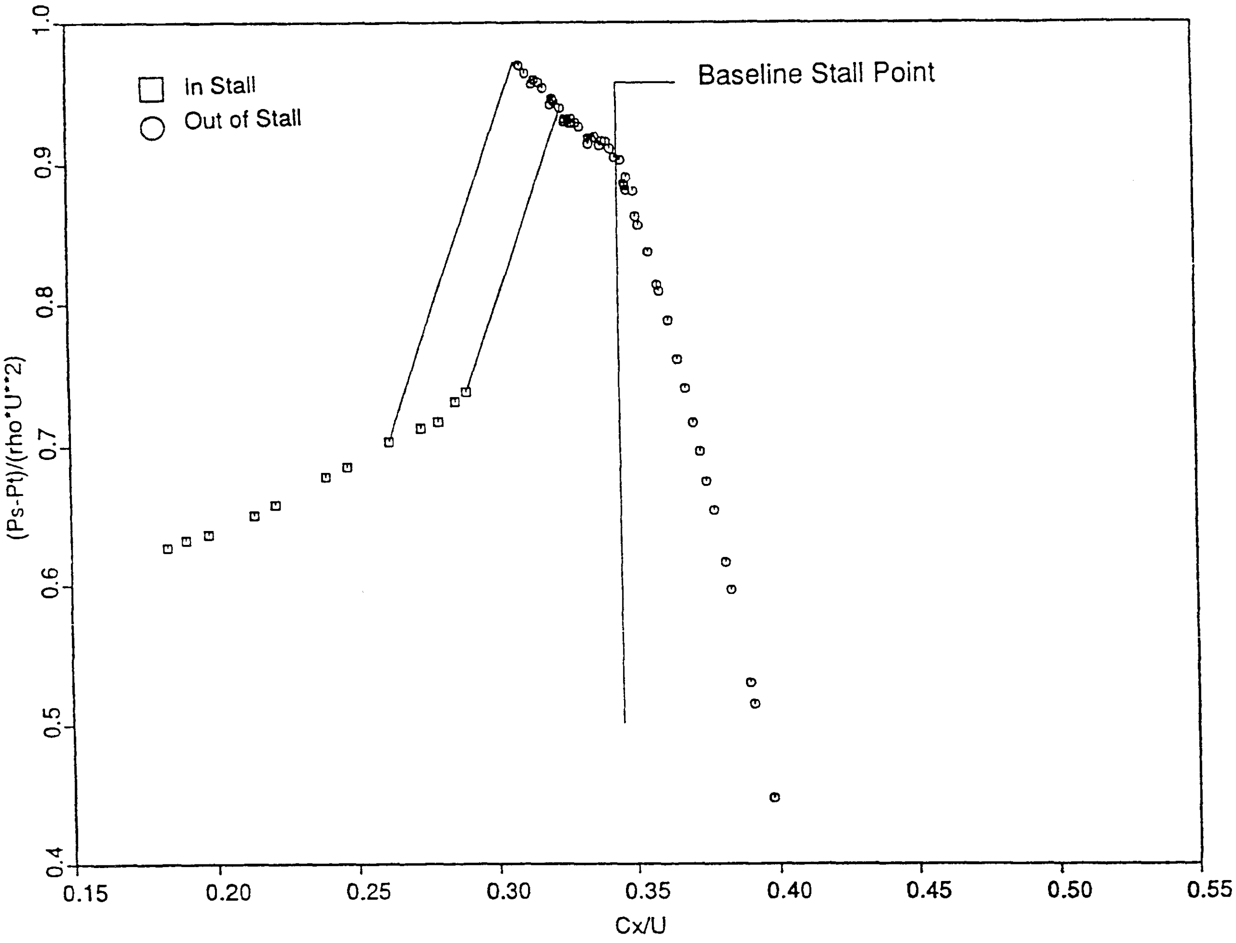

Figure 8: Mismatch build overall characteristic showing hysteresis loop, including in stall and out of stall operating points.

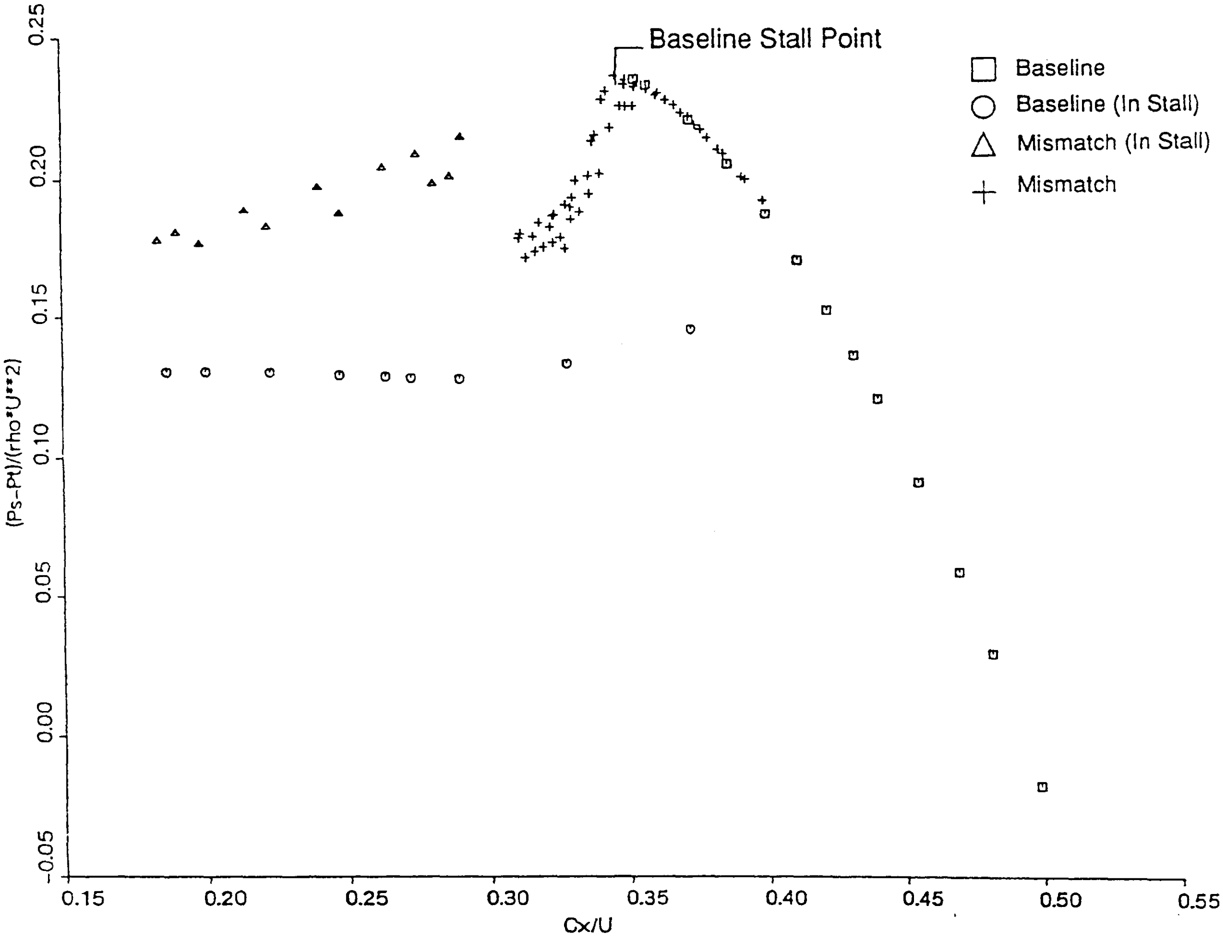

Figure 9: Stage 1 characteristics of baseline and mismatch builds.

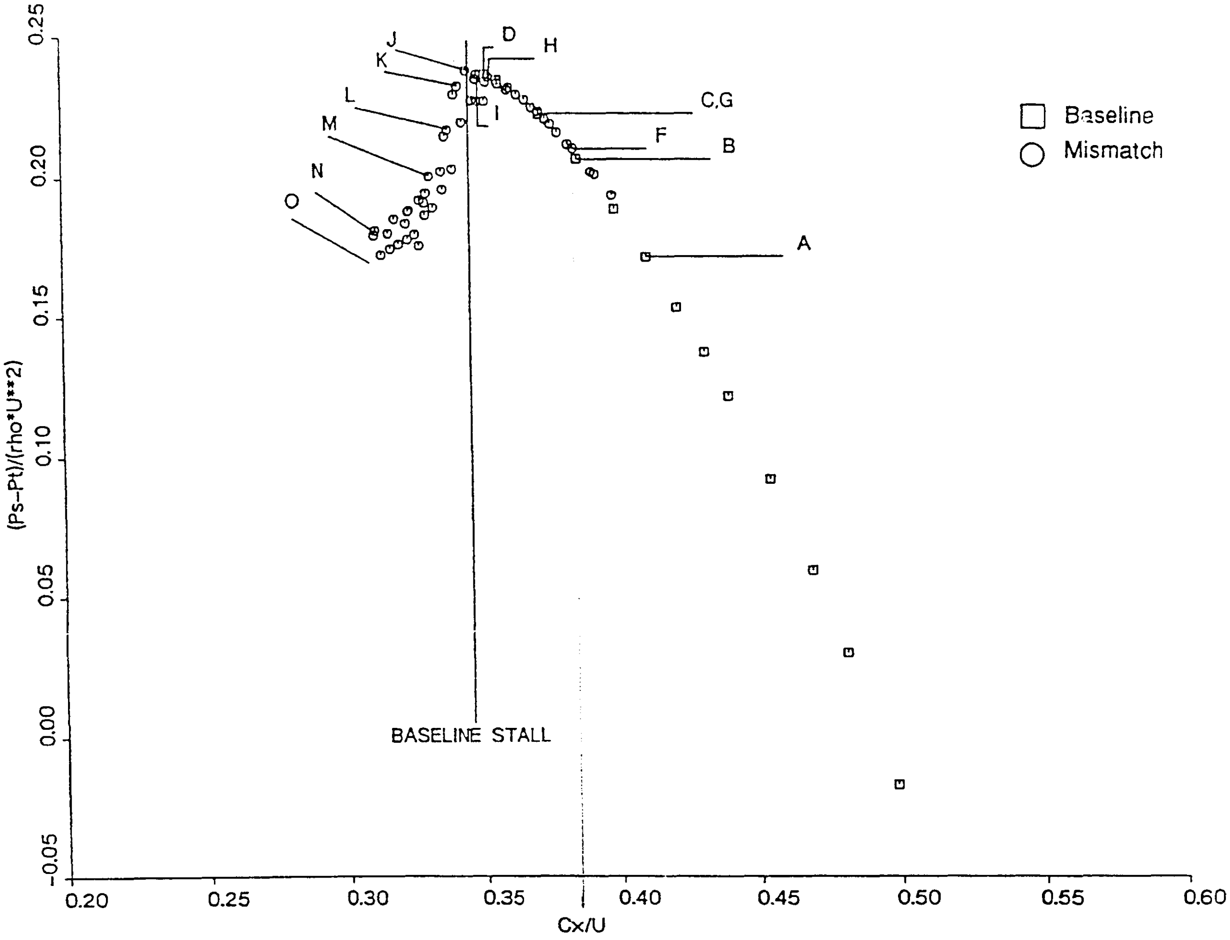

Figure 10: Stage 1 characteristics of baseline and mismatch builds. Specific operating points are labeled for future reference. Note that the extended operating region of the first stage characteristic is positively sloped.

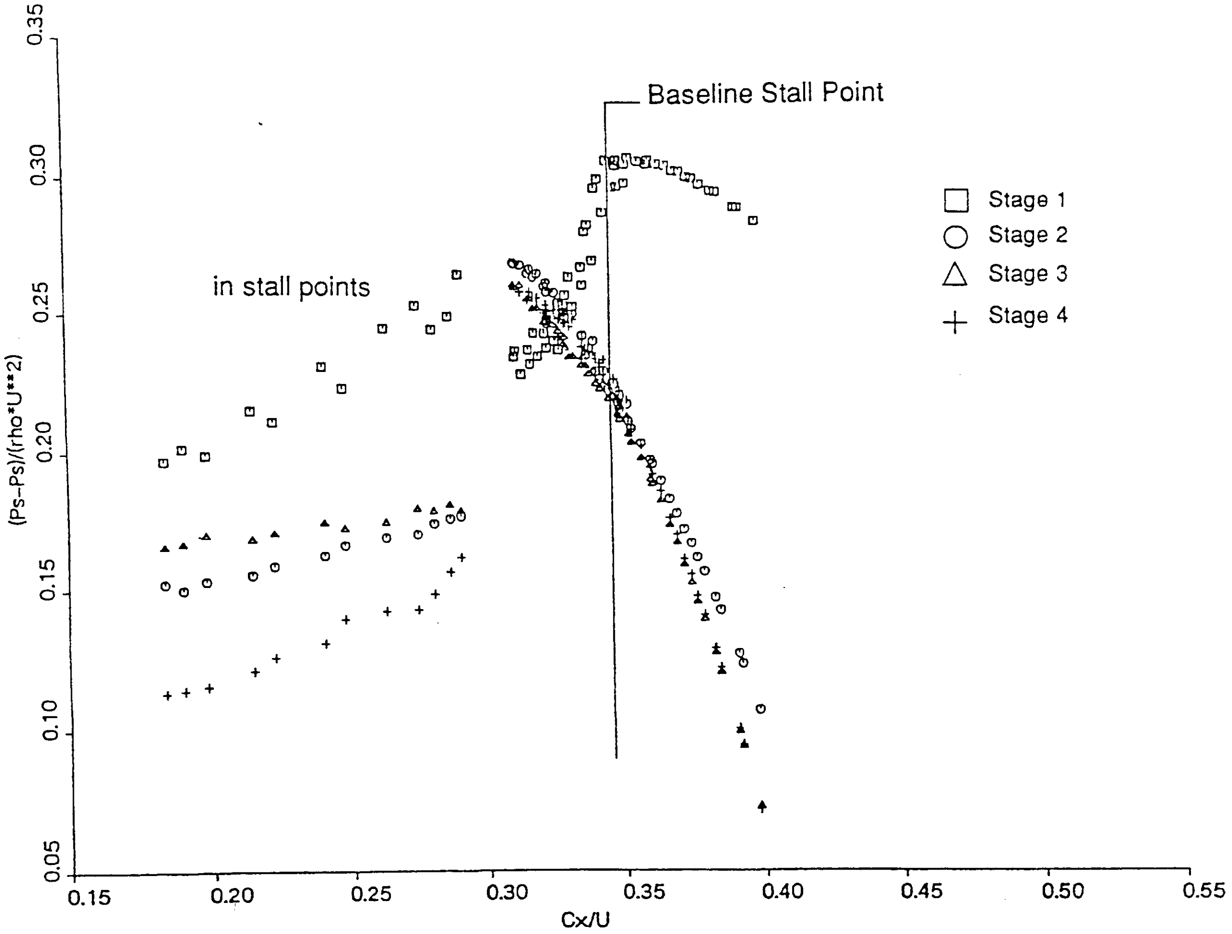

Figure 11: Individual static pressure rise characteristics for all four stages of the mismatch build.

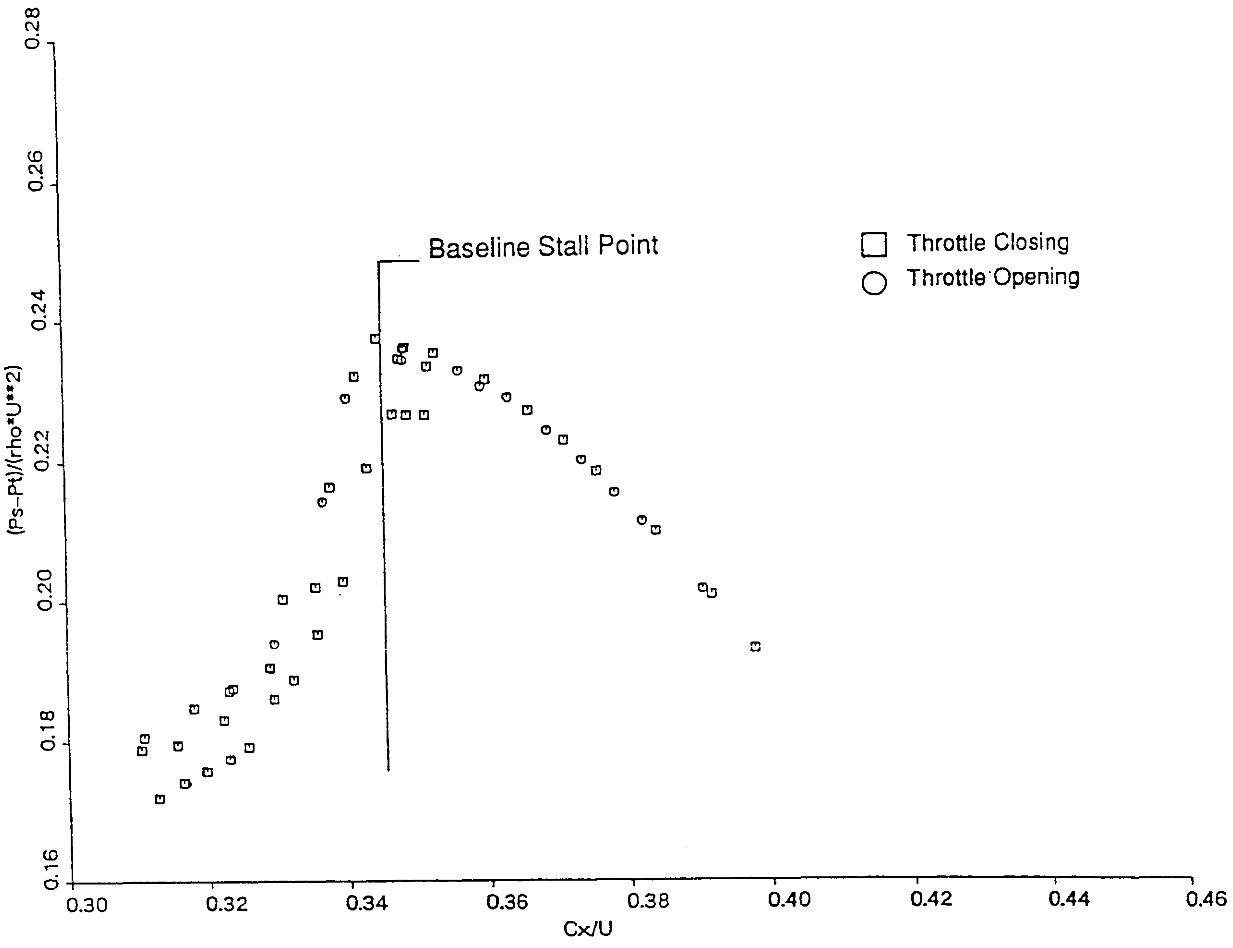

Figure 12: Stage 1 characteristic of mismatch build showing the effect of direction of throttle motion.

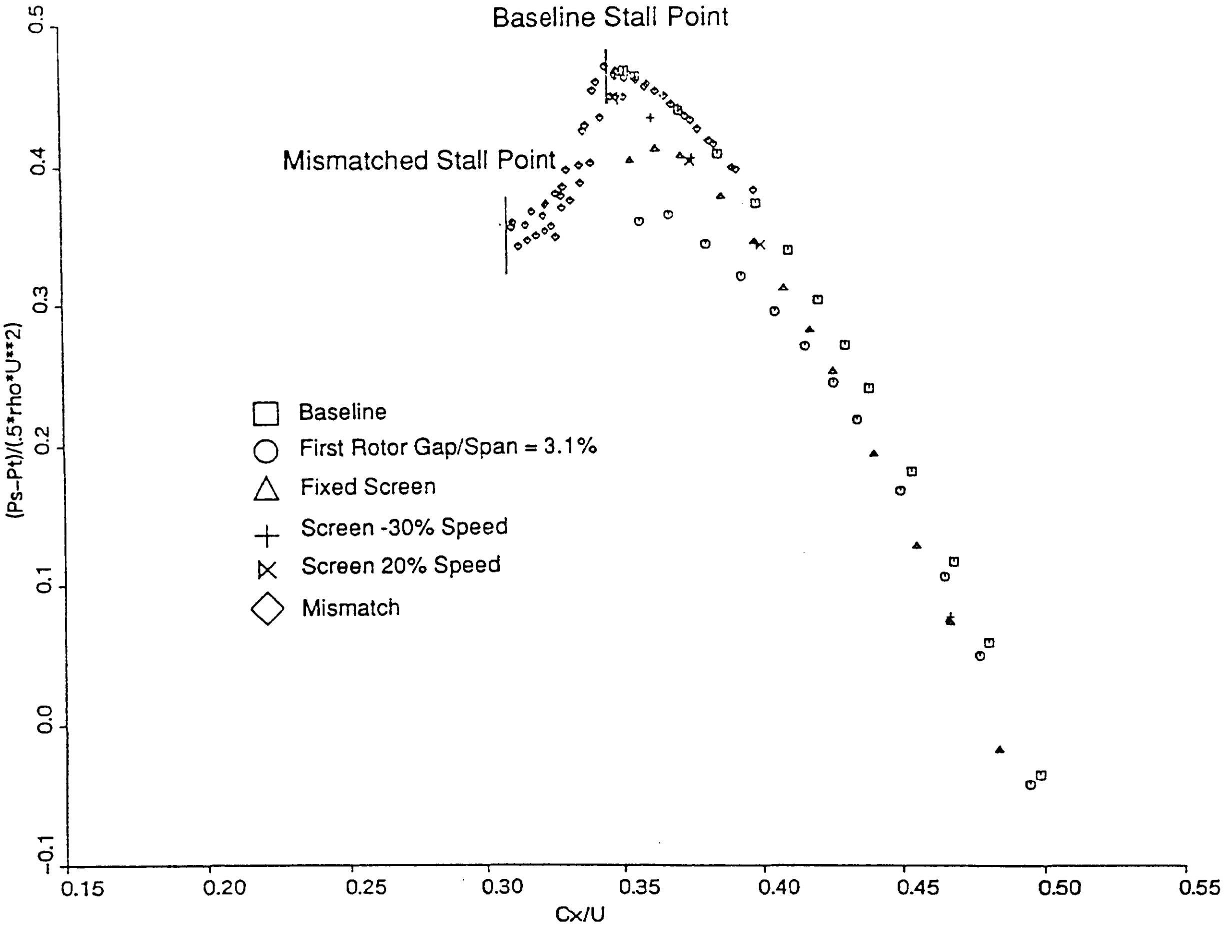

Figure 13: Summary of stage 1 characteristics for various builds.

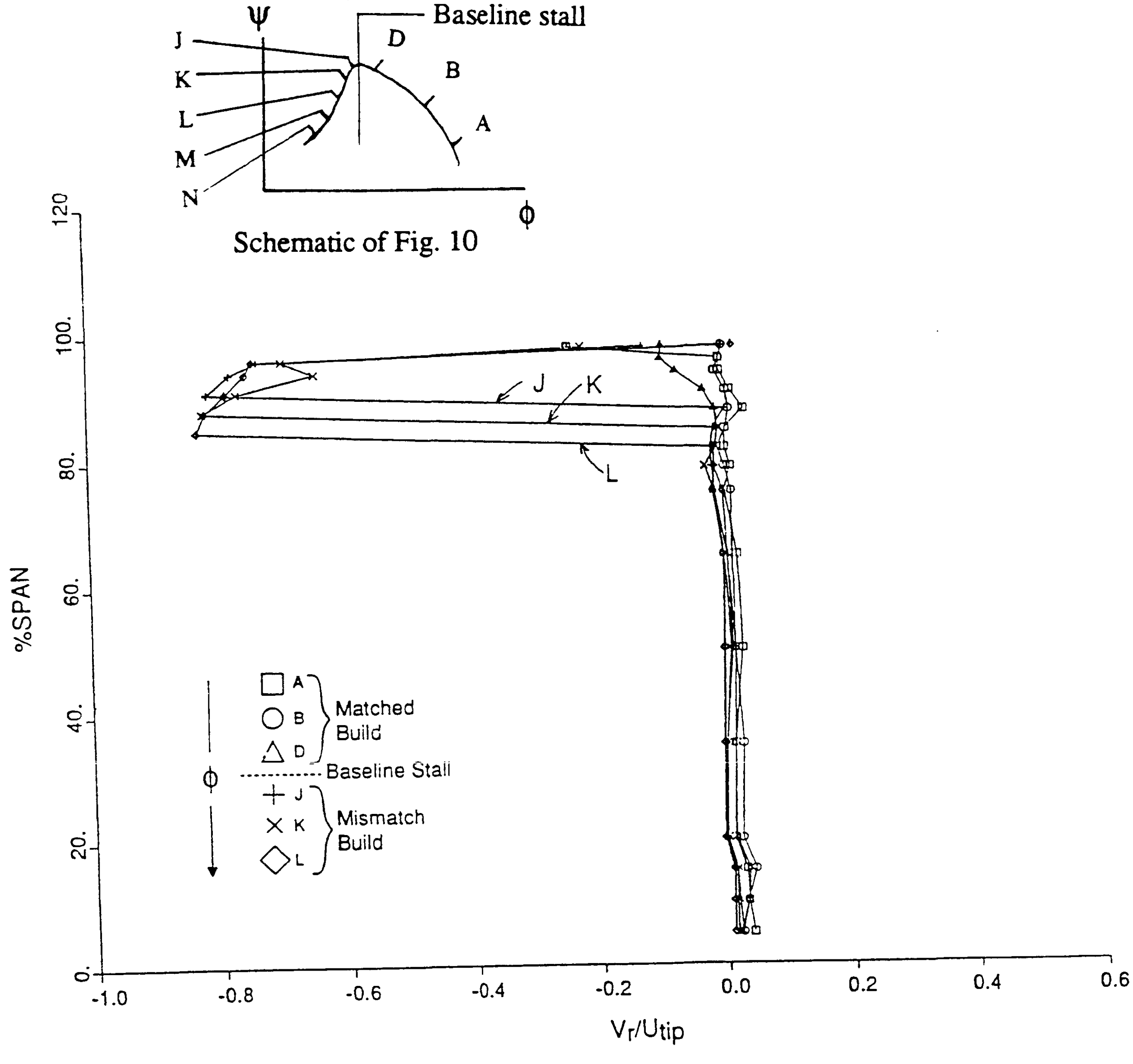

Figure 14: Radial profiles of circumferentially mass averaged radial velocity at rotor inlet. The operating points, A-L, correspond to those labeled in figure 10. The flow direction in the tip region for operating points J,K, and L deviated enough from the expected flow direction to be out of calibration range for the slant wire.

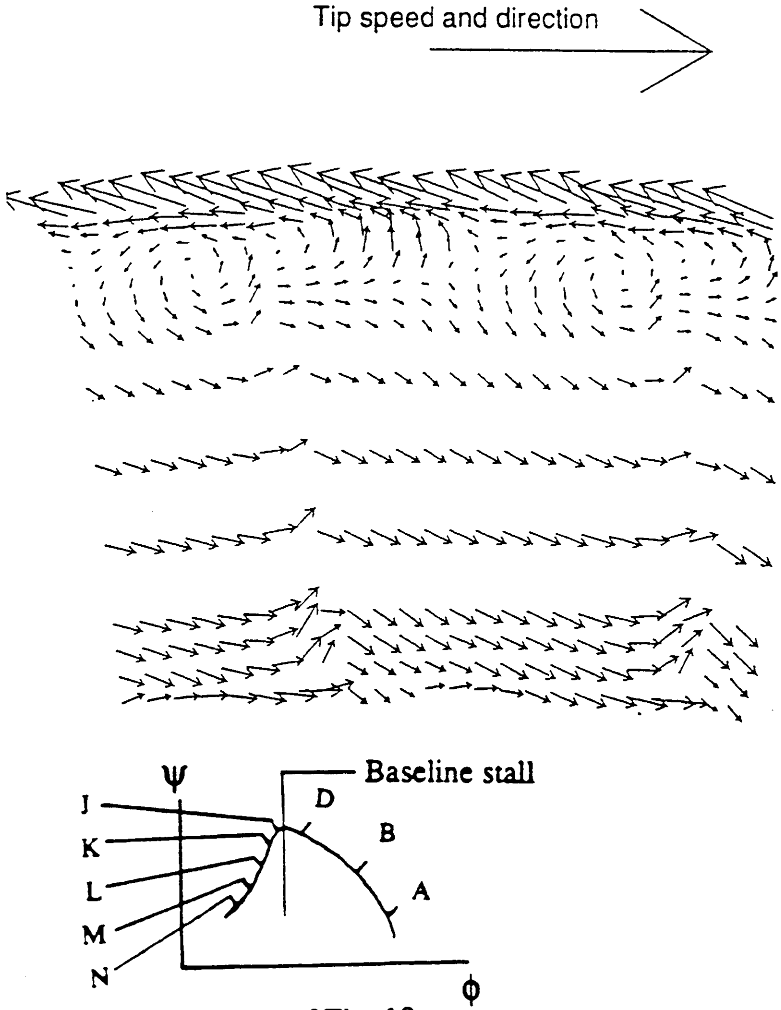

Schematic of Fig. 10

Figure 15: Secondary flow at rotor 1 exit in the relative frame. This is at a yaw of 55 ° from axial. Roughly 1.5 rotor pitches are displayed. Rotor blade wakes and tip vortices are visible. A reference vector, indicating tip speed and direction is included. Operating point B of figure 10.

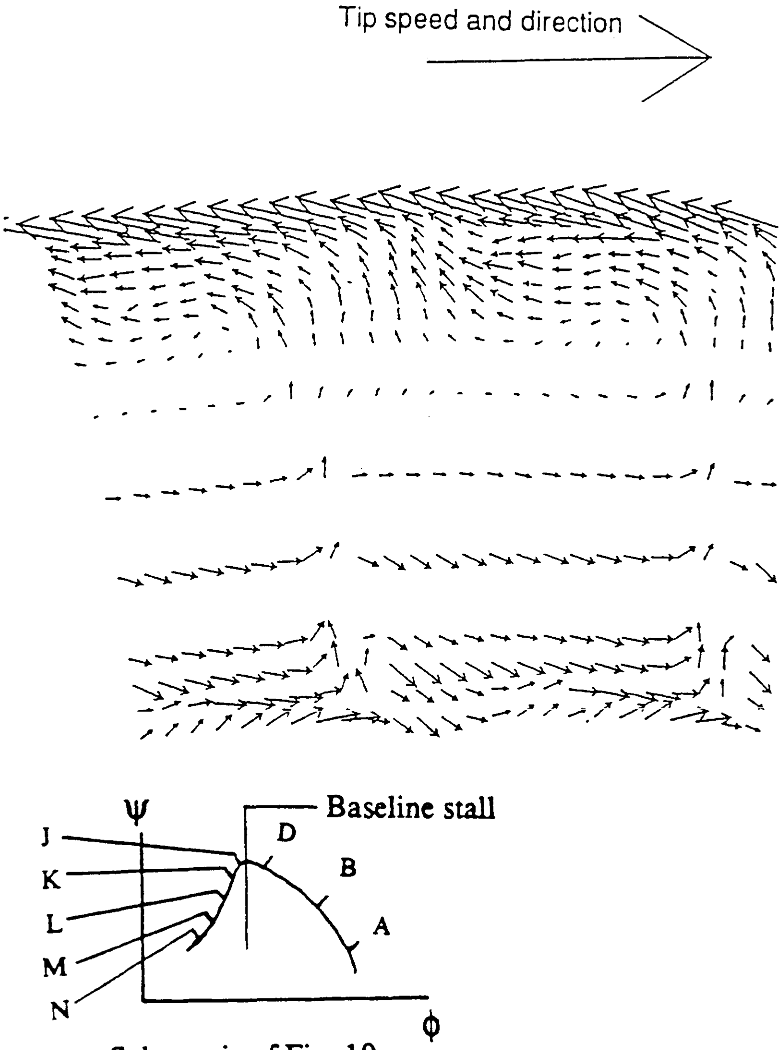

Schematic of Fig. 10

Figure 16: Secondary flow at rotor 1 exit in the relative frame. This is at a yaw of 55 ° from axial. Roughly 1.5 rotor pitches are displayed. Rotor blade wakes and tip vortices are visible. A reference vector, indicating tip speed and direction is included. Operating point D of figure 10, baseline build near stall.

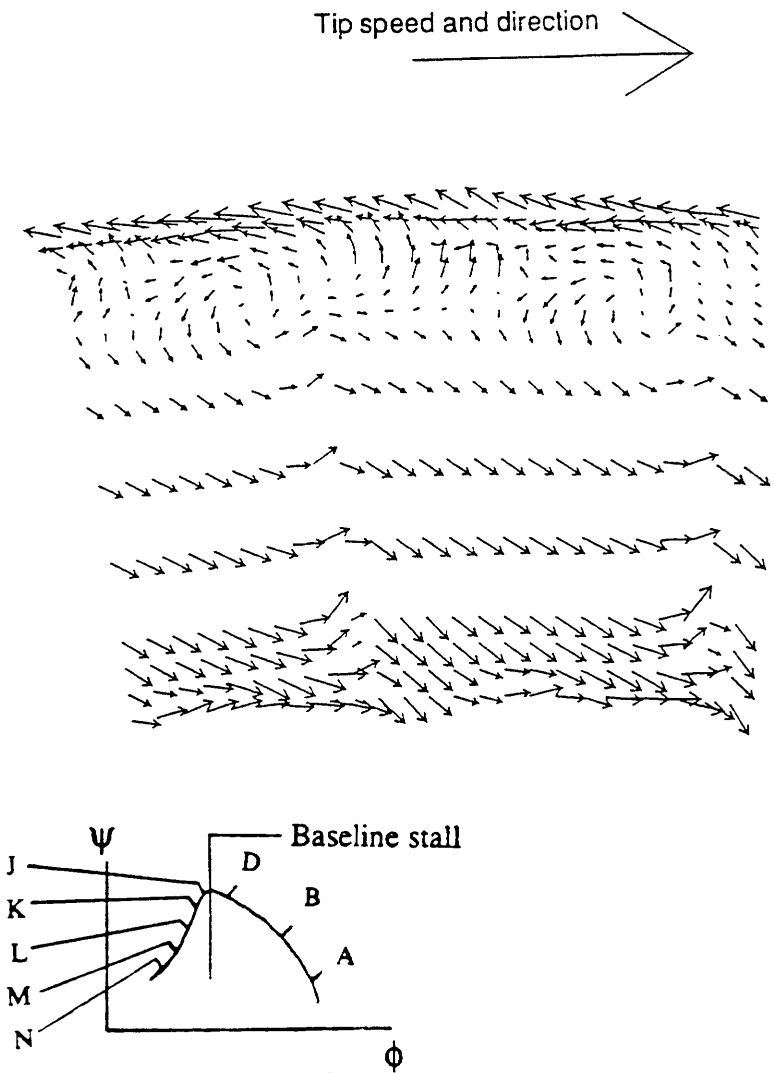

Schematic of Fig. 10

Figure 17: Secondary flow at rotor 1 exit in the relative frame. This is at a yaw of 55 ° from axial. Roughly 1.5 rotor pitches are displayed. Rotor blade wakes and tip vortices are visible. A reference vector, indicating tip speed and direction is included. Operating point K of figure 10, mismatch build in the extended operating region.

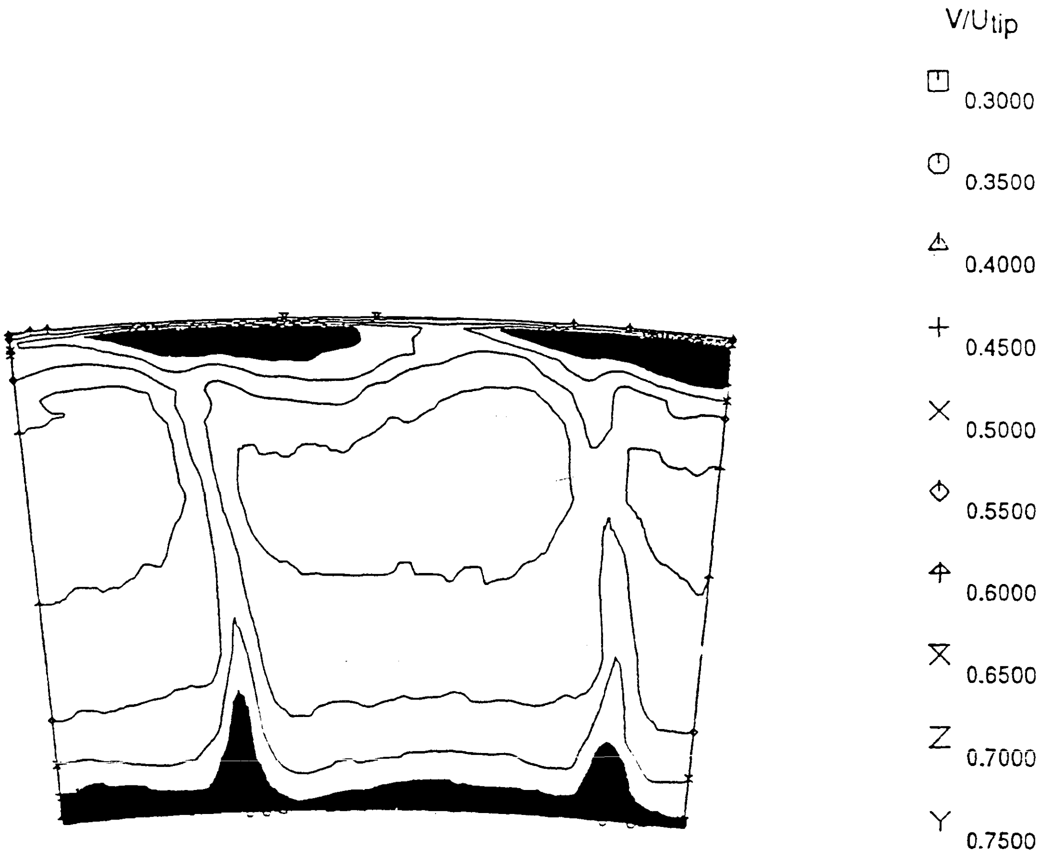

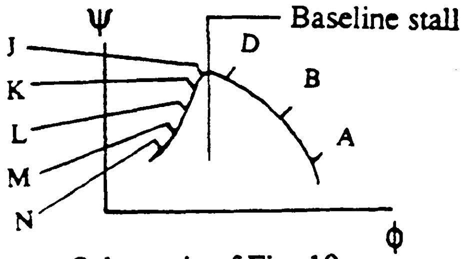

Schematic of Fig. 10

Figure 18: Through flow at rotor 1 exit in the relative frame. This is at a yaw of 55 ° from axial. Roughly 1.5 rotor pitches are displayed. Rotor blade wakes are visible. Operating point B of figure 10. Shaded region is low through flow region of v/Utip < .45

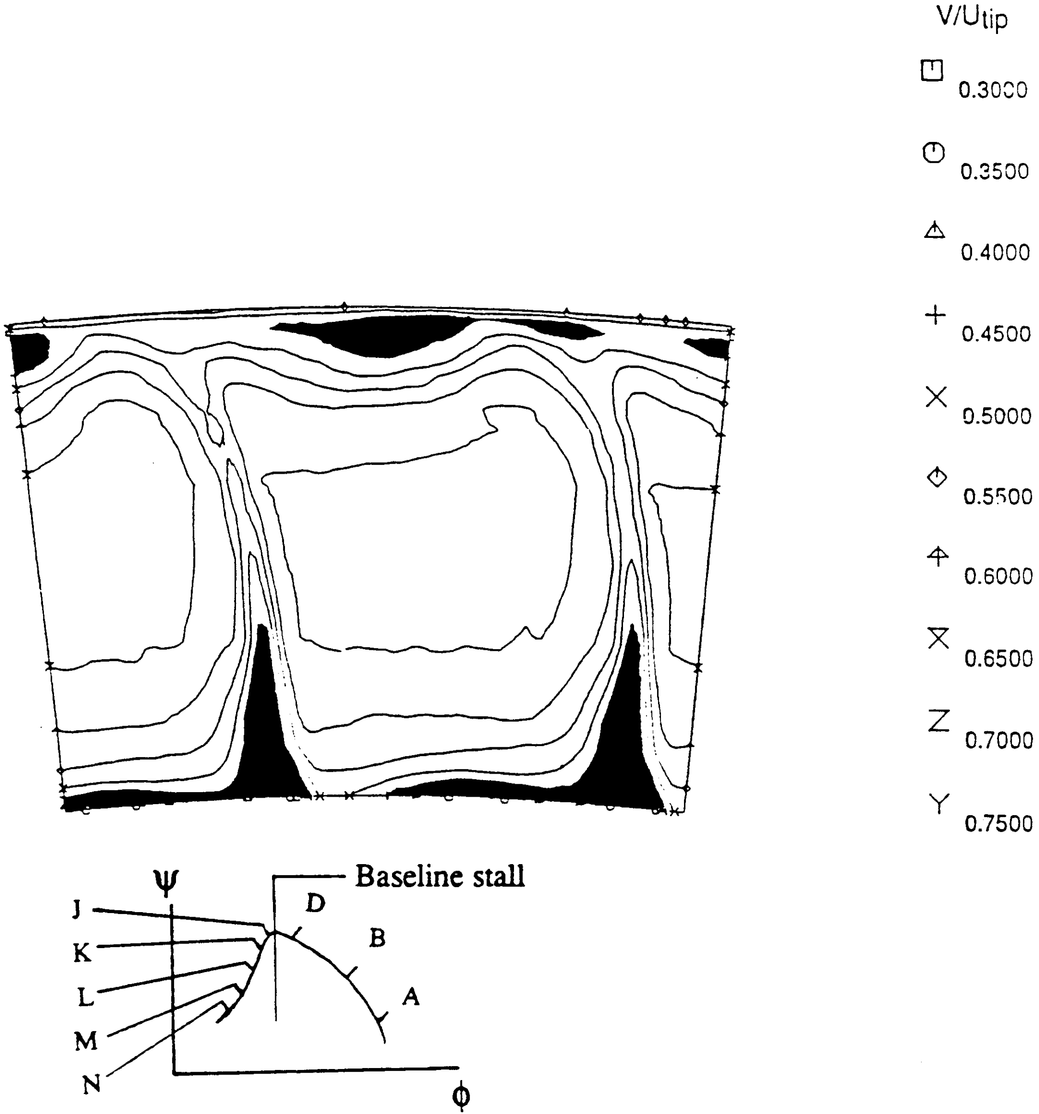

Schematic of Fig. 10

Figure 19: Through flow at rotor 1 exit in the relative frame. This is at a yaw of 55 ° from axial. Roughly 1.5 rotor pitches are displayed. Rotor blade wakes are visible. Operating point D of figure 10, baseline build near stall. Shaded region is low through flow region of v/Utip < .45

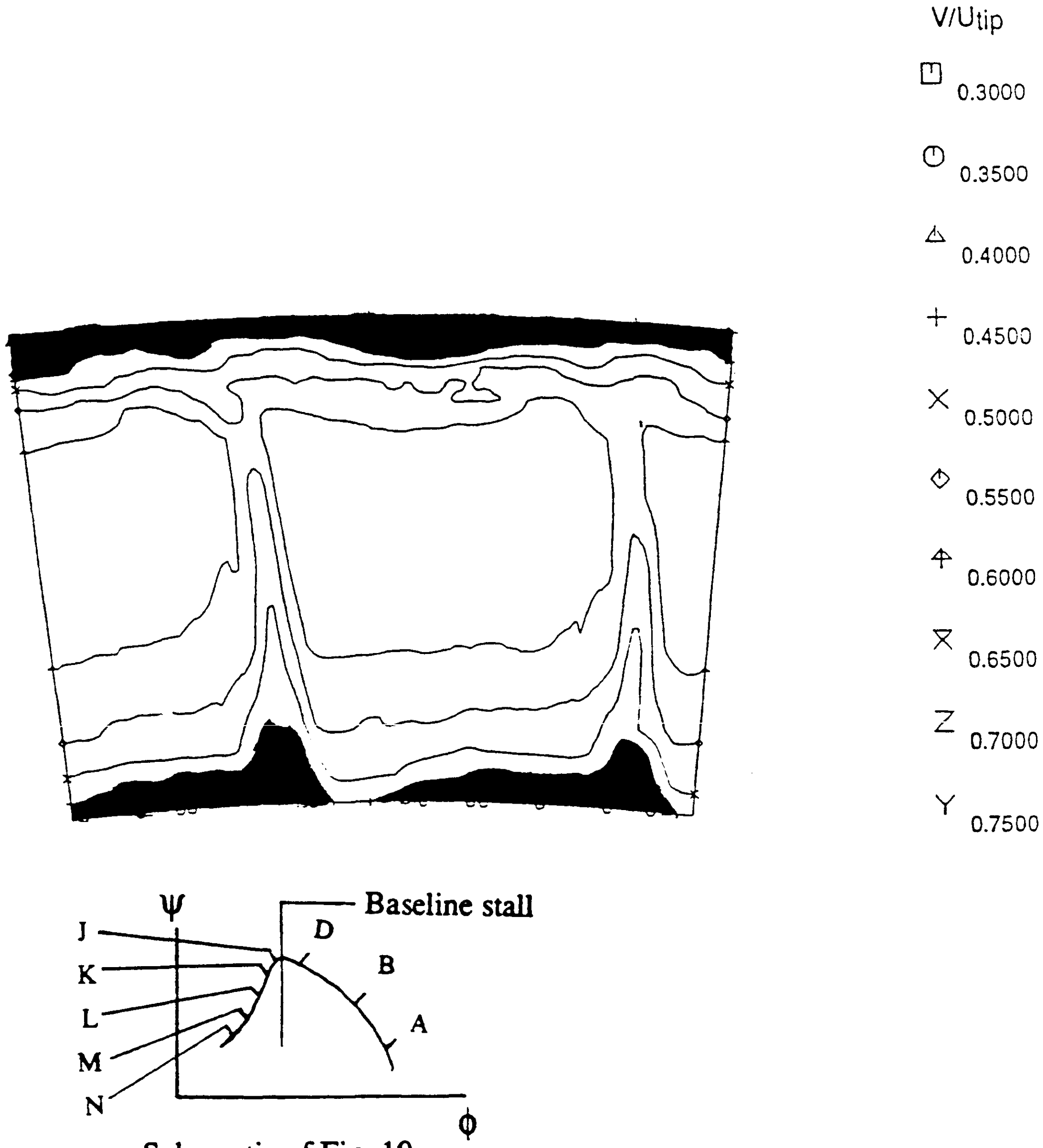

Schematic of Fig. 10

Figure 20: Through flow at rotor 1 exit in the relative frame. This is at a yaw of 55 ° from axial. Roughly 1.5 rotor pitches are displayed. Operating point K of figure 10, mismatch build in the extended operating region. Shaded region is low through flow region of v/Utip < .45

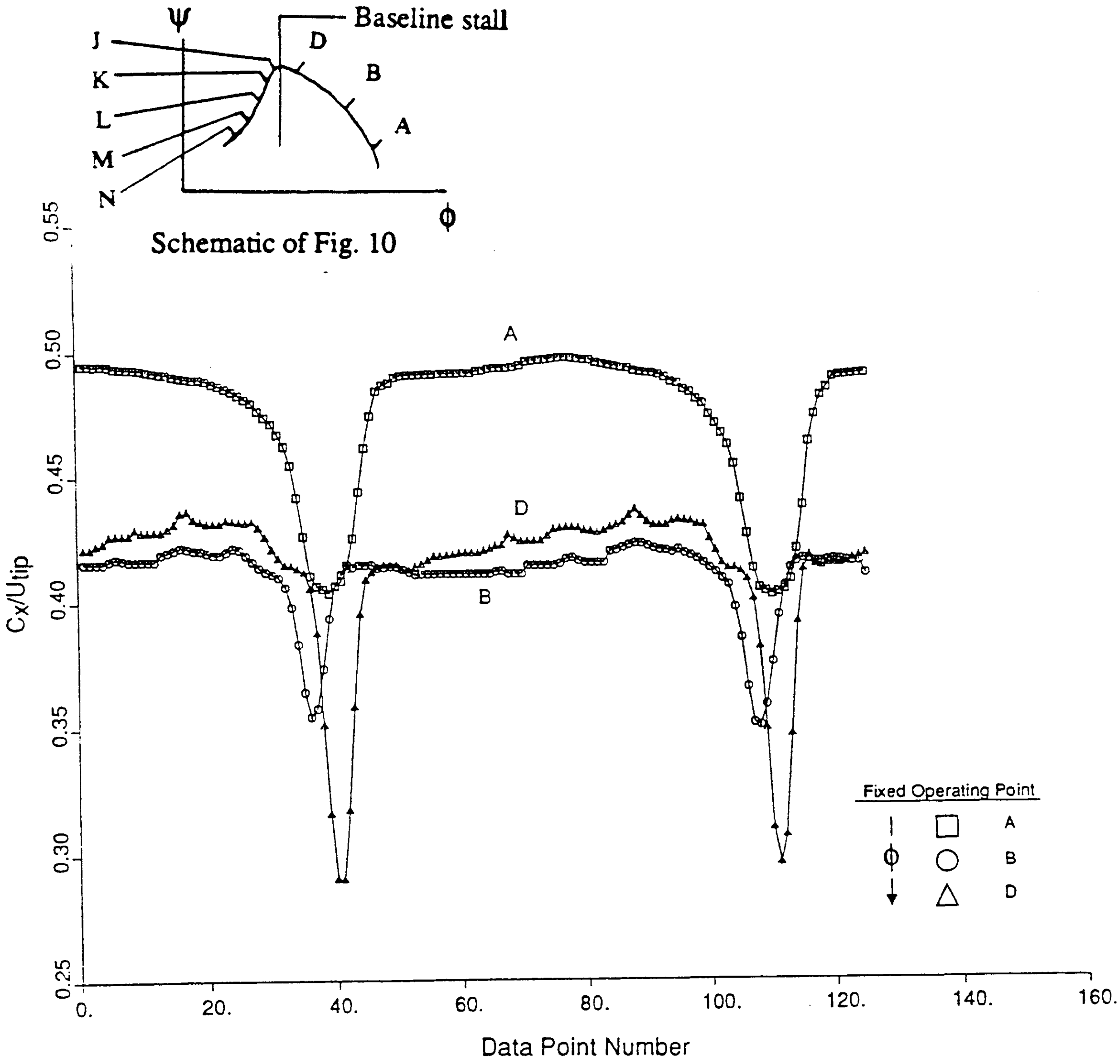

Figure 21: Circumferential profiles of axial velocity at midspan of rotor exit for the baseline build. Roughly 1.5 rotor pitches are displayed. Operating points correspond to those labeled in figure 10.

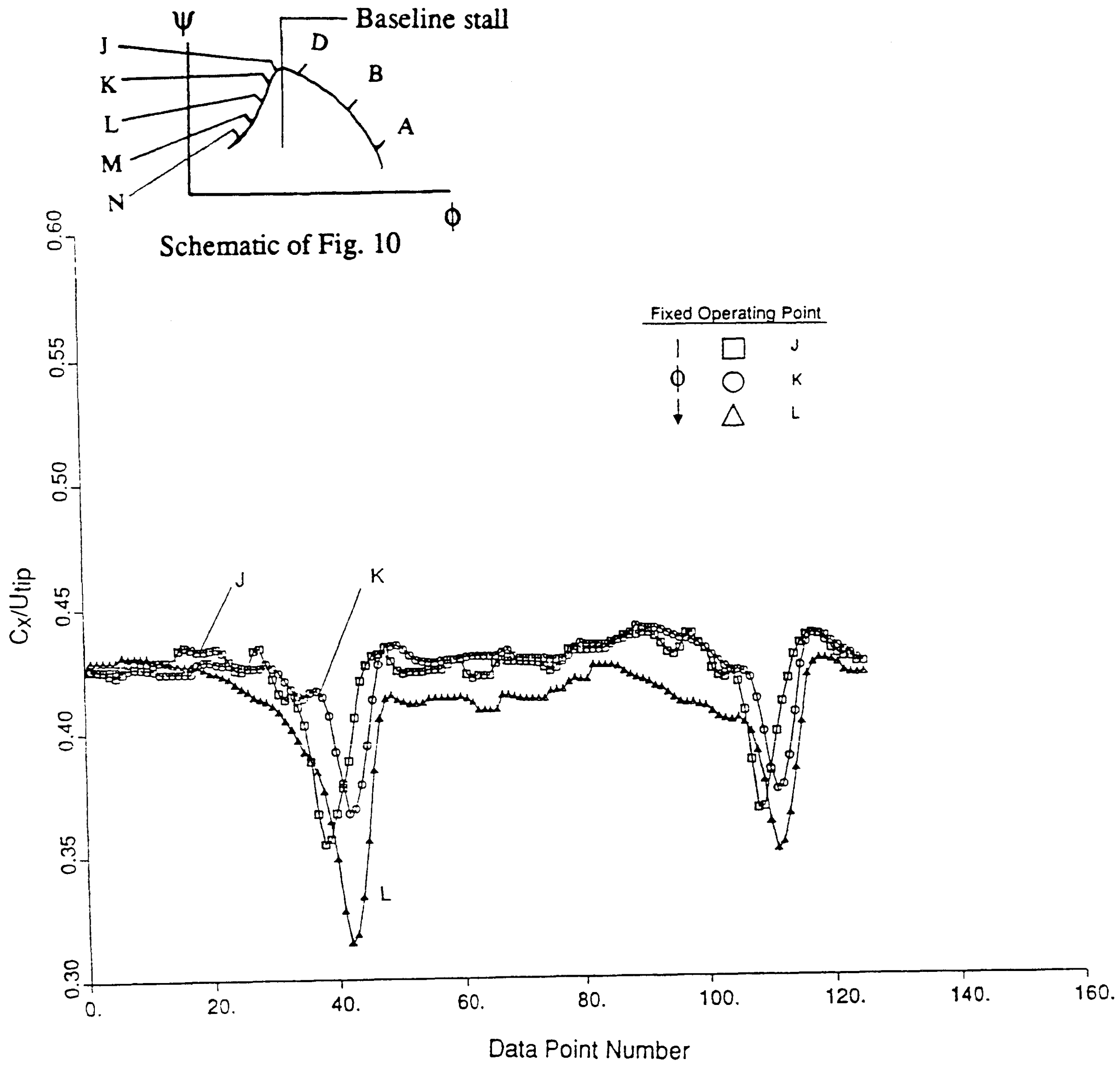

Figure 22: Circumferential profiles of axial velocity at midspan of rotor exit for the mismatch build. Roughly 1.5 rotor pitches are displayed. Operating points correspond to those labeled in figure 10.

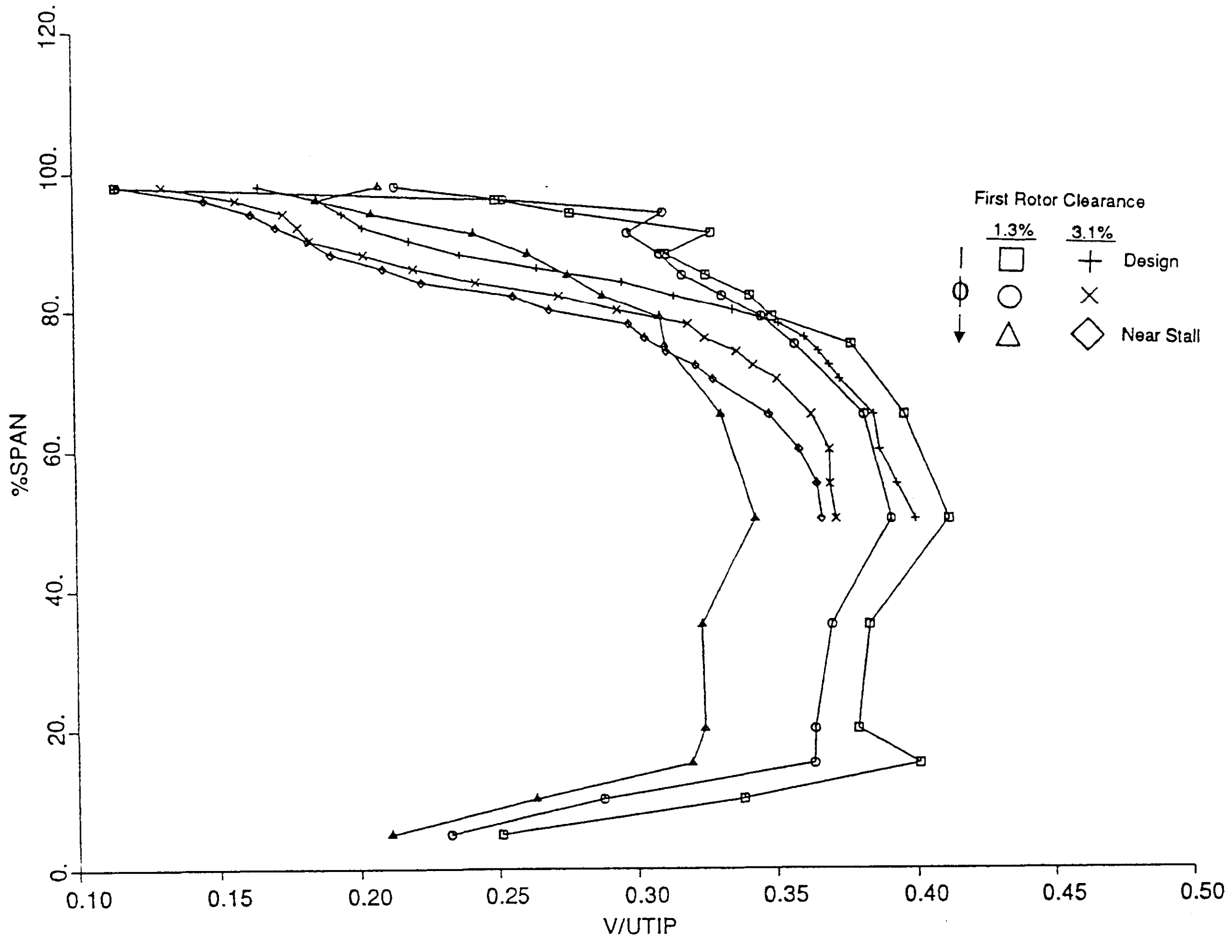

Figure 23: Radial profiles of pitchwise averaged axial velocity at rotor inlet. Both the baseline and larger first stage tip clearance builds are shown.

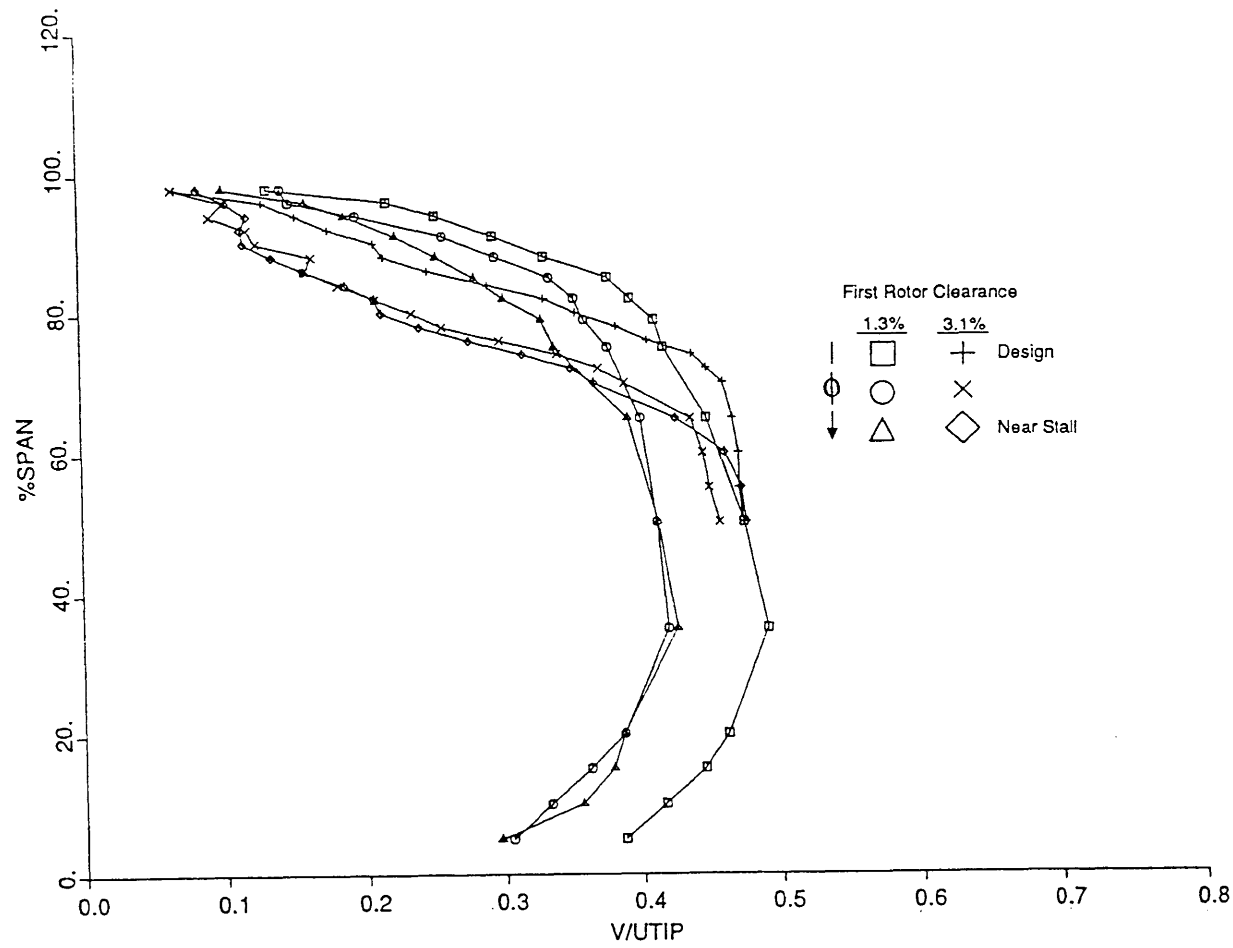

Figure 24: Radial profiles of pitchwise averaged axial velocity at rotor exit. Both the baseline and larger first stage tip clearance builds are shown.

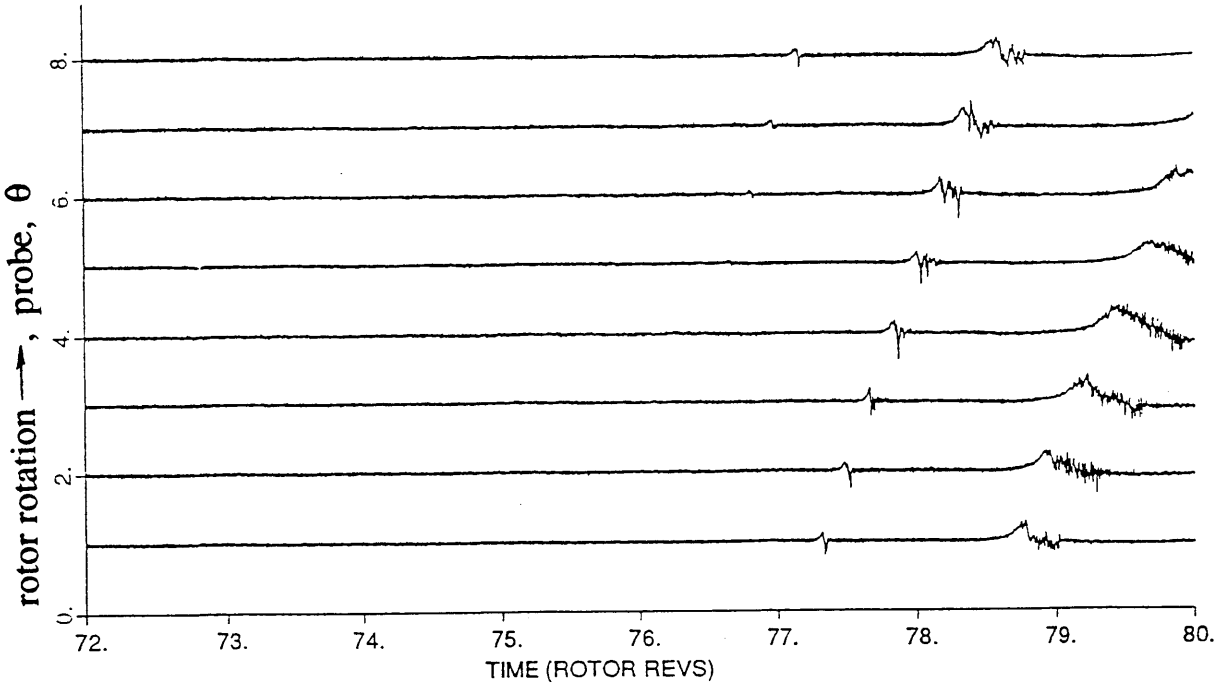

Figure 25: Pressure at rotor inlet vs. time as the compressor is throttled down into stall. 8 equally circumferentially spaced casing transducers, normalized data, baseline build. The probe numbers of the ordinate locate the zero level for each probe. Probe numbers increase in the direction of rotor rotation and increasing theta.

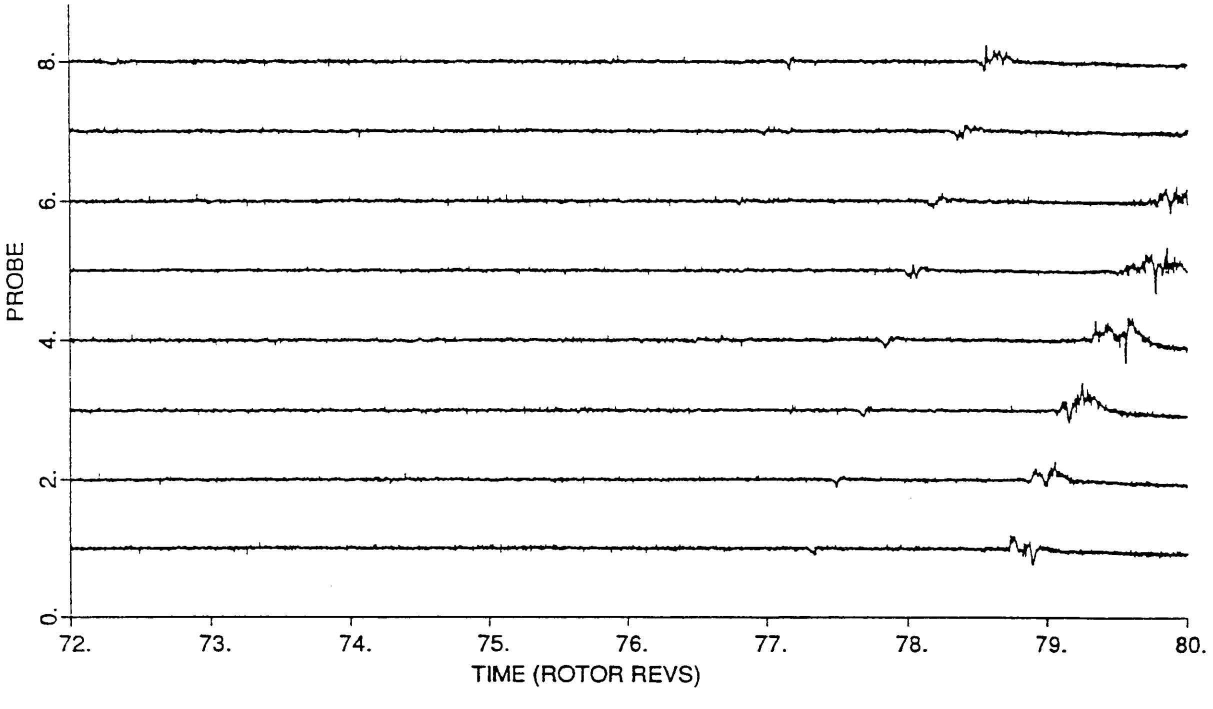

Figure 25b: Pressure at rotor exit vs. time as the compressor is throttled down into stall. 8 equally circumferentially spaced casing transducers, normalized data, baseline build. This is for a stall event similar to that of figure 25.

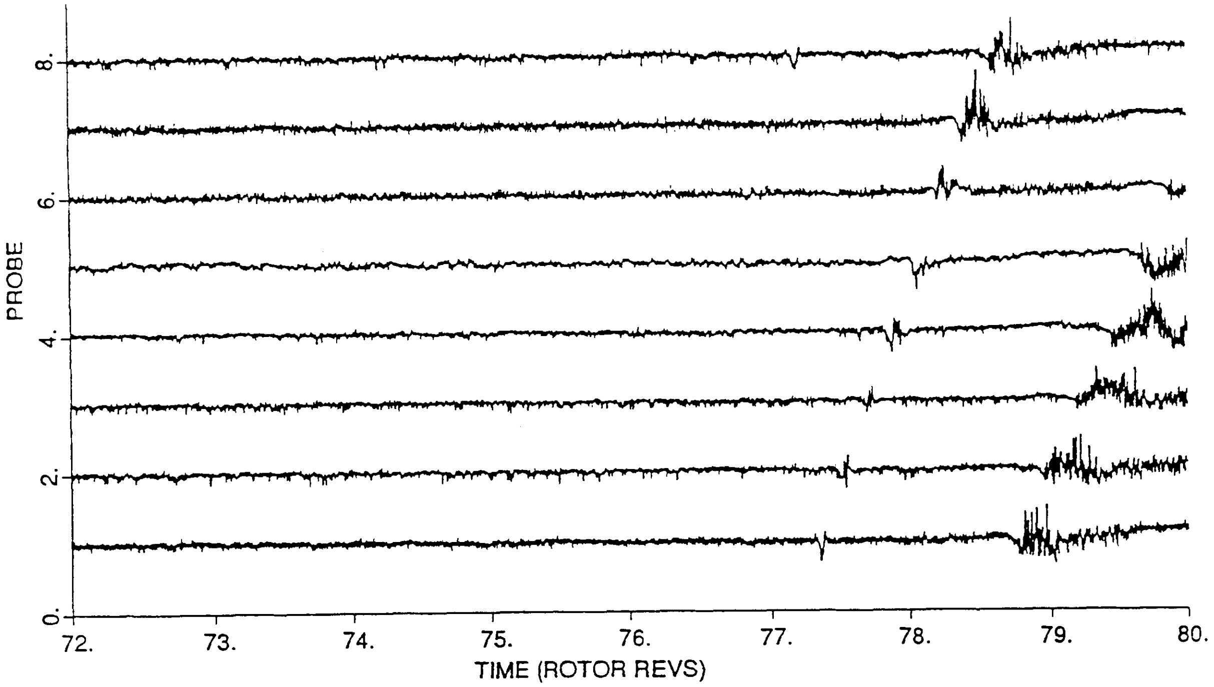

Figure 26: Velocity at rotor inlet vs. time as the compressor is throttled down into stall. 8 equally circumferentially spaced hot wires at 20% immersion, normalized data for the same case as figure 25, baseline build.

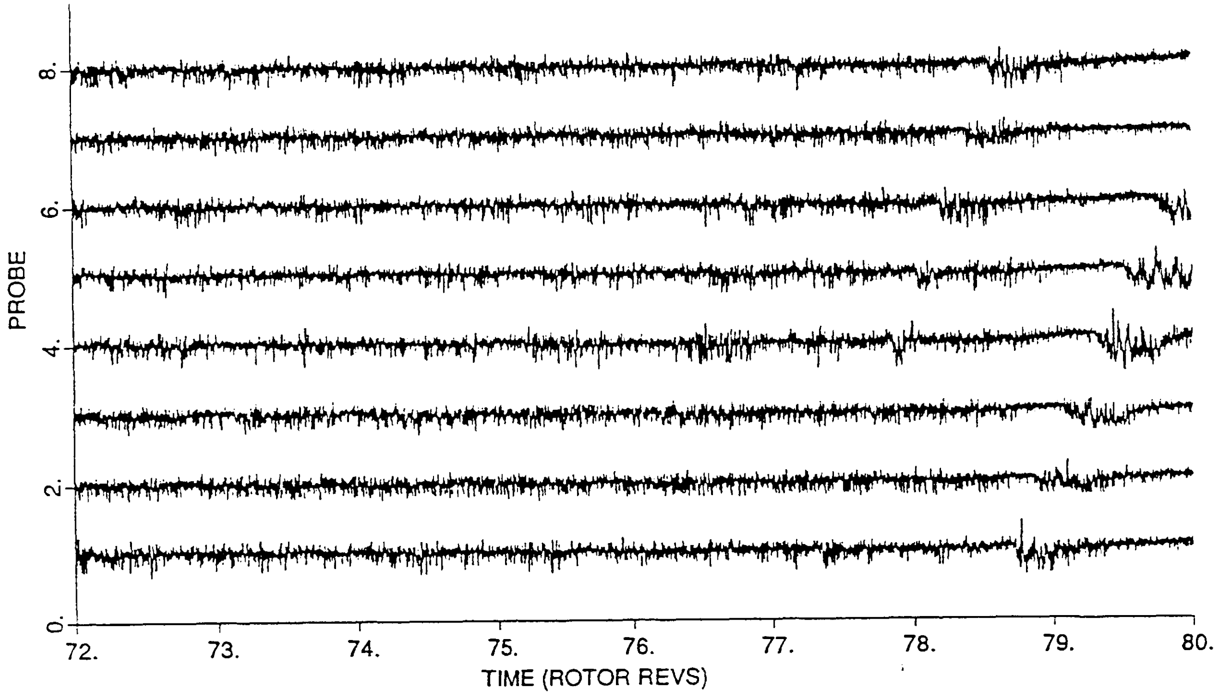

Figure 26b: Velocity at rotor exit vs. time as the compressor is throttled down into stall. 8 equally circumferentially spaced hot wires at 20% immersion, normalized data for the same case as figure 25b, baseline build.

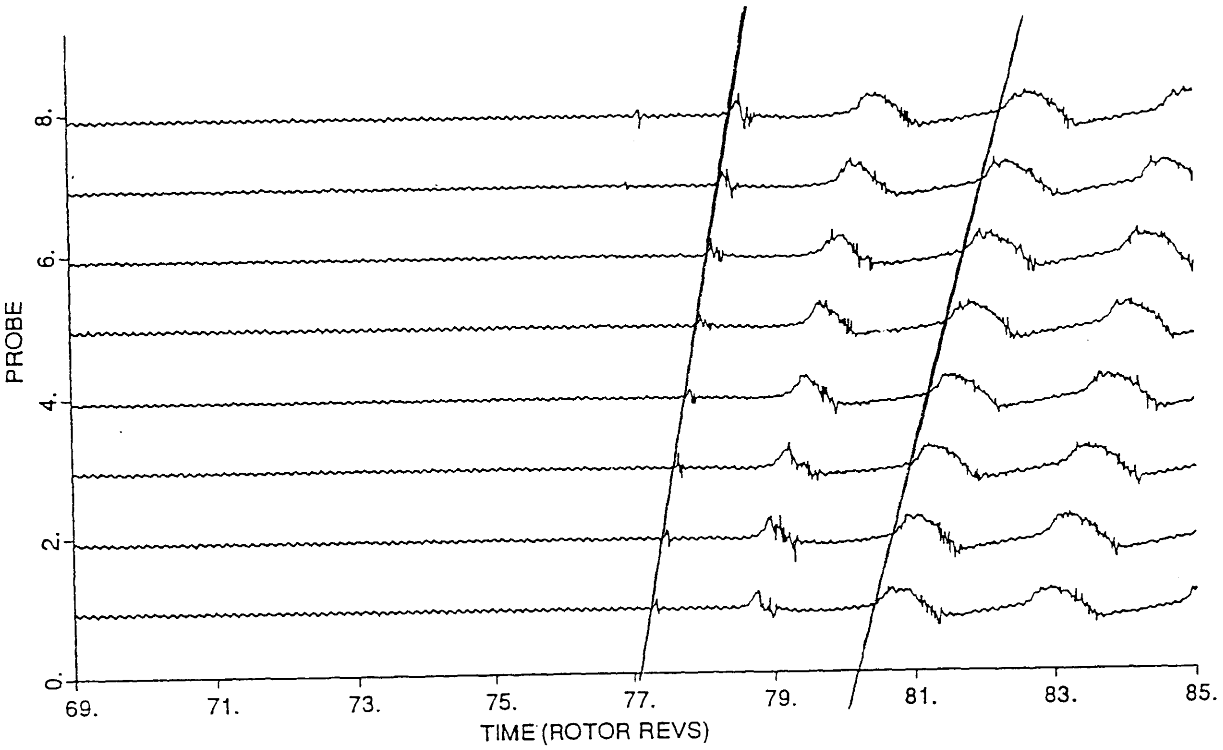

Figure 27: Raw data from figure 25. Pressure at rotor inlet vs. time as the compressor is throttled down into stall. 8 equally circumferentially spaced casing transducers. Guidelines have been drawn to display the change in circumferential propagation speed of the disturbance.

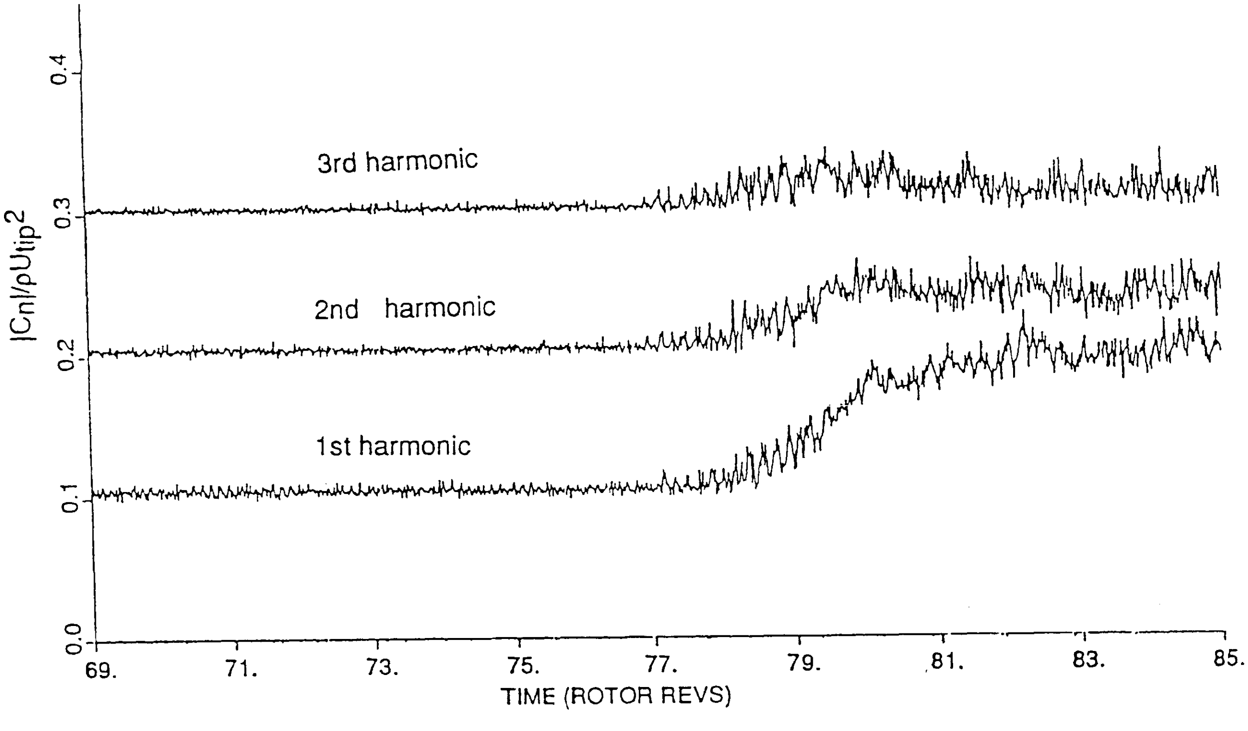

Figure 28: Magnitudes of spatial Fourier analysis of figure 27, pressure at rotor inlet, at each time. The zeros for the various harmonics are offset for clarity. No disturbances are visible prior to t~77, when the pip is first seen, (see figs. 25,26,27).

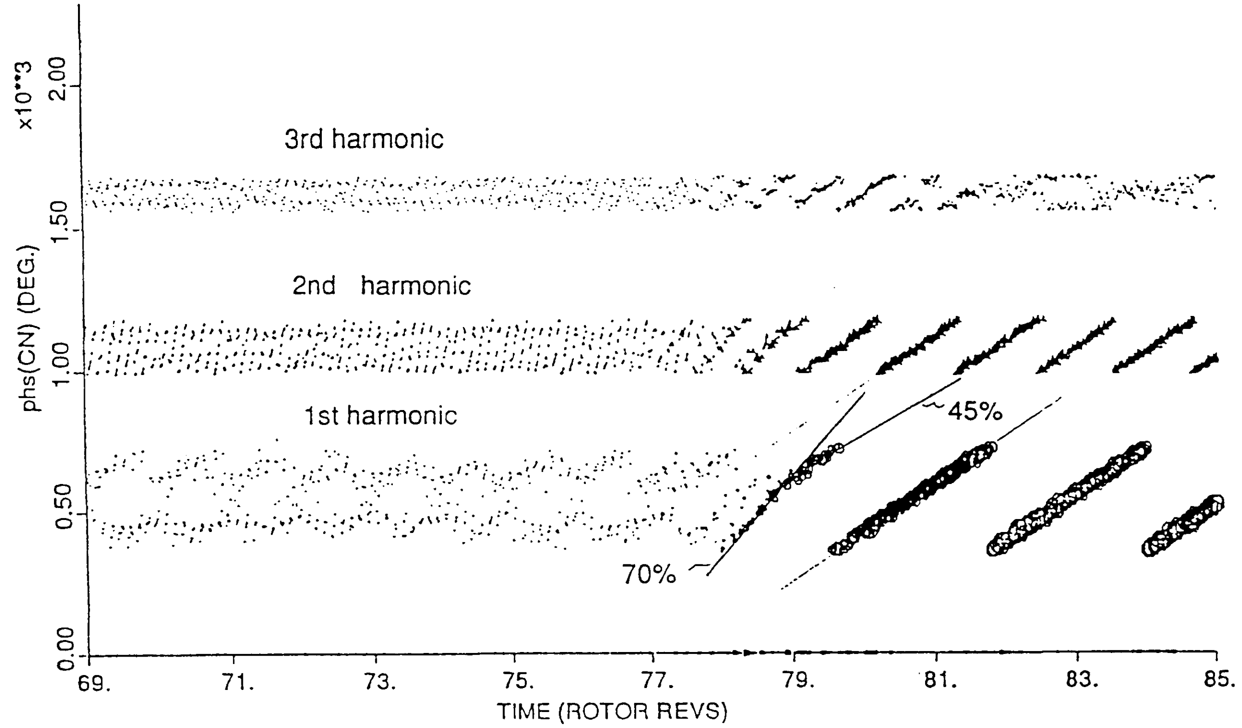

Figure 29: Phase of spatial Fourier analysis of figure 27. Symbol size is scaled by the magnitude of each harmonic, figure 28. The zeros for the various harmonics are offset for clarity. Guidelines show the change in circumferential propagation speed of the disturbance from the pip's 70% speed to the stall cell's 45% speed. Once per revolution signal seen in first harmonic is attributed to a rotor asymmetry.

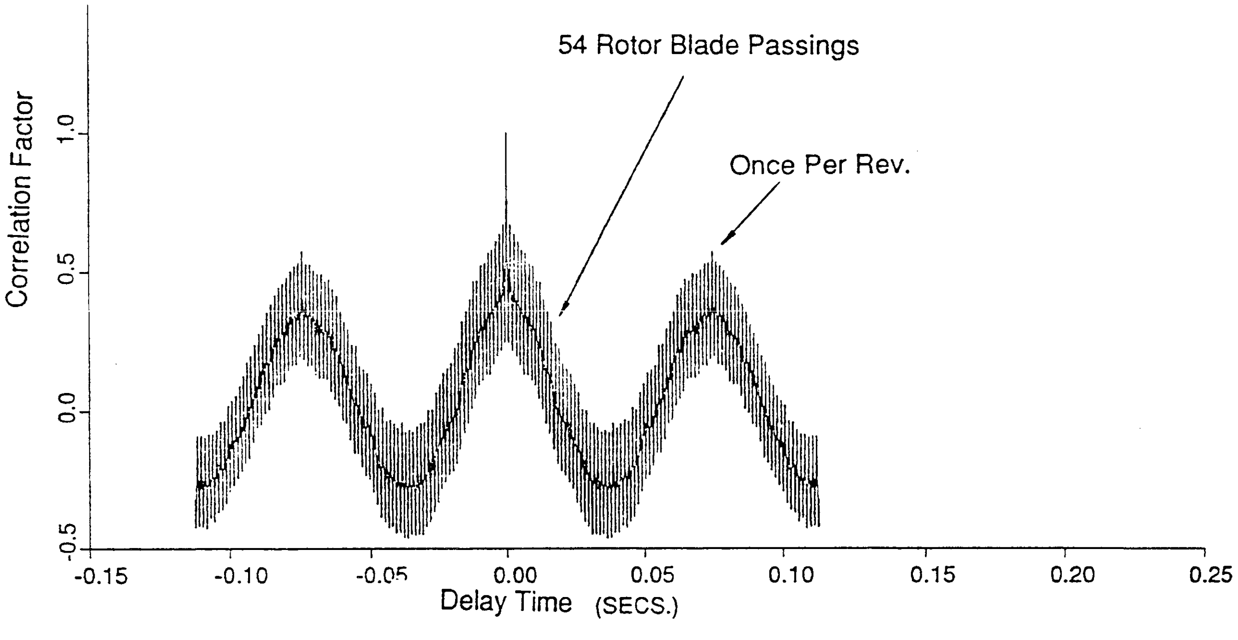

Figure 30: Autocorrelation of first pressure transducer from figure 25, taken over the time period 65 <t< 75. Clearly seen are the once per revolution signal from the first harmonic of figure 29 and the 54 overtones of rotor blade passing. No evidence of any other propagating disturbances.

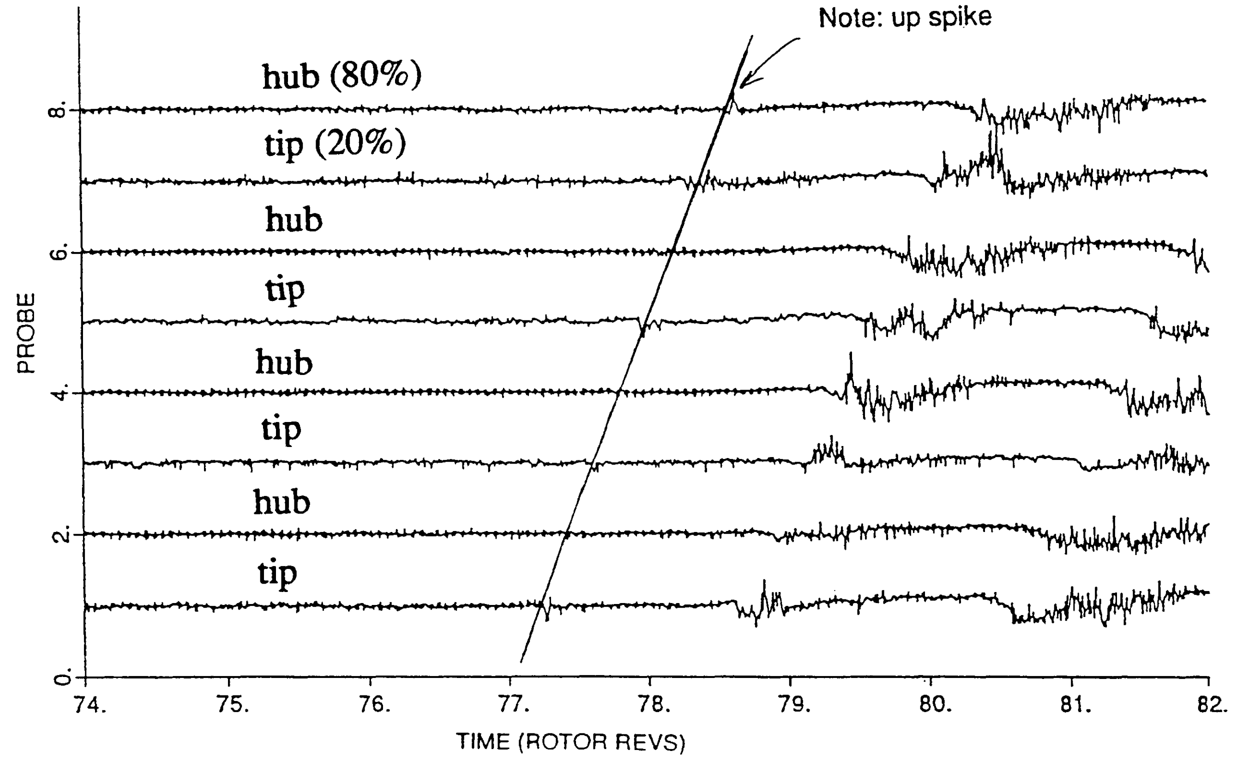

Figure 31: Alternating hub/tip velocity at rotor inlet vs. time as the compressor is throttled down into stall. 8 equally circumferentially spaced hot wires, normalized data, baseline build. Note disturbance is first visible as a deficit in the tip region at t~77.

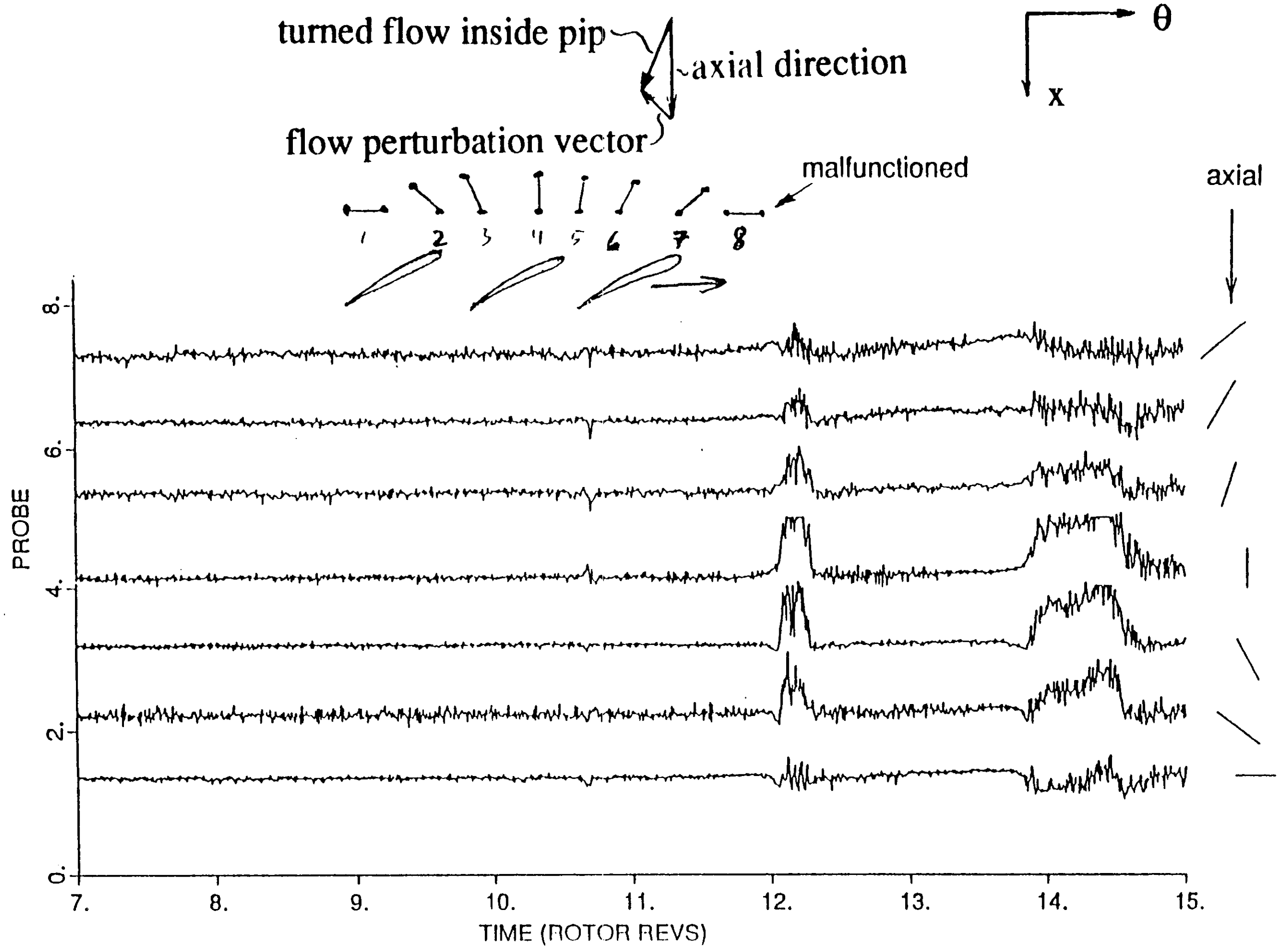

Figure 32: Velocity from hot wires at different inclinations. Rotor inlet, 20% immersion, 8 equally circumferentially spaced hot wires over a 3 pitch region as the compressor is stalled, baseline build. The sketched flow turning due to the proposed flow perturbation is consistent with the observed velocity deficits and increments on the various wires.

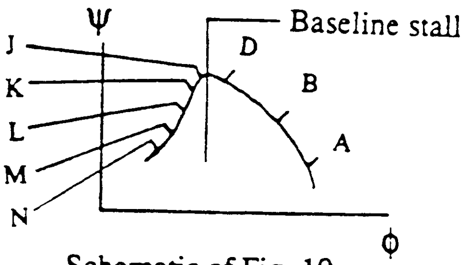

Schematic of Fig. 10

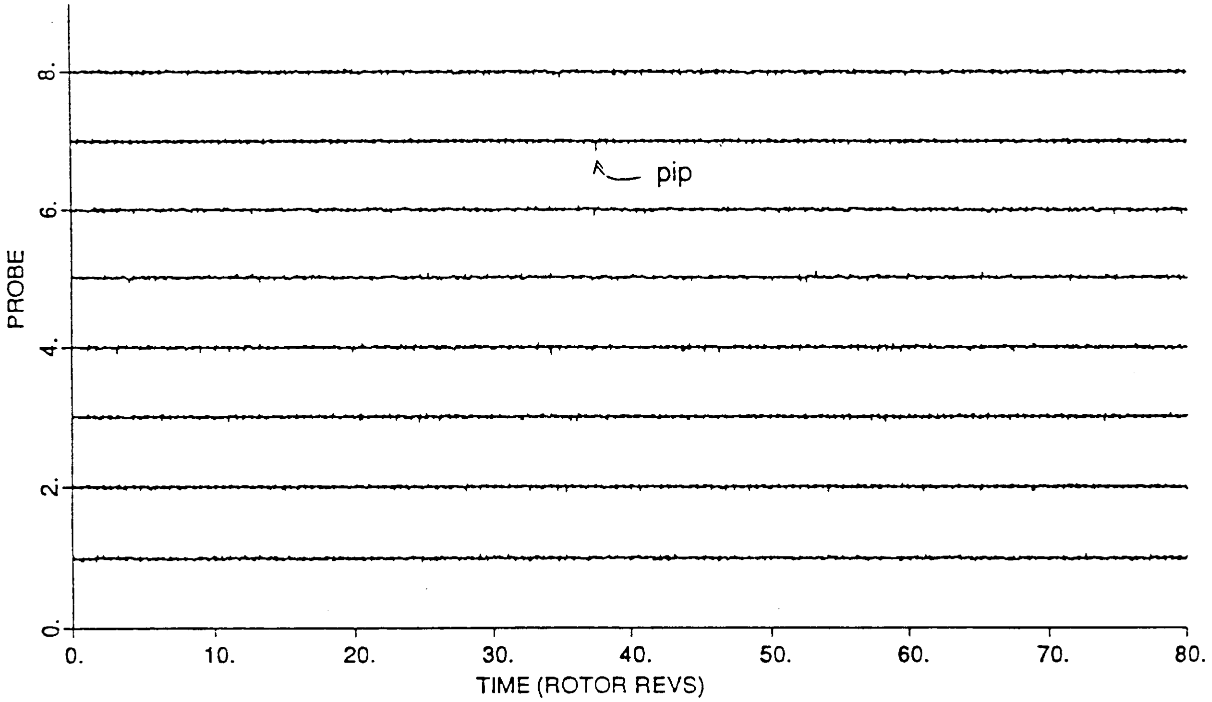

Figure 33: Velocity at rotor inlet vs. time for fixed operating point J, see fig. 10. 8 equally circumferentially spaced hot wires, normalized data, 20% immersion, mismatch build, baseline stall point. Short lived pips appear and disappear sporadically. An example of this is seen on wire 7 at t=38.

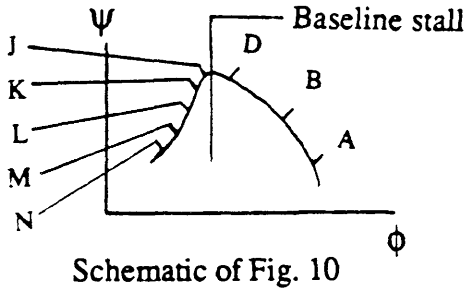

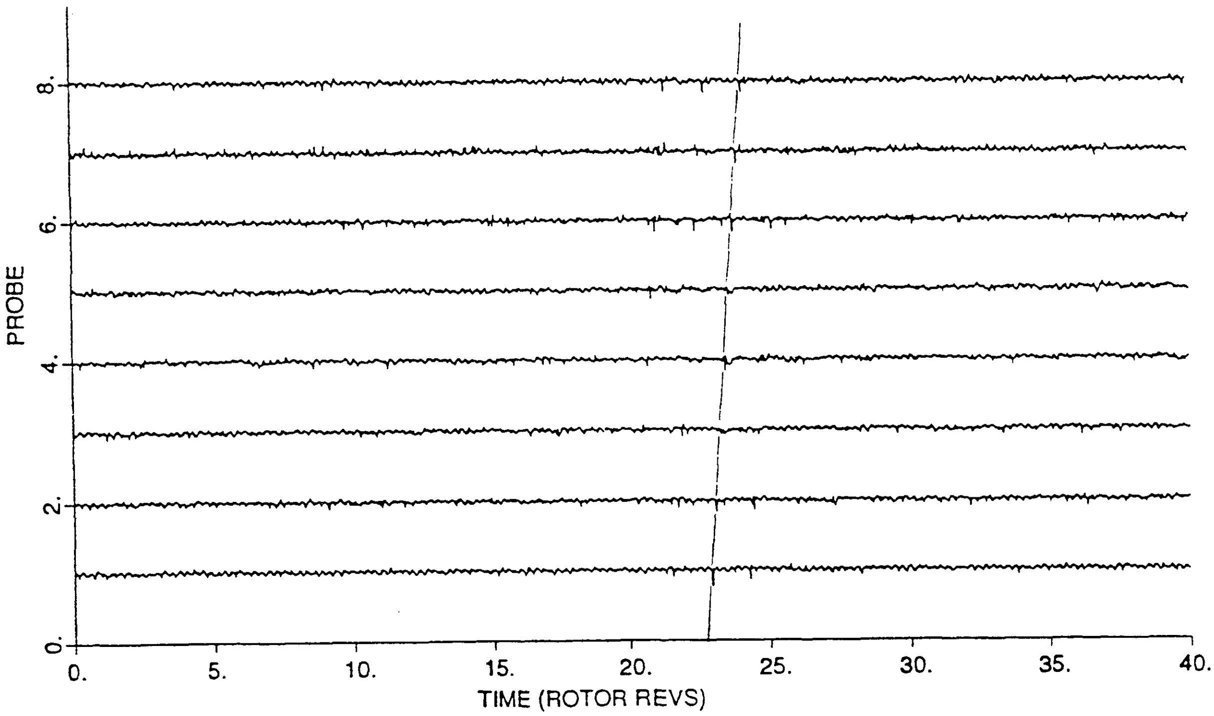

Figure 34: Velocity at rotor inlet vs. time for fixed operating point J, see fig. 10. 8 equally circumferentially spaced hot wires, normalized data, 20% immersion, mismatch build, baseline stall point. A guideline has been included to track a particular pip.

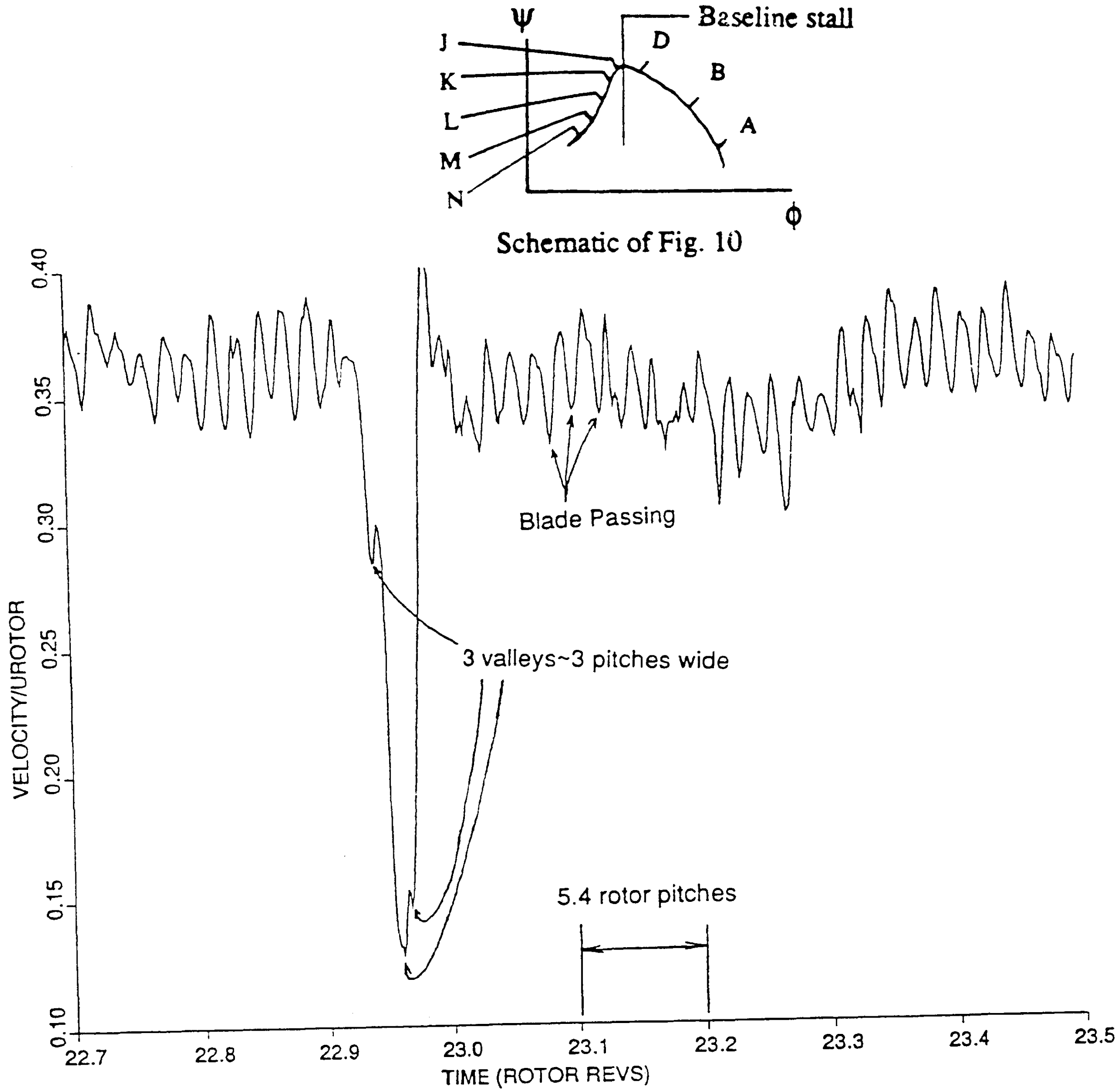

Figure 35: Velocity at rotor inlet vs. time for fixed operating point J, see fig. 10. 20% immersion, mismatch build, baseline stall point. This is an expanded view of probe #2 from figure 34. The pip is roughly 3 pitches wide.

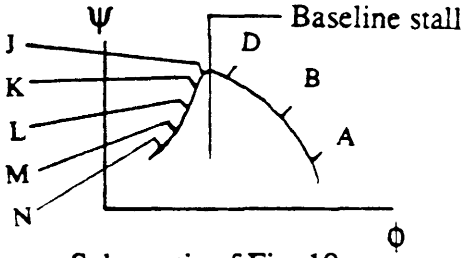

Schematic of Fig. 10

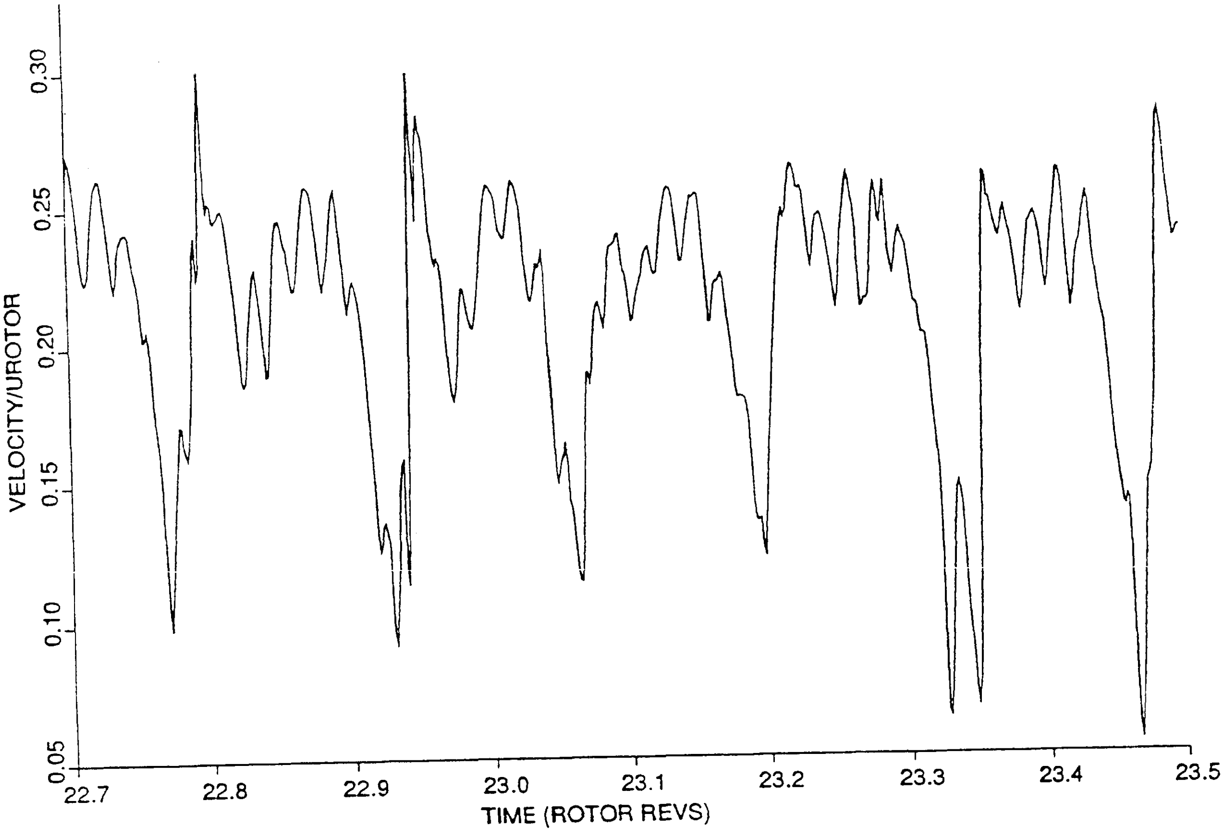

Figure 35b: Velocity at rotor inlet vs. time for fixed operating point M, see fig. 10. 20% immersion, mismatch build. Note that there are now more pips, and they appear fuller than in figure 35, operatingpoint J.

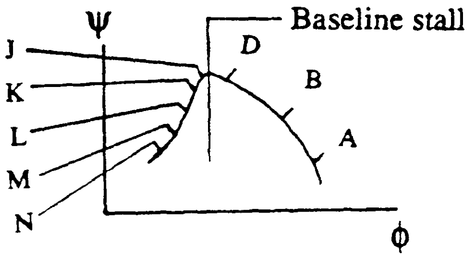

Schematic of Fig. 10

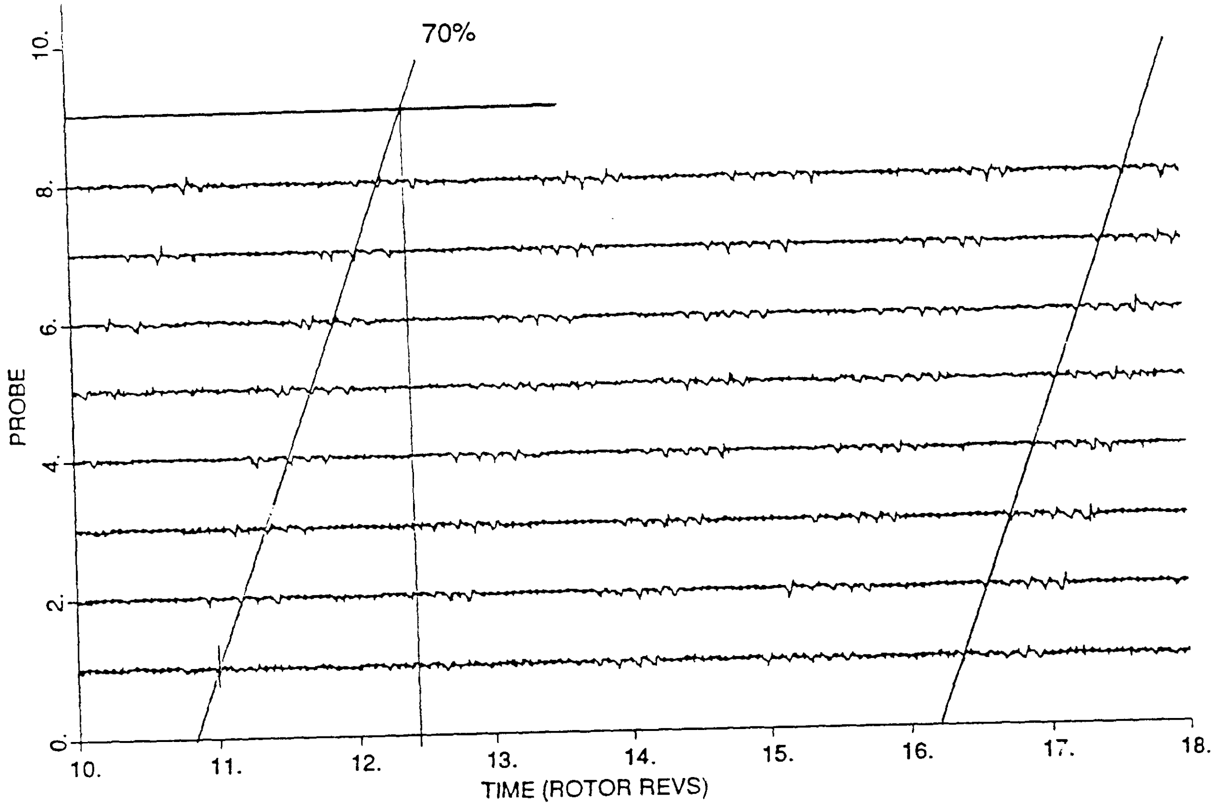

Figure 36: Velocity at rotor inlet vs. time for fixed operating point L, see fig. 10. 8 equally circumferentially spaced hot wires, normalized data, 20% immersion, mismatch build. Note that the disturbances, roughly 5 of them, travel at 70% speed and are not equally spaced about the annulus.

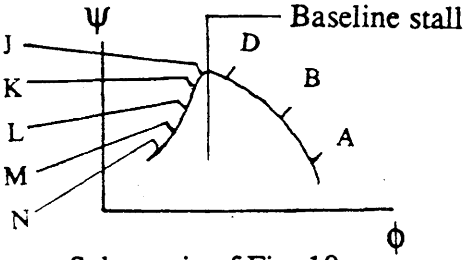

Schematic of Fig. 10

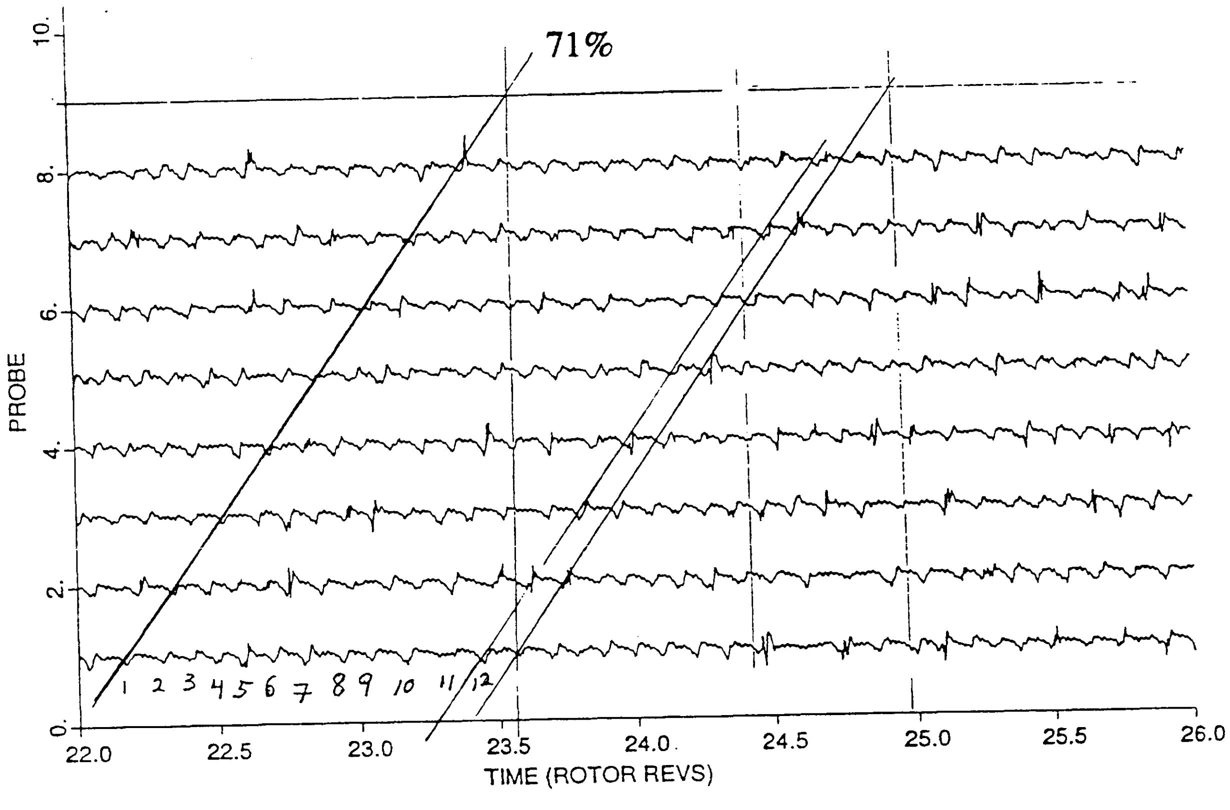

Figure 37: Velocity at rotor inlet vs. time for fixed operating point N, see fig. 10. 8 equally circumferentially spaced hot wires, normalized data, 20% immersion, mismatch build.
Note 12 pips/circumference travelling at roughly 70% speed causing a 9/rev signal.

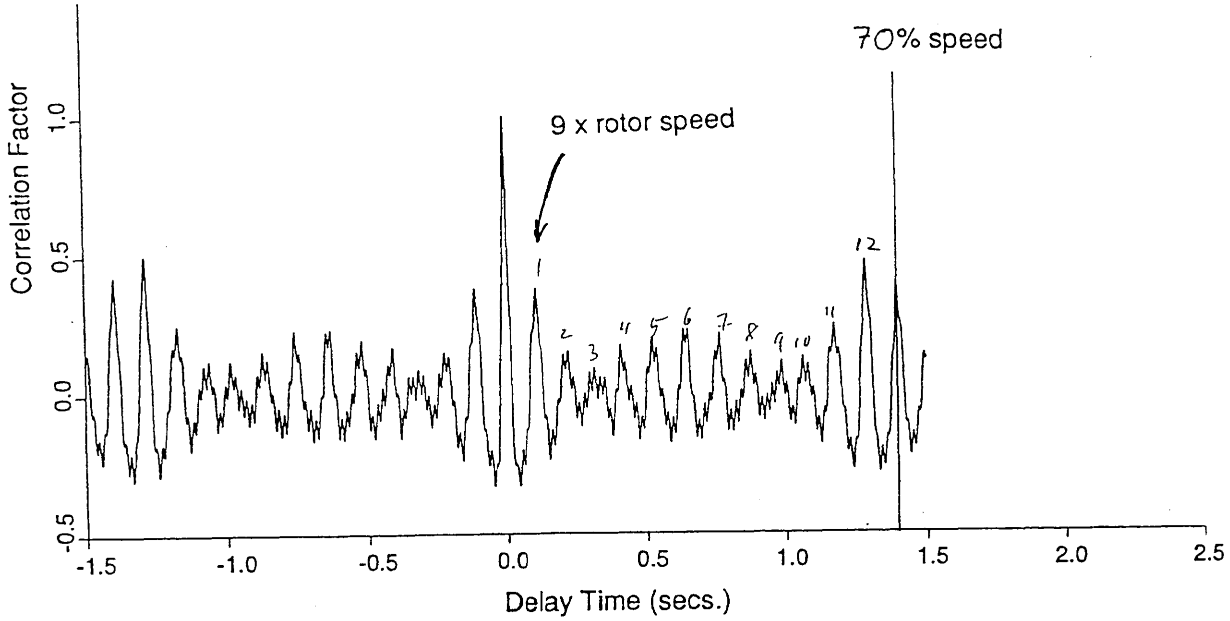

Figure 37b: Autocorrelation of velocity at rotor inlet vs. time for fixed operating point N, 20% immersion, mismatch build, see fig. 10. Specifically, probe #1 from figure 37 was used. Note the confirmation of 12 disturbances travelling at roughly 70% speed, giving rise to an apparent signal at 9 X rotor speed.

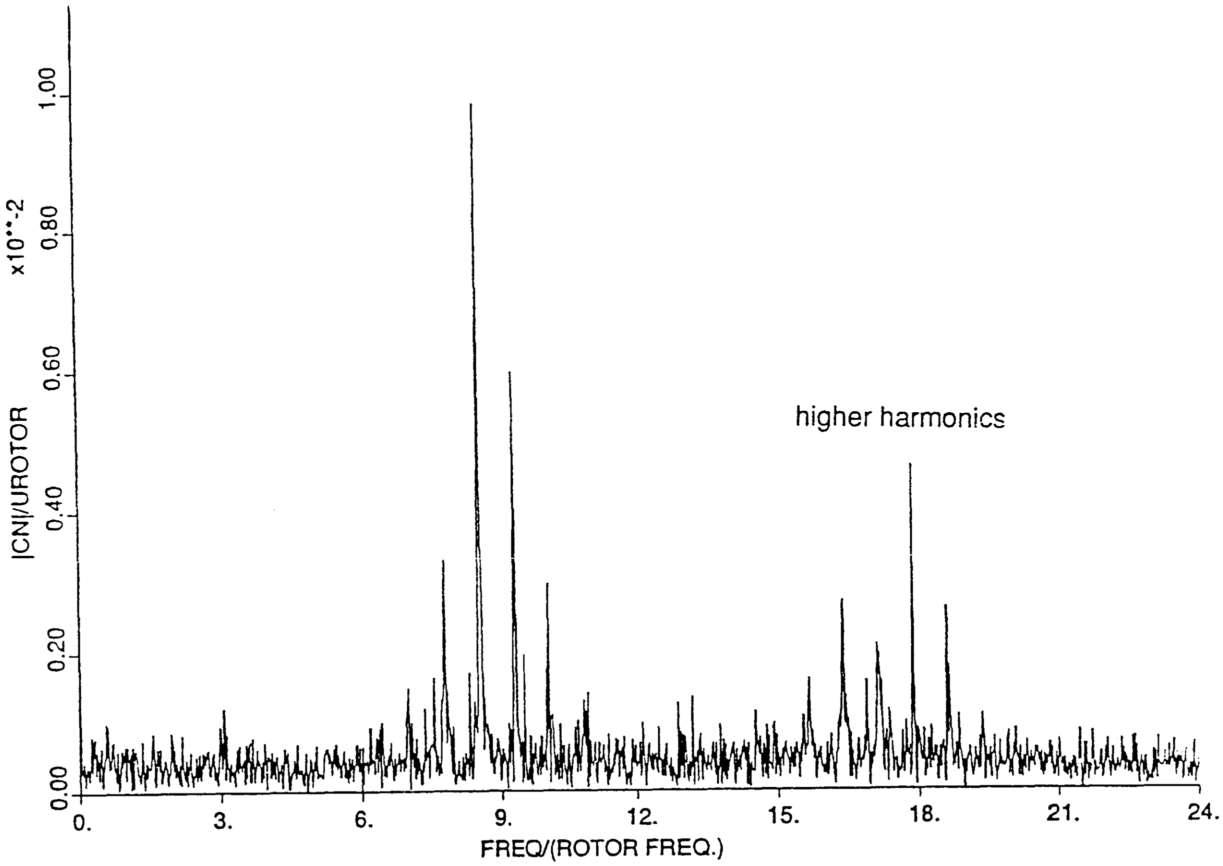

Figure 37c: Temporal FFT of velocity at rotor inlet vs. time for fixed operating point N, 20% immersion, mismatch build, see fig. 10. Specifically, probe #1 form figure 37 was used. The apparent signal at 9 X rotor speed is clearly visible.

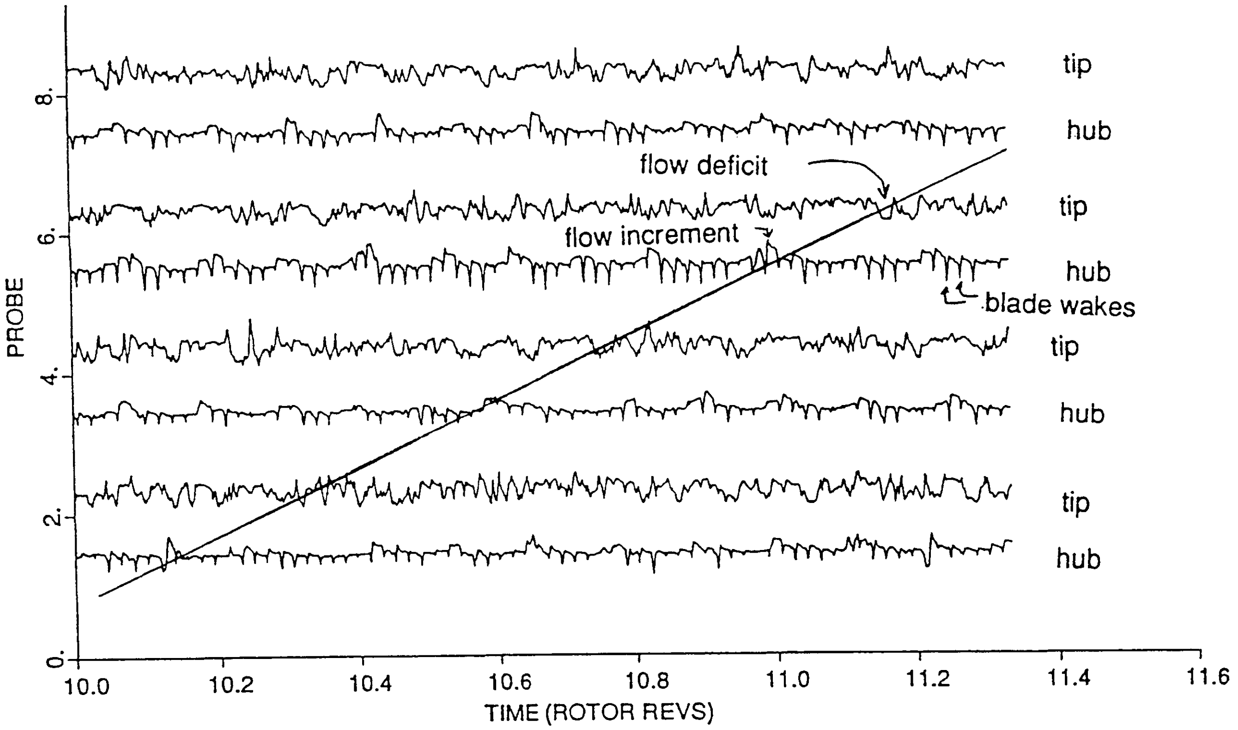

Figure 38: Alternating hub/tip hot wires at rotor exit vs. time as the mismatched compressor is throttled down into stall. 8 equally circumferentially spaced hot wires at 80%/20% immersion. Guideline show signal at 73% speed, based on crosscorrelation.

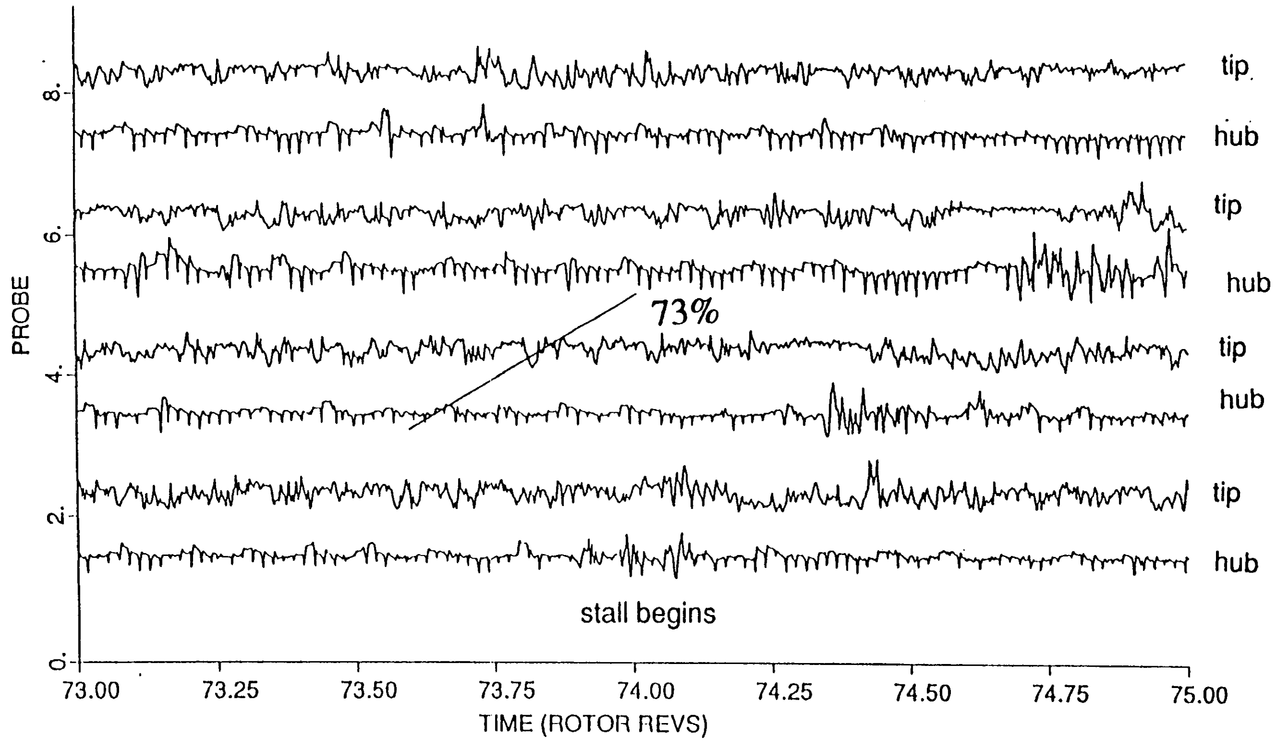

Figure 39: Alternating hub/tip hot wires at rotor exit vs. time as the mismatched compressor is throttled down into stall. 8 equally circumferentially spaced hot wires at 80%/20% immersion. Guideline shows signal at 73% speed, based on crosscorrelation. This is for the same event as figure 38, but later in time. Radial variation of disturbance continues until stall begins.

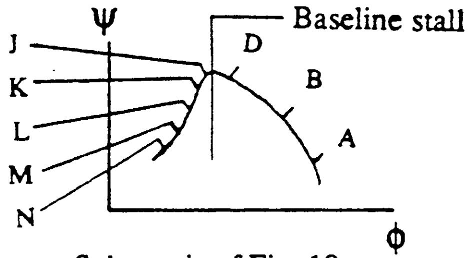

Schematic of Fig. 10

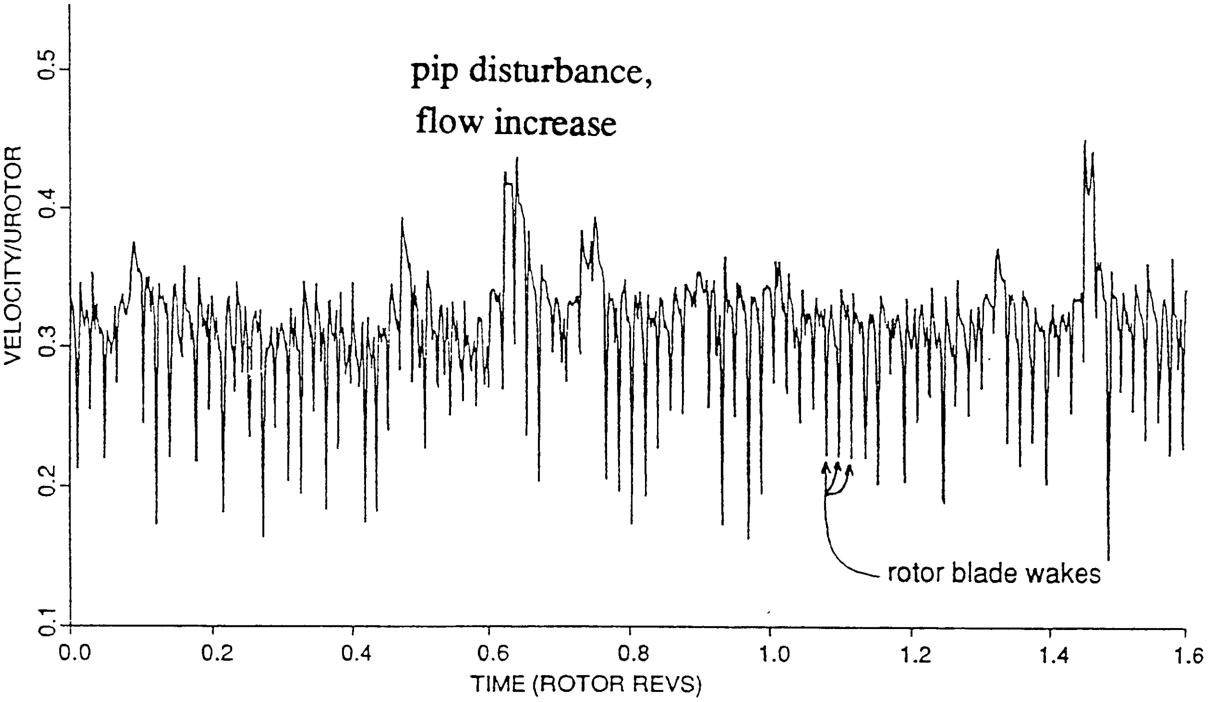

Figure 40: Velocity at 80% immersion for the mismatch build at rotor exit for fixed operating point K, see fig. 10. The disturbance appears as a flow increase on the order of a few blade pitches wide in the circumferential direction.

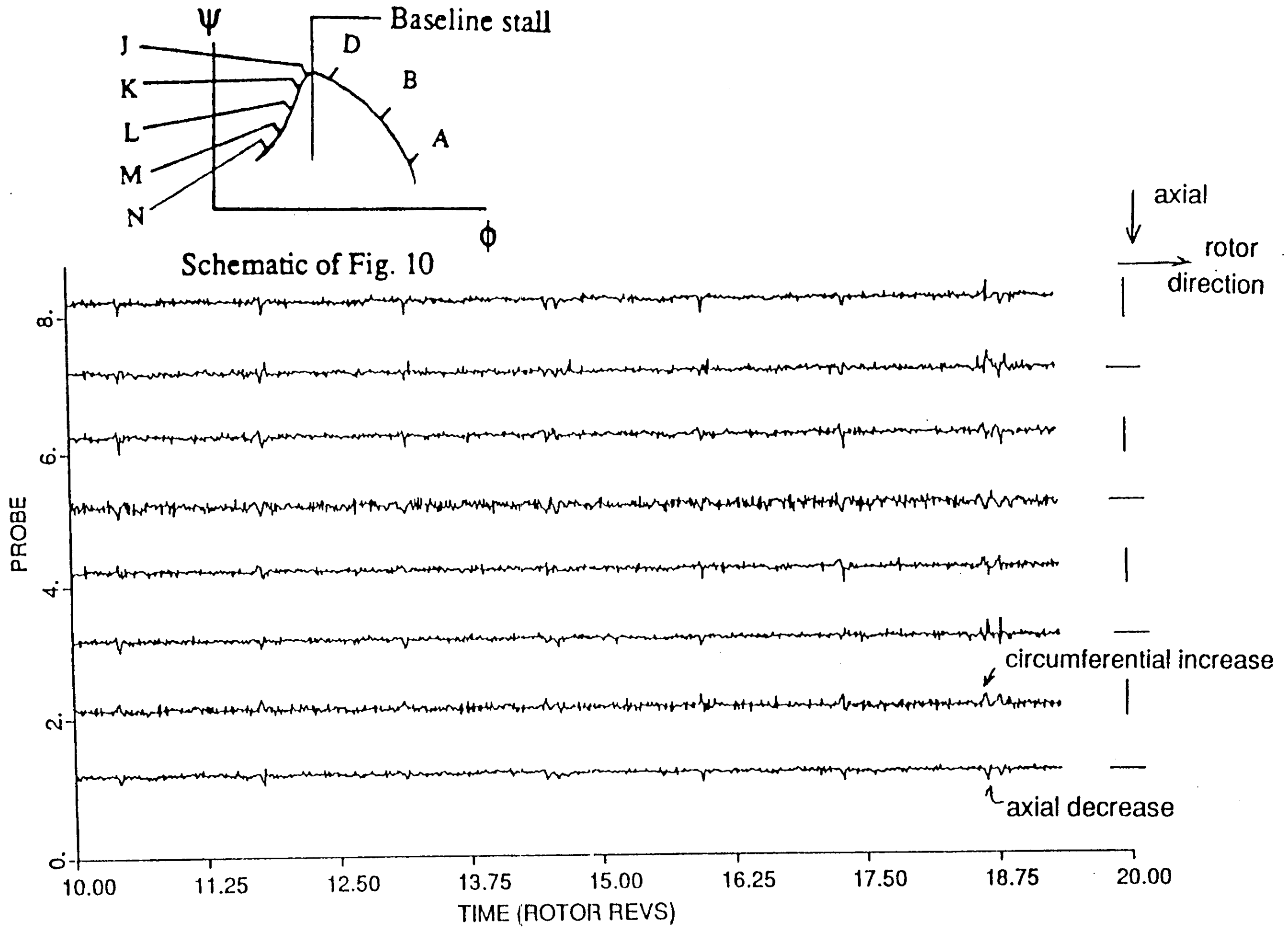

Figure 41: Velocity at 5% immersion for the mismatch build at rotor inlet for fixed operating point K, see fig. 10. The hot wires are packed over 3 pitches, and their orientation alternates as indicated. The pip appears as an axial decrease, and a circumferential increase.

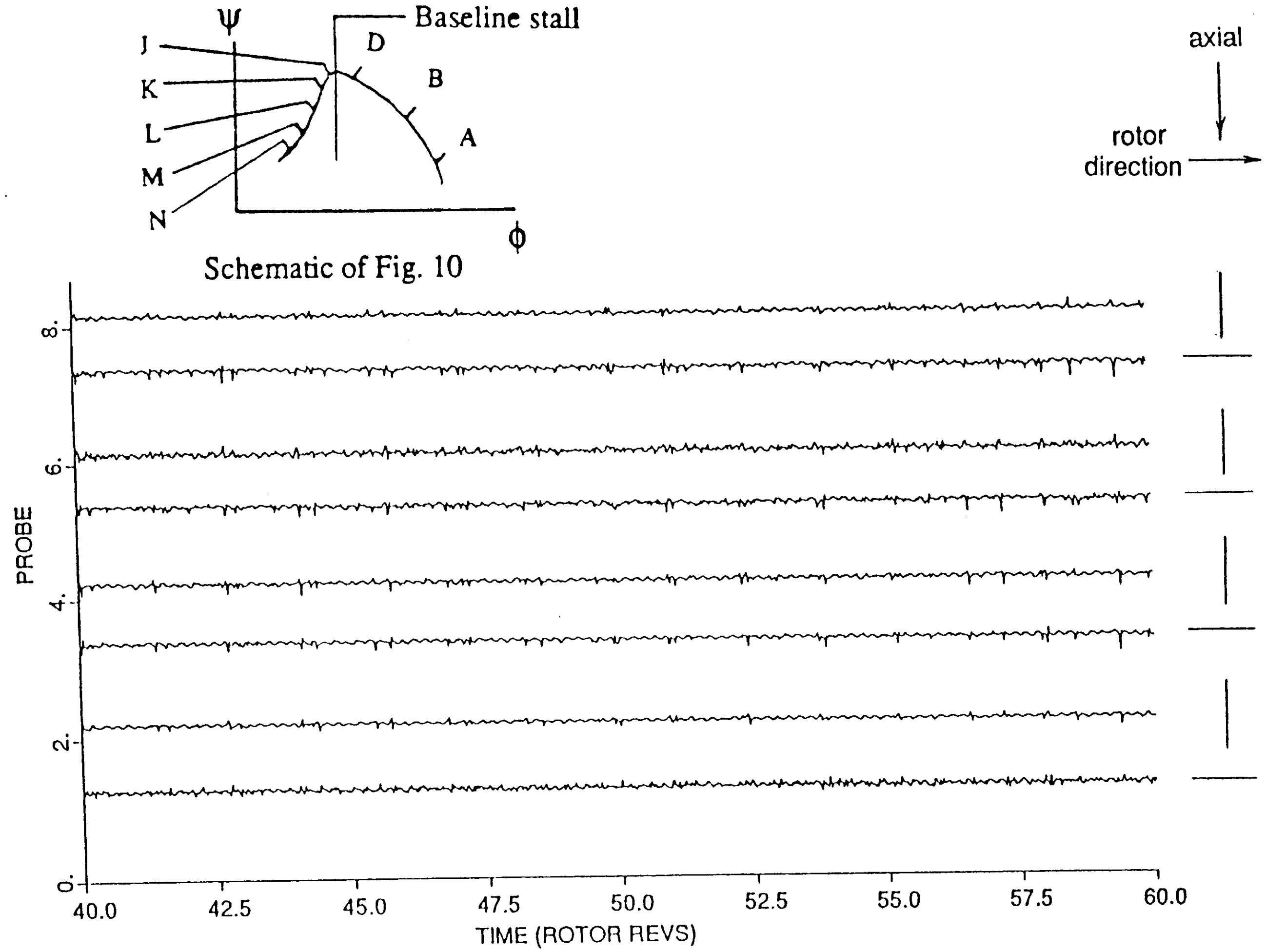

Figure 42: Velocity at 30% immersion for the mismatch build at rotor inlet for fixed operating point K, see fig. 10. The hot wires are packed over 3 pitches, and their orientation alternates as indicated. The disturbances are less visible than they were at 5% immersion, fig. 41.

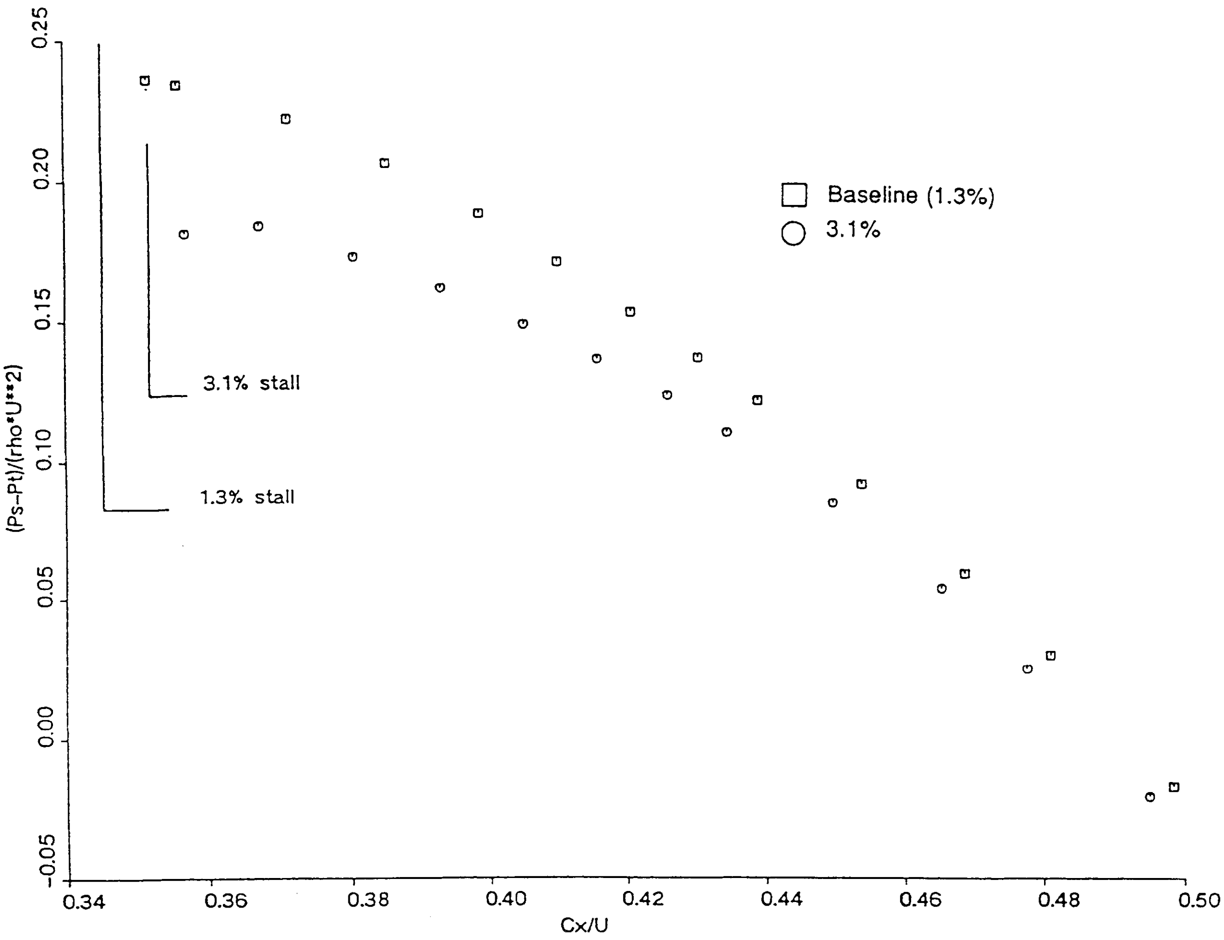

Figure 43: Stage 1 characteristics for baseline (1.3%) and large first stage (3.1%) rotor tip clearance builds. Note the increase in stalling flow coefficient.

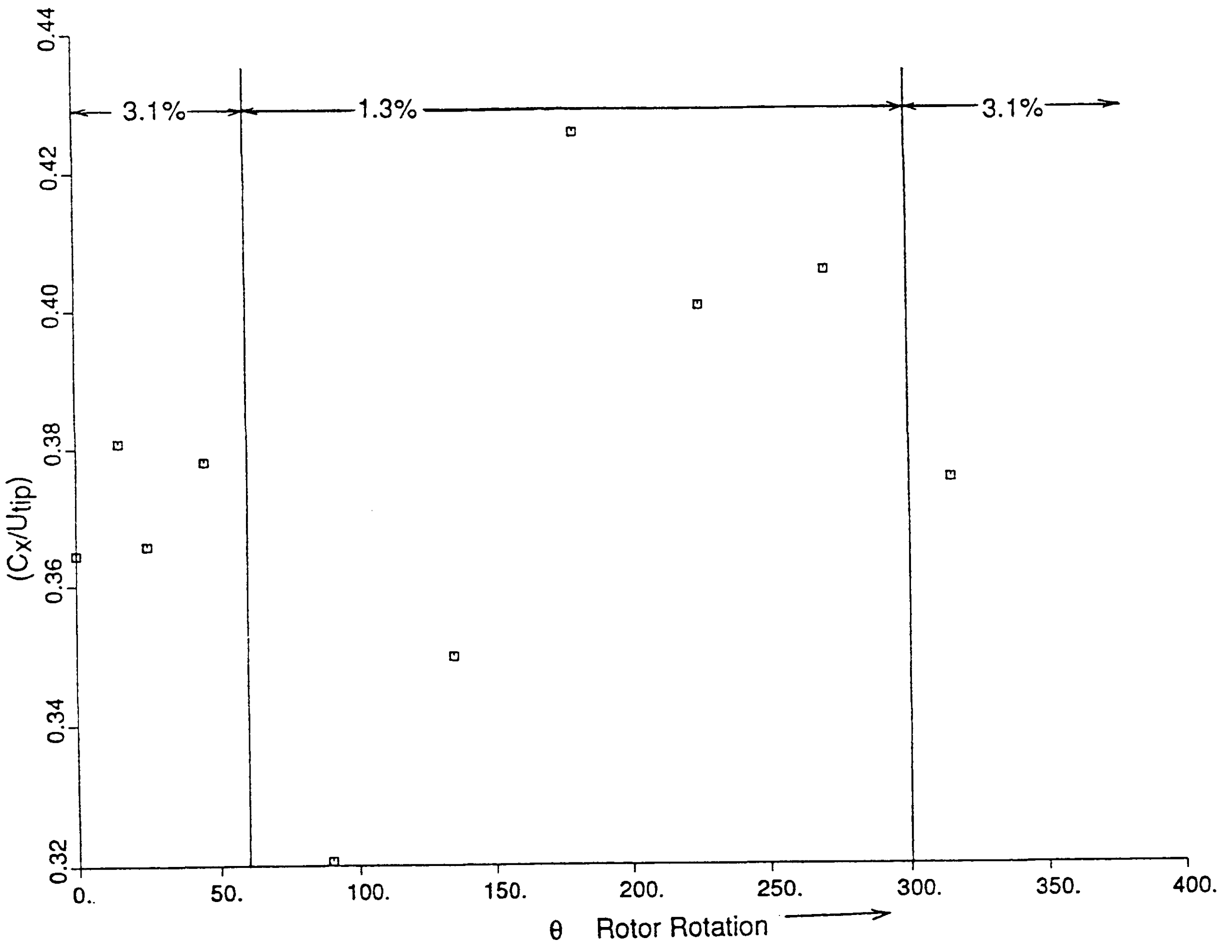

Figure 44: Mean velocity at rotor inlet, 20% immersion, near stall. Asymmetric first rotor tip clearance build. 3.1% and 1.3% first rotor tip clearance regions are indicated at the top. Each point is the average over ten rotor revolutions. The mean velocity is lowest at the exit of the large clearance region.

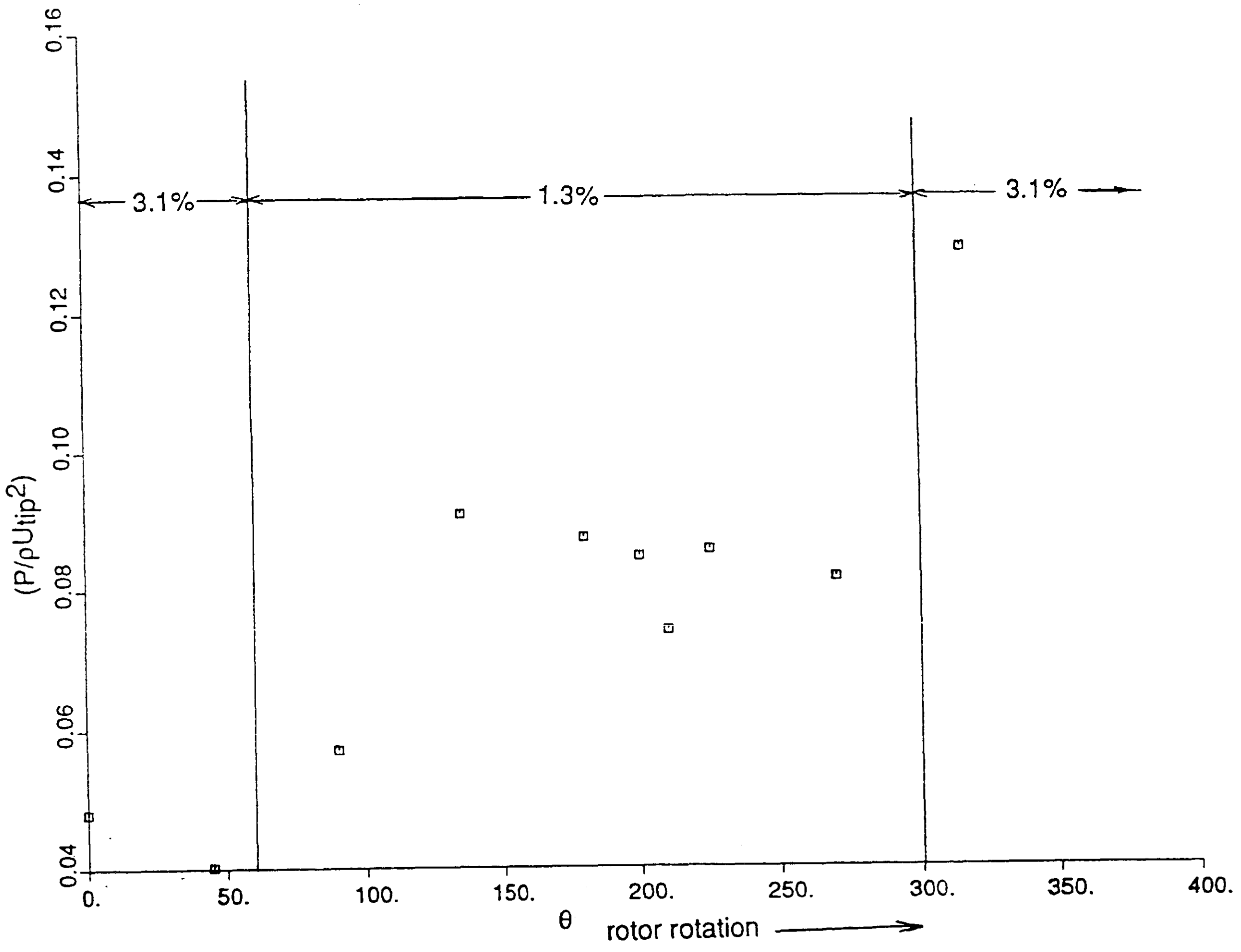

Figure 45: Mean casing pressure at rotor inlet, near stall. Asymmetric first rotor tip clearance build. 3.1% and 1.3% first rotor tip clearance regions are indicated at the top. Each point is the average over ten rotor revolutions. The mean pressure is lowest at the exit of the large clearance region. Same case as fig. 44.

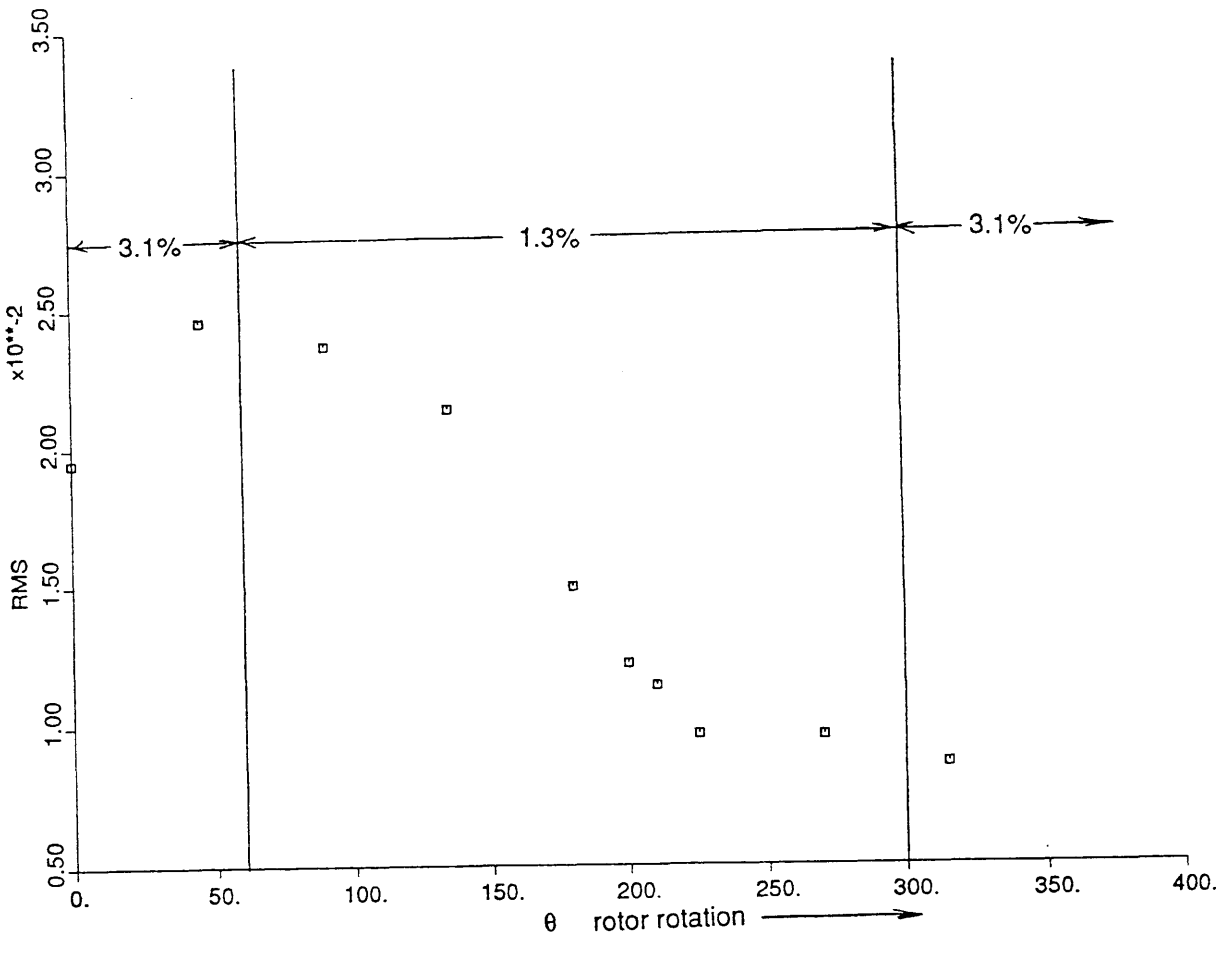

Figure 46: RMS of casing pressure at rotor inlet, near stall. Asymmetric first rotor tip clearance build. 3.1% and 1.3% first rotor tip clearance regions are indicated at the top. The noisiest signal is at the exit of the large clearance region. Same case as fig. 45.

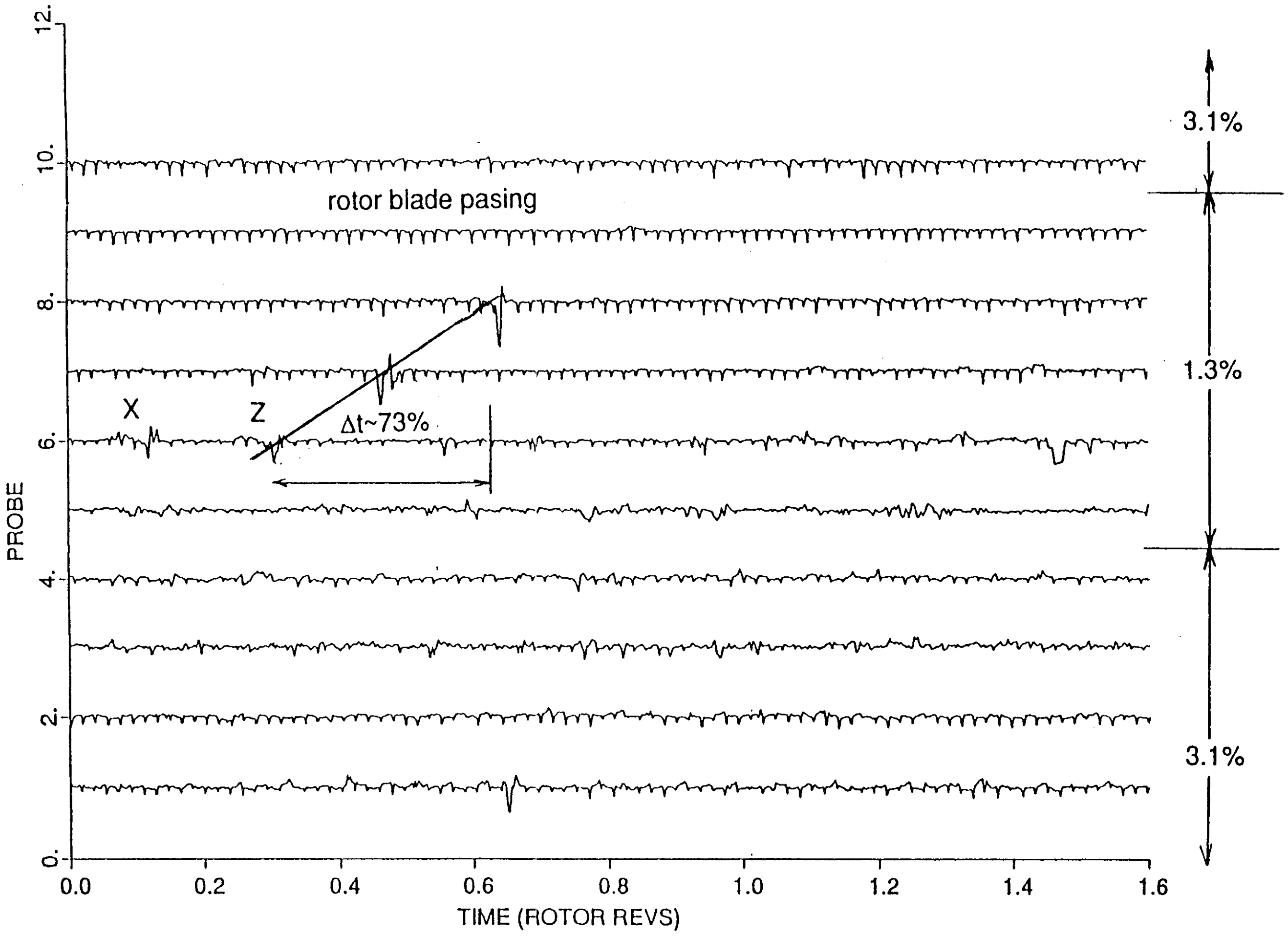

Figure 47: Normalized velocity at 30% immersion at rotor exit, near stall as throttle is closing. Asymmetric first rotor tip clearance build. Disturbances first seen at the exit of the large clearance region, X and Z. Both disturbances decay in tight clearance region. The clearance regions are defined on the side.

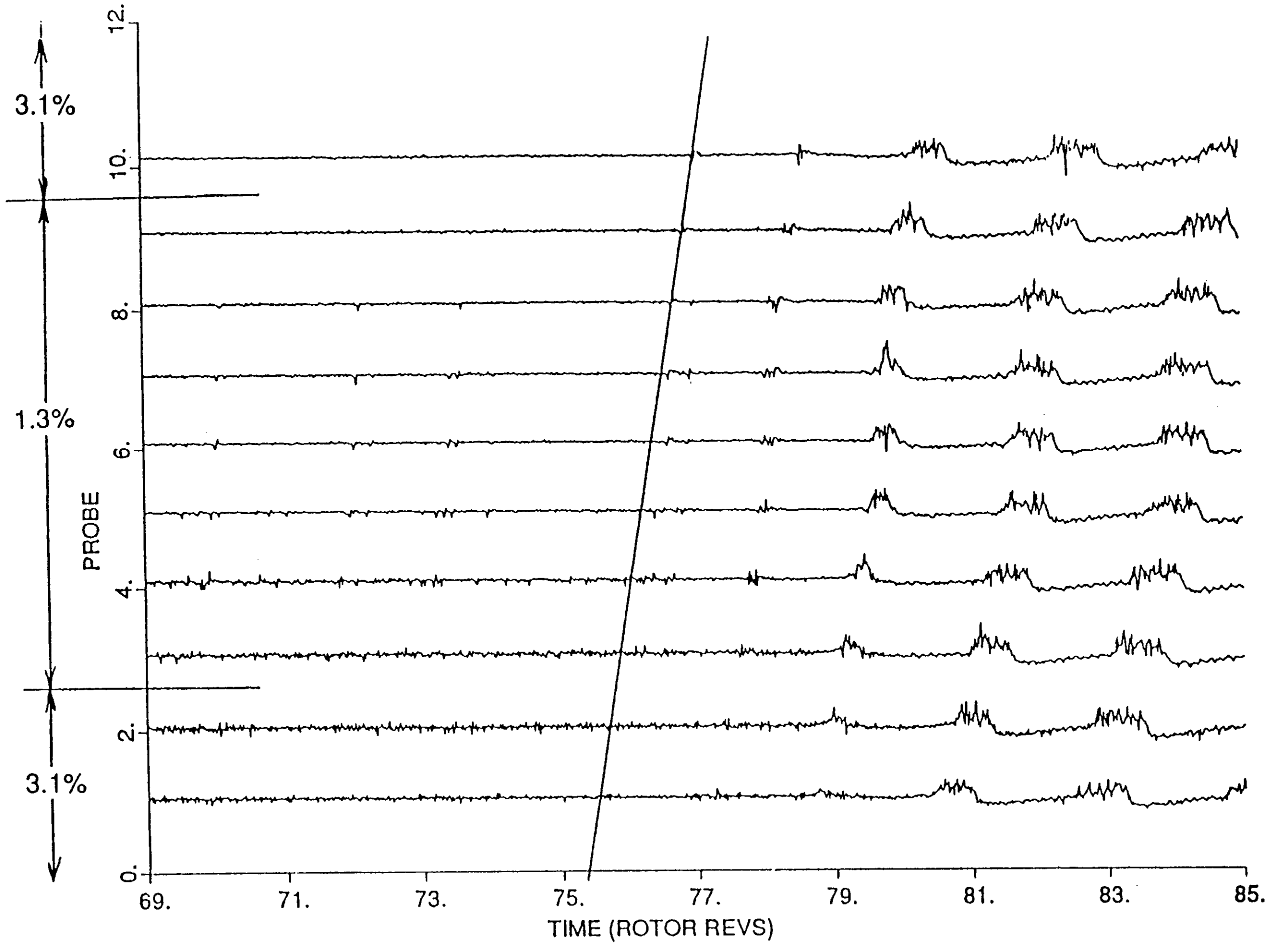

Figure 48: Casing pressure at rotor exit, as compressor is throttled down into stall. Asymmetric first rotor tip clearance build. Disturbances are visible at the exit of the large clearance region. Disturbances decay in tight clearance region. The clearance regions are defined on the side. Guideline drawn at 70% rotor speed.

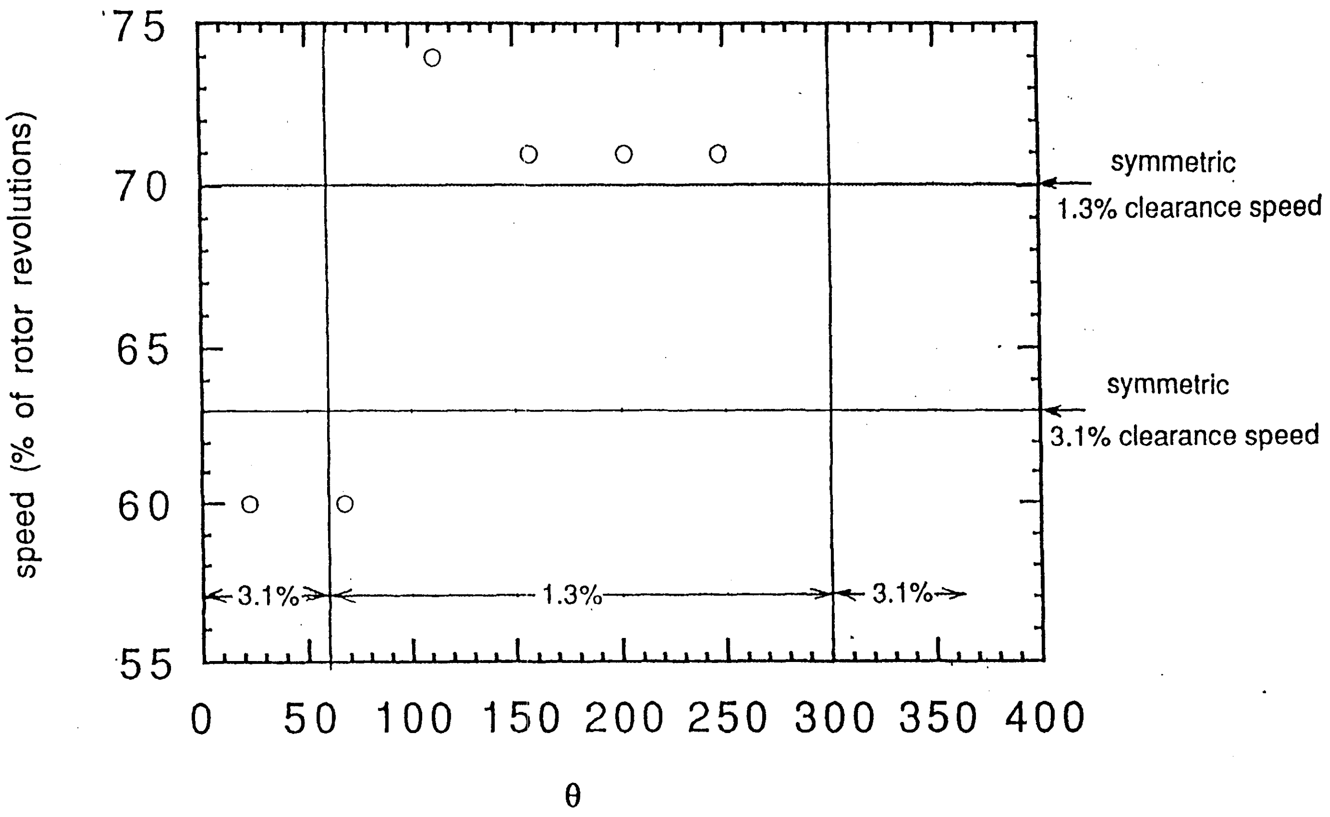

Figure 49: Calculated disturbance speeds of propagation from crosscorrelations of casing pressure transducers at rotor exit of asymmetric first rotor tip clearance build. The clearance regions are defined at the bottom. Disturbance behaves in each region as if in a symmetric region of similar character. Disturbance speeds in symmetric regions is displayed at the side.

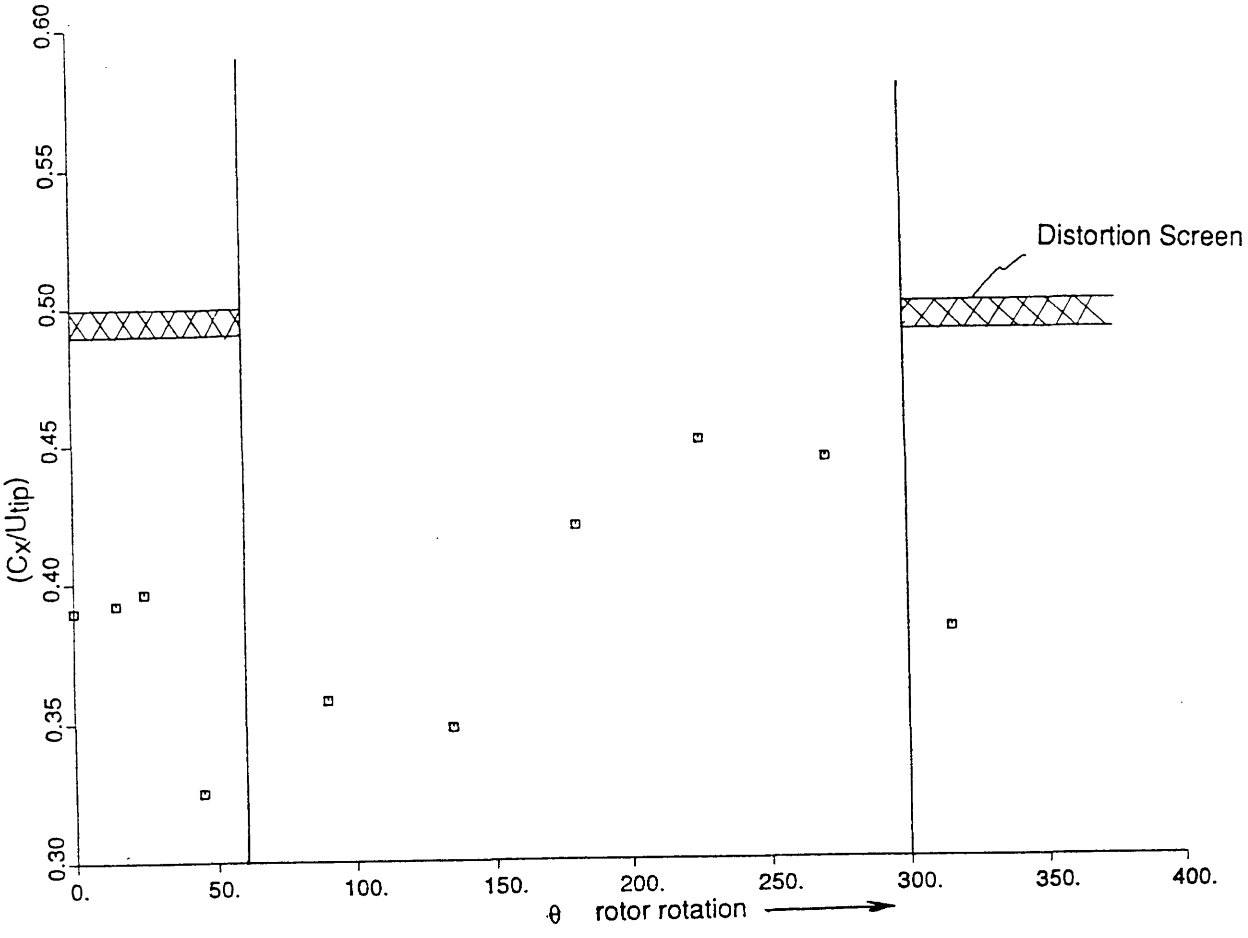

Figure 50: Mean velocity at rotor inlet, 30% immersion, near stall. Fixed 120 ° distortion screen 1.5 radii upstream of rotor. Each point is the average over ten rotor revolutions.
The mean velocity is lowest at the exit of the distortion screen.

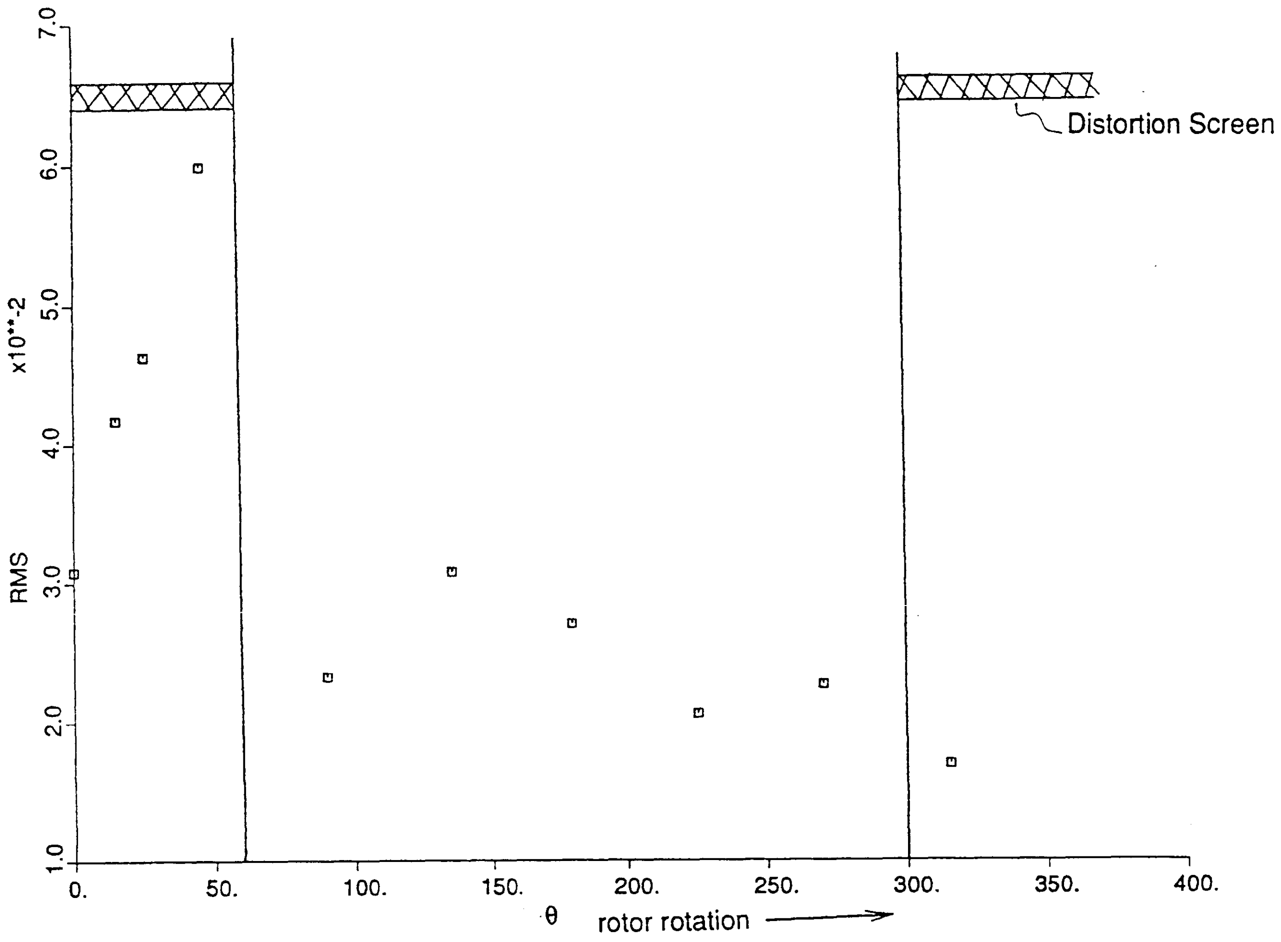

Figure 51: RMS of velocity at rotor inlet, near stall. Fixed 120 ° distortion screen 1.5 radii upstream of rotor. The RMS is highest at the exit of the distortion screen. Same case as fig. 50.

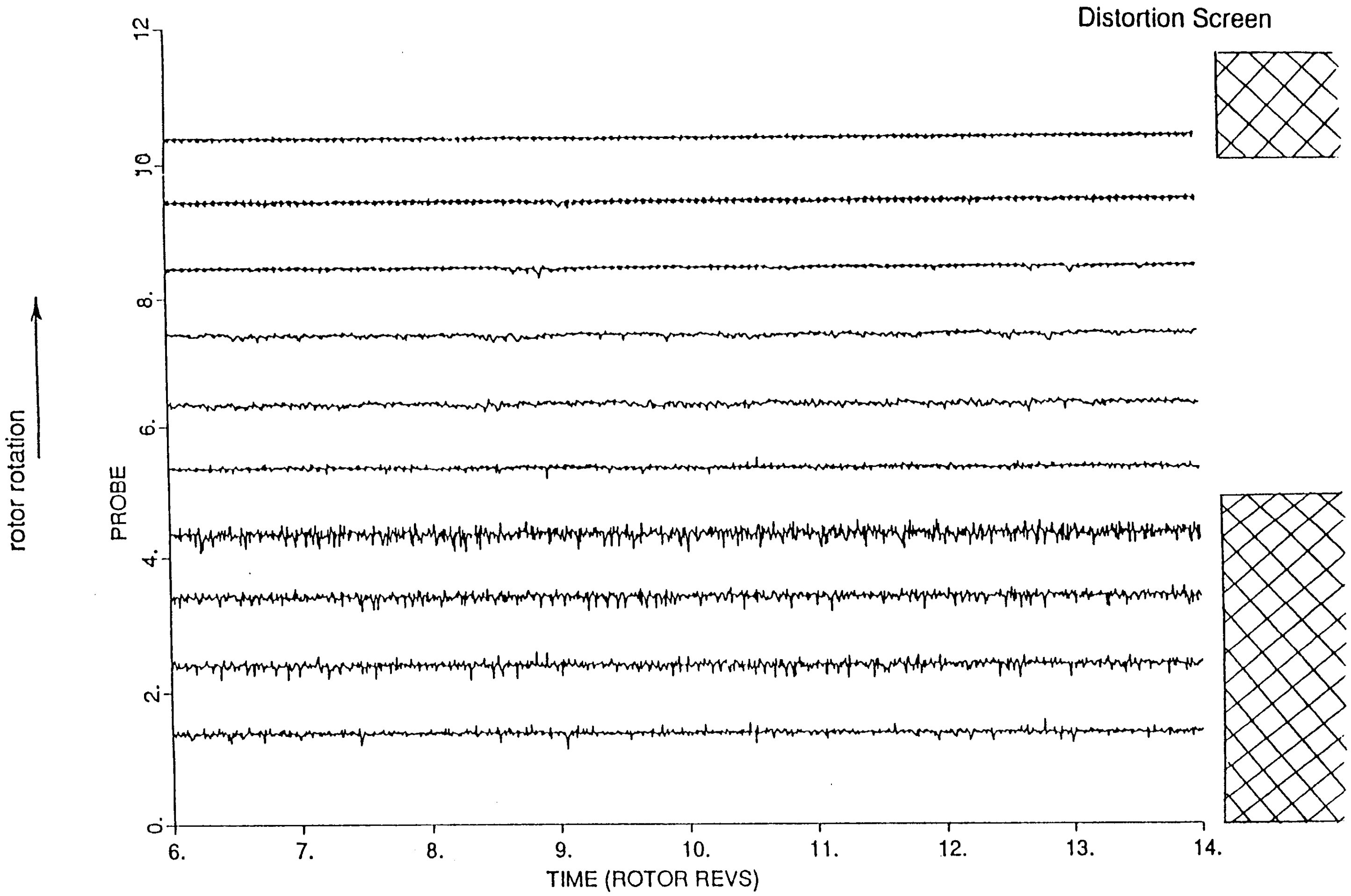

Figure 52: Velocity at rotor inlet, 30% immersion, near stall. Fixed 120 ° distortion screen 1.5 radii upstream of rotor. Disturbances are present at the end of the distortion screen region. Some disturbances propagate into the clean flow region and decay.

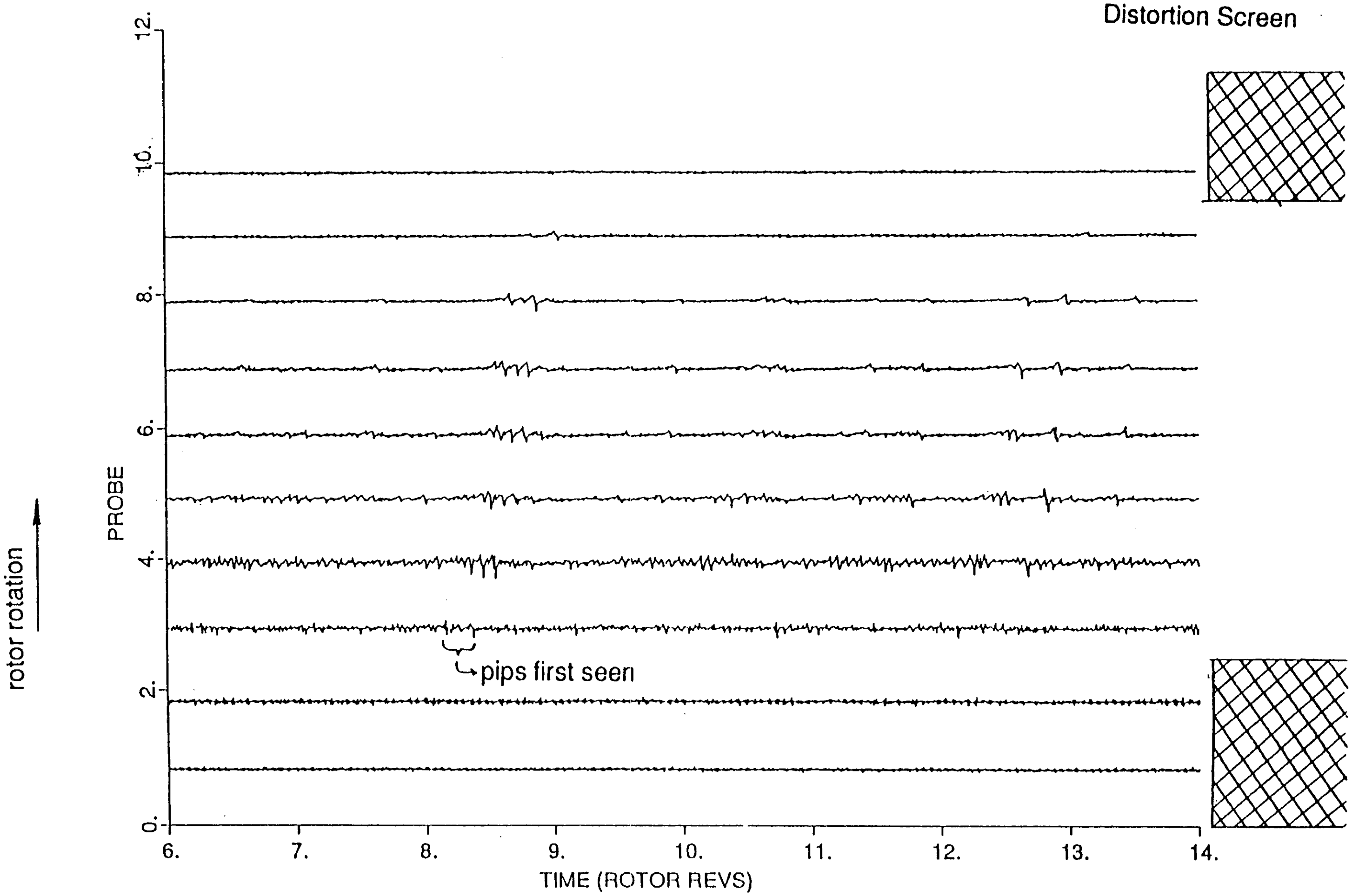

Figure 53: Casing pressure at rotor inlet, near stall. Fixed 120 ° distortion screen 1.5 radii upstream of rotor. Disturbances are present at the end of the distortion screen region. Some disturbances propagate into the clean flow region and decay. Same event as figure 52.

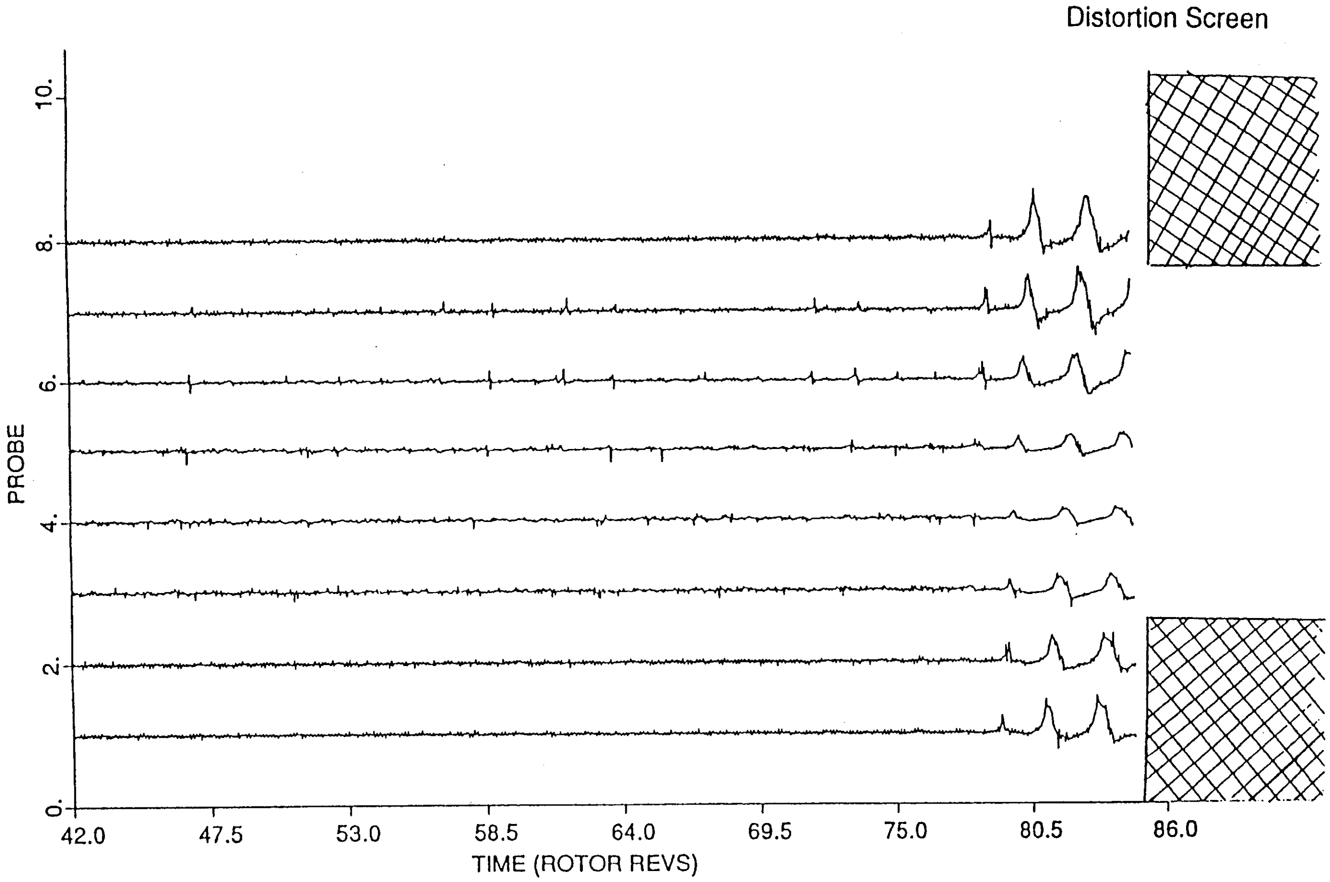

Figure 54: Casing pressure at rotor inlet, as the compressor is throttled down into stall. Fixed 120 ° distortion screen 1.5 radii upstream of rotor. The stall cell attenuates in the higher local flow of the clean flow region.

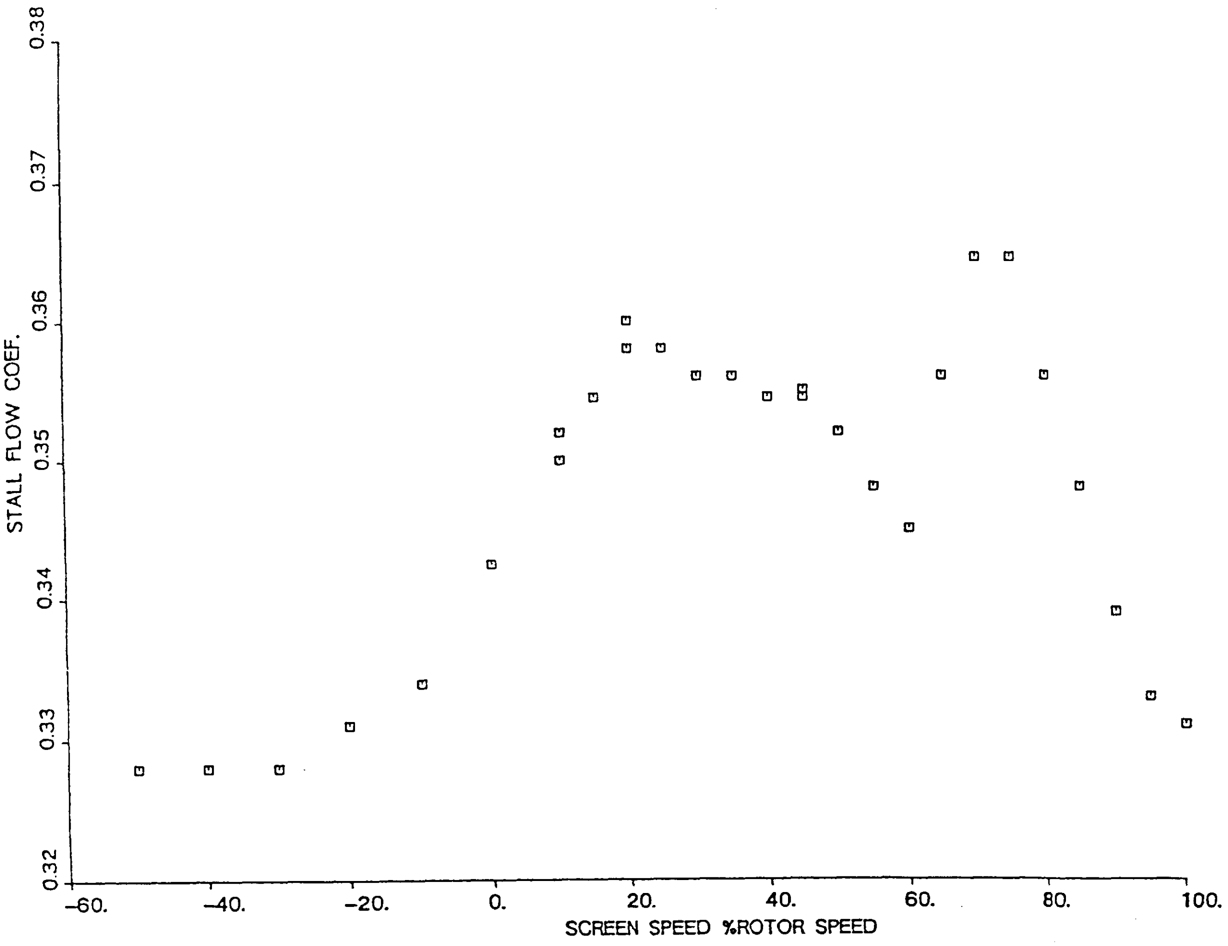

Figure 55: Stalling flow coefficient vs. distortion screen rotation rate. Note the two peaks, decreased stall margin, at roughly 20% and 70% speed.

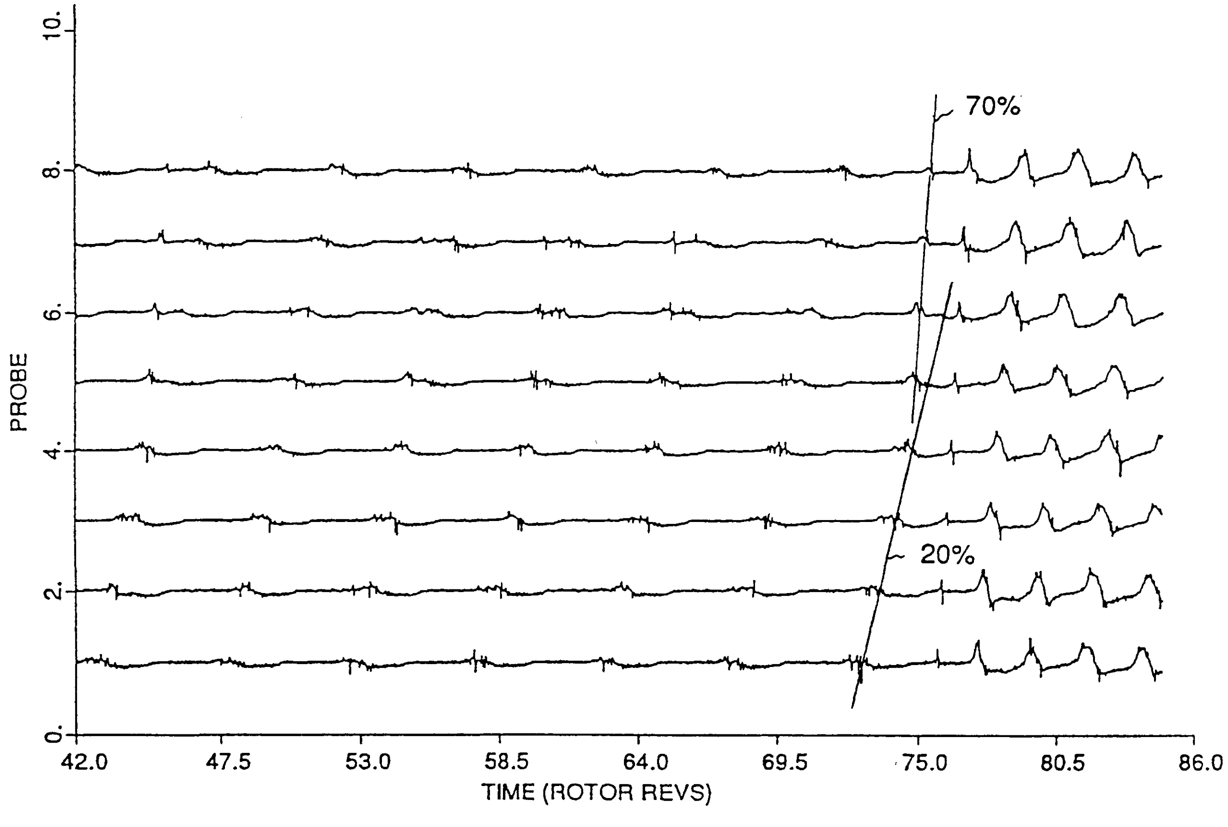

Figure 56: Normalized data from 8 equally circumferentially spaced casing pressure transducers at rotor inlet vs. time as the compressor is throttled down into stall. The 120 ° distortion screen is 1.5 radii upstream of the rotor, and rotating at 20% speed. Guidelines show the distrubance travelling at 70% speed that grows out of the 20% speed disturbance created by the screen.